INSTRUMENTATION AND ASTROPHYSICAL OBSERVATIONS

A thesis submitted to the University of Manchester

for the degree of Doctor of Philosophy

in the Faculty of Science

By

John Andrew O'Connor

Dept. of Physics & Astronomy

February, 2000

ProQuest LLC.
789 East Eisenhower Parkway
P.O. Box 1346
Ann Arbor, MI 48106 – 1346

Contents

List of Figures

List of Tables

Abstract

University of Manchester

ABSTRACT OF THESIS submitted by **John Andrew O'Connor** for the Degree of Doctor of Philosophy and entitled **Instrumentation and Astrophysical Observations**
Month and Year of Submission: February, 2000

The Manchester occulting mask imager (MOMI) is a device, when combined with the Ritchey–Chretien or Cassegrain foci of large telescopes, dedicated to the imagery of faint line–emission regions around bright sources. The design of MOMI is discussed along with initial observations, with MOMI combined with the Nordic Optical telescope (NOT), of the V = 4.8 mag P Cygni Luminous Blue Variable (LBV) star. A $\gtrsim 5'$ long [N II] λ6584 Å emitting filament has been discovered to be protruding from P Cygni's outer nebular shell. The presence of a strange monopolar lobe older than both the inner (22″ diameter) and outer (1′.6 diameter) shells is suggested. Images, with MOMI combined with the Isaac Newton telescope (INT), of the inner [Ni II] λ7378 Å emitting inner shell have been obtained and are compared with similar images of the inner shell in the light of [N II] λ6584 Å.

Kinematical observations have been made with the Manchester echelle spectrometer (MES) combined with the San Pedro Mártir telescope of the various features in the strange Planetary Nebula IC 4593. In particular high speed

flows are found to be emerging from the nebular core which do not correspond spatially to the low ionised knots. The outer halo knots, which appeared morphologically to be ejecta from the inner nebula, are, surprisingly, shown to be very inert raising questions about their origin. Various models for the whole structure are discussed in the light of these new observations.

The newly discovered hypersonic knots emerging from the young planetary nebula MyCn 18 have been investigated by obtaining imagery and spatially resolved spectrometry of the Hα and [N II] $\lambda\lambda$6548, 6584 Å nebular emission lines with the Manchester echelle spectrometer combined with the Anglo–Australian telescope (AAT). In the most likely configuration the knots are shown to have velocities (up to 630 km s^{-1}) which scale with distance from the central star. Furthermore, the knots are revealed to have very narrow line profiles, i.e., between 15 and 30 km s^{-1}. Along with several possible explanations, a recurrent nova–like ejection model is considered for the high speed knots. The bright, bipolar, nebular core of MyCn 18 is shown to be composed of two extended hemisperical shells whose axes are tilted at an angle of 52° to the plane of the sky.

Using MES on the AAT hitherto undiscovered hypersonic velocity features have also been discovered at the tips of the inner lobes of the young, bipolar planetary nebula Mz 3 . The possible connection with high velocity features observed in several other planetary nebulae is considered. It is suggested that Mz 3 might evolve to have hypersonic knots similar to those found around MyCn 18.

The work described in this thesis progresses from instrumental development, through observational use, to astrophysical discoveries.

Declaration

No portion of the work referred to in this thesis has been submitted in support of an application for another degree or qualification of this or any other university or other institution of learning.

Copyright & Ownership

1. Copyright in text of this thesis rests with the Author. Copies (by any process) either in full, or of extracts, may be made **only** in accordance with instructions given by the Author and lodged in the John Rylands University Library of Manchester. Details may be obtained from the Librarian. This page must form part of any such copies made. Further copies (by any process) of copies made in accordance with such instructions may not be made without the permission (in writing) of the Author.

2. The ownership of any intellectual property rights which may be described in this thesis is vested in the University of Manchester, subject to any prior agreement to the contrary, and may not be made available for use by third parties without the written permission of the University, which will prescribe the terms and conditions of any such agreement.

   Further information on the conditions under which disclosures and exploitation may take place is available from the Head of Dept. of Physics & Astronomy.

Acknowledgements

I owe a great debt of gratitude to my supervisor Prof. John Meaburn for his help, encouragement and advice and for making available the facilities of the Astronomy group in Manchester for these researches. My work has also benefited from many useful discussions with Drs. Myfanwy Bryce, Wolfgang Steffen and Matt Redman. If ever I had a computing problem one of Drs. John Palmer, Anthony Holloway or David Berry could be relied upon to either solve it or point me in the right direction. The forementioned, along with my peers in the Astronomy group, have provided a stimulating and genial atmosphere within which to work.

I should also thank the technical staff of the Dept. of Physics and Astronomy for their excellent assistance, in particular Mr. John Rowcroft, Mr. Derek Hornby, Mr. Jim Allen, Mr. Dick Carling, Mr. Ian Derbyshire and Mr. Terry Crossley without whom my research would not have been possible. I thank Miss Melanie Thomas for her secretarial support, particularly where observing trip expenses were concerned.

Finally, I must thank my parents and family for their support and encouragement during my undergraduate and postgraduate studies.

The Author

The author gained a B.Sc.(Hons.) degree in Physics with Astrophysics from the University of Manchester in 1996.

Preface

The work presented in this thesis was conducted between October, 1996 and January, 2000 at the University of Manchester. Observations presented here were obtained by the author at the San Pedro Mártir Observatory in March, 1997, the Nordic Optical telescope in November, 1997, the Isaac Newton telescope in September, 1998 and the Anglo–Australian telescope in April, 1999. All figures, unless otherwise stated, were produced by the author. Chapter 4 includes work from O'Connor, Meaburn & Bryce (1998) and Meaburn et al. (2000). Chapter 5 contains work from O'Connor et al. (1999). Chapter 6 contains work from O'Connor et al. (2000). Chapter 7 contains work from Redman et al. (2000).

Abbreviations

AGB – Asymptotic giant branch.

FWHM – Full width at half maximum.

HR – Hertzsprung–Russell.

INT – Isaac Newton Telescope.

ISW – Interacting stellar winds.

LBV – Luminous Blue Variable.

MES – Manchester echelle spectrometer.

MOMI – Manchester occulting mask imager.

NOT – Nordic optical telescope.

PN(e) – Planetary nebula(e).

To Claire and Ella

Chapter 1

Introduction

1.1 Luminous Blue Variable stars

The proto–typical Luminous Blue Variable (LBV) star, P Cygni, first came to the attention of modern astronomers in the early 17^{th} century[1] when it was discovered on August 18^{th}, 1600 by Dutch chart-maker Blaeu (cf. Lamers, De Groot & Cassatella 1983b and references therein). The star brightened to around third magnitude before fading to below the visible limit ($\lessapprox$ 6 Mag) within a few decades. In the 1650s another outburst brought P Cygni back to third magnitude prior to a period of extreme variability during the latter half of the 17^{th} century which resulted in the star settling at V $\approx$ 5.2 Mag. The years between 1700 and the present have seen a gradual increase in brightness to today's V = 4.8 Mag with continuing variability of a few tenths in magnitude.

[1]This may not have been the first time the star was noticed by Earthly observers, Meaburn et al. (1996a) found evidence of a similar outburst around 2100 yrs ago!

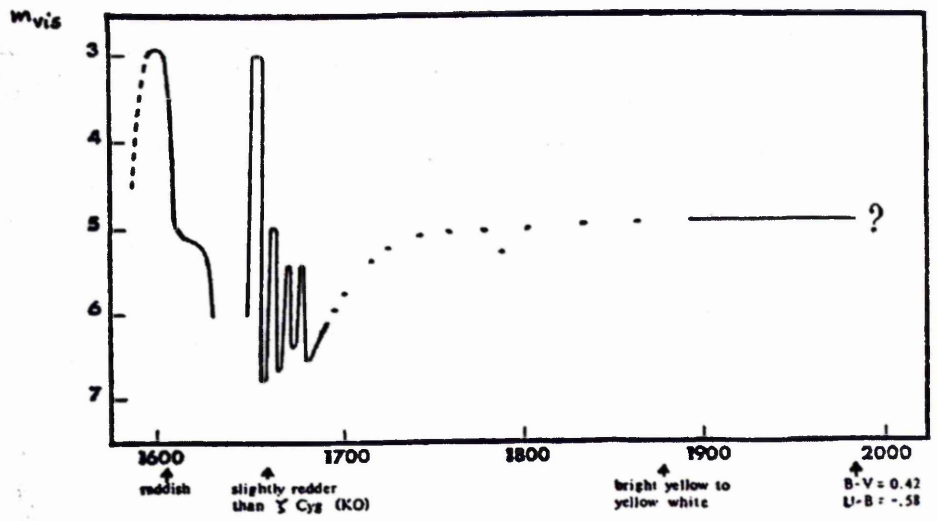

Figure 1.1: The historic light curve of P Cygni, after de Groot (1988)

A reconstructed light curve (after De Groot 1988) is shown in Fig. 1.1.

P Cygni is not the only massive star known to have shown variable behaviour during this period (cf. Nota et al. 1995 and references therein). η Carinae was recorded in the 17th and early 18th centuries to be between second and fourth magnitude, apparently varying. After 1820 the brightness varied with increasing rapidity until, in the 1830s, η Carinae became one of the brightest stars in the sky with a magnitude varying between -1 and 1. η Carinae faded after 20 years to eighth magnitude where it remained, apart from an excursion in the late 19th century, until recently (1940s) when a gradual increase in brightness has occured.

The 20th century has seen P Cygni better known for its emission line profile than its history of violent eruptions, indeed it is the star's eruptive nature that has provided the explanation of its emission line profile. Although P Cygni and η Carinae have been known to astronomers for several hundreds of years

it was not realised until recently that these stars were members of a class of stars now known as LBVs[2].

LBVs are rare, only a handful of Galactic LBVs are known – P Cygni, η Carinae, AG Car, HR Car, WRA 751, HD 160529 and, possibly, HDE 316285 (Hillier et al. 1998). Two further Galactic LBVs have been discovered recently in the Quintuplet Cluster (Figer, McLean & Morris 1995; Figer et al. 1998; Lang et al. 1999; Figer et al. 1999), one of which is now known as the 'Pistol Star' due to the shape of, what is suspected to be, its nebula. A similar number of LBVs are known in nearby galaxies. The scarcity of LBVs alone would imply that they are stars which are experiencing a short lived phase in their evolution. There is evidence that the LBV phase lies on the evolutionary path an O star follows prior to becoming a Wolf–Rayet star (Lamers, De Groot & Cassatella 1983a; Garcia-Segura, Mac Low & Langer 1996; Moffat, Drissen & Robert 1989; Langer 1989). They are characterised by high intrinsic luminosities, photometric variability, high mass–loss rates and circumstellar shells or nebulae.

The high intrinsic luminosities (Table 1.1) place the LBVs at or near the top of the Hertzsprung–Russell diagram (Fig 1.2; HR diagram). Absolute bolometric luminosities range from -8 to -11.6 mag. In the ionised photosphere of a hot star the momentum from the photon flux is transferred to the free electrons which in turn pass momentum to the protons via strong electrostatic interactions. The rate at which momentum is transferred to the electrons is

[2]The term Luminous Blue Variables was first used by Conti as recently as 1984.

independent of wavelength, temperature and gas density ($\dot{p} = h\nu\sigma_{\rm T}F/c$ where F, the number flux of photons with frequency ν, is $L(h\nu 4\pi R^2)^{-1}$; $\sigma_{\rm T}$ is the scattering cross–section, h is Planck's constant, c is the speed of light and R is the distance from the centre of the star). Restricting the radiation pressure to less than the gravitational force gives the 'classical' Eddington limit, $L/M < 4\pi cGm_{\rm p}/\sigma_{\rm T}$, where G is the gravitational constant and $m_{\rm p}$ is the mass of a proton, or $L/M < 4\pi cG/\kappa$ where κ is the opacity per unit mass. The 'classical' Eddington limit assumes the minimum likely opacity (that due to Thomson scattering) and thus gives a maximum likely L/M ratio ($L/M = 6.32$). The ratio of L/M to the 'classical' Eddington limit is generally above $\frac{1}{2}$ for LBVs (Humphreys & Davidson 1994), P Cygni, for example, has a L/M ratio close to three quarters of the 'classical' Eddington limit, it is, therefore, believed that radiation pressure contributes to their instability (cf. Appenzeller 1989). Differences from the Eddington limit will depend on the effective opacity (Burger & Lamers 1989).

On the HR diagram (Fig. 1.2) the LBV stars flirt with the empirically derived luminosity limit, the Humphreys–Davidson limit (Humphreys & Davidson 1979; HD limit). The HD limit shows a temperature dependence for stars above $\sim 10,000$K and a temperature independent luminosity limit for stars below $\sim$ 8000K. Humphreys & Davidson (1979) suggested that above a critical initial mass stars do not evolve towards the red supergiants. As the star cools an unstable configuration is encountered that limits evolution to cooler temperatures. The instability results in significant mass–loss which halts the

Star	$M_{\rm Bol}$	Apparent temp. (quiescence)	(eruption)	$\dot{M}$ (eruption)	Circumstellar shells
P Cygni	-8.3	19,000	...	5×10^{-4}	*yes*
η Carinae	-11.6	20,000–30,000	...	1×10^{-3}	*yes*
AG Car	-10.8	30,000	9,000	3×10^{-5}	*yes*
HR Car	-8.9	14,000	...	...	*yes*
WRA 751	-9.6	...	...	...	*yes*
HD 160529	-8.6	11,000	8,000	...	*yes*
HDE 316285[1]	-8.9	15,000	...	...	...

Table 1.1: Physical parameters for known galactic LBVs. Adapted from Nota et al. (1995) and Humphreys & Davidson (1994). [1]Possible LBV (Hillier et al. 1998).

stars red-ward evolution turning it blue-ward. The modified Eddington limit, with a temperature and density dependent opacity, may offer an explanation for the locus in the HD limit.

Variations in the optical brightnesses of LBVs have been observed with amplitudes ranging from a few tenths in magnitude to several orders of magnitude (Van Genderen et al. 1985; Van Genderen et al. 1990; Shore, Altner & Waxin 1996), as in the case of η Carinae's 'giant eruption' of 1837. These variations can be categorised by distinct amplitude scales (Lamers 1987). Firstly, variations of a few hundredths to a few tenths of a magnitude are observed over time-scales of days to months (Van Genderen et al. 1985; Van Genderen et al. 1990; Van Genderen et al. 1999). Secondly, oscillations of half a magnitude or so, with periods of months, are observed superposed on the third category, 'eruptions' or 'normal' or S Doradus–type eruptions. These 'eruptions' can produce brightness variations of 1–2 magnitudes with periods of order years to several decades and were observed in the late $18^{\rm th}$ century in P Cygni for example. A fourth and much more dramatic type of eruption has been ob-

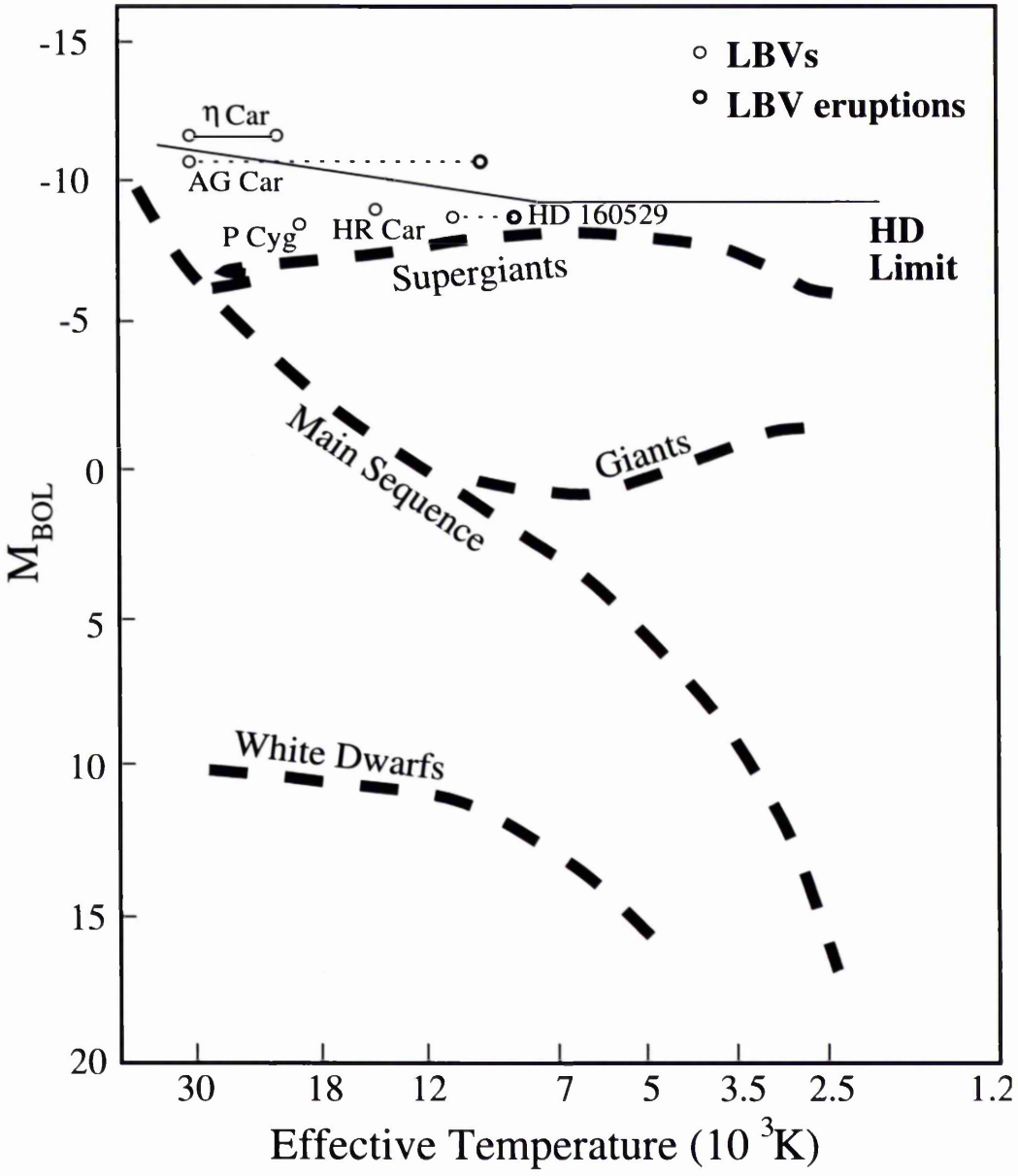

Figure 1.2: The locations of the galactic LBVs, tabulated in Table 1.1, are indicated on a HR diagram. The evolution through the eruptive phase is indicated by the dotted lines.

served in just two Galactic and two extra-galactic LBVs. Great eruptions or η Carinae Type eruptions, in excess of 2 magnitudes, define a rare subset of LBVs, the η Carinae variables (Humphreys, Davidson & Smith 1999). The four known η Carinae variables are η Carinae itself, P Cygni, SN 1961v and V12 in NGC 2403 and may be joined by the Pistol Star (Figer et al. 1998; Figer, McLean & Morris 1995). Humphreys & Davidson (1994) draw a simile between LBVs and geysers, or volcanoes, both exhibit 'patterns of moderate activity, then violent burbling, then the fitful eruption itself, followed by a period of relative quiescence'.

LBVs exhibit high mass-loss during their eruptive phases, ejections of order 10^{-2} $M_{\odot}$ for P Cygni (Barlow et al. 1994) to 2-3 $M_{\odot}$ for η Carinae (Humphreys & Davidson 1994) are estimated to be present in shells associated with giant eruptions. Mass-loss rates during these giant eruptions was of order $\dot{M}$=10^{-4} $M_{\odot}yr^{-1}$ to $\dot{M}$=10^{-3} $M_{\odot}yr^{-1}$ and $\dot{M}$=10^{-2} $M_{\odot}yr^{-1}$ for P Cygni and η Carinae respectively if the mass-loss occurred over similar time-scales to the photometric variations. The high mass-loss in their eruptive phases distinguishes the LBVs from the supergiants they resemble during quiescence (Lamers 1989). The mechanisms driving the mass–loss rates observed in LBVs are not understood.

As indicated in Table 1.1 the known galactic LBVs show signs of nitrogen enriched circumstellar nebulae, indicative of CNO-cycle enhancements. The nebulae range in morphology from the bipolar η Carinae homunculus through rings to almost spherical shells, such as those around P Cygni. As with the

shells around Planetary Nebulae (PNe) the shaping mechanism is not fully understood. Bipolar shells may be generated in a variety of ways (Frank 1999). The interacting winds model has a fast spherical wind ploughing into an aspherical slow wind previously ejected from the star. Bi-polarities can be formed by equatorial density enhancements in the slow wind restricting the progress of the fast wind via momentum conservation. This model has successfully reproduced bi-polar PNe (Kahn & West 1985) though it does pose questions – why is there a density contrast in the slow wind and at what time did the contrast form? Frank, Ryu & Davidson (1998) suggest the opposite scenario i.e. isotropic slow wind and aspherical fast wind, which transfers the density enhancement questions to the fast wind. Models for aspherical mass–loss can include binary companions to break the spherical symmetry of the stellar system, rotation of the star allowing the effective gravity at the equator to be less than at the poles or magnetic fields within the star. Garcia-Segura, Mac Low & Langer (1996) have suggested that an instability in the wind of P Cygni will cause a fragmented spherical nebula.

Nebulae offer an opportunity to study the historical mass–loss of these stars (Nota & Lamers 1997; Smith et al. 1998). So far two shells have been discovered around P Cygni. Barlow et al. (1994) found the expansion speed of the inner, $\sim 22''$ diameter, shell of P Cygni to be 140 km s^{-1} in the light of [N II] λ6584 Å but only 110 km s^{-1} in the light of the flourescently excited (Lucy 1995) and exceptionally bright [Ni II] λ7412 Å emission line. The lower velocities found in the light of [Ni II] λ7412 Å compared to those obtained

from the light of [N II] λ6584 Å have been convincingly explained by Barlow et al. (1994) as being due to dense clumps of material being overtaken by the 206 km s^{-1} wind (Lamers, Korevaar & Cassatella 1985) of P Cygni. The outer, 1′.6 diameter, shell has been shown to have an expansion velocity of 185 km s^{-1} in the light of [N II] λ6584 Å (Meaburn et al. 1996a). The outer shell coincides with radio emission observed by Baars & Wendker (1987) and Skinner et al. (1998) to the North–East of P Cygni. A more compact radio nebula is also present (Skinner et al. 1997). The observations of Watson (private communication) demonstrate significant variations between epochs 3 days apart at angular scales of 0″.1 (Fig. 1.3). Vakili et al. (1997) also found evidence for subtle structures in the wind of P Cygni in their optical spectra. Lamers, Korevaar & Cassatella (1985) found evidence in UV spectra of [Fe II] for three distinct thick shells having been ejected from P Cygni between 1978 and 1983. The ISO–SWS observations of Lamers et al. (1996) indicate that the circumstellar envelope is clumpy. It seems likely that the mass loss from the star is not in perfectly spherical shells but in distinct clumps of material. The imaging observations of Barlow et al. (1994) were obtained with the Manchester echelle spectrometer (MES – Meaburn et al. 1984) working in its coronographic mode. In its coronographic mode the MES has a limited field of view (1′.9 ×1′.5) on the Isaac Newton telescope (INT) consequently any nebular ejecta from P Cygni at larger angular distances would remain undetected. To overcome this restriction the Manchester occulting mask imager (MOMI) has been developed and is described in detail in Chapter 2 of this

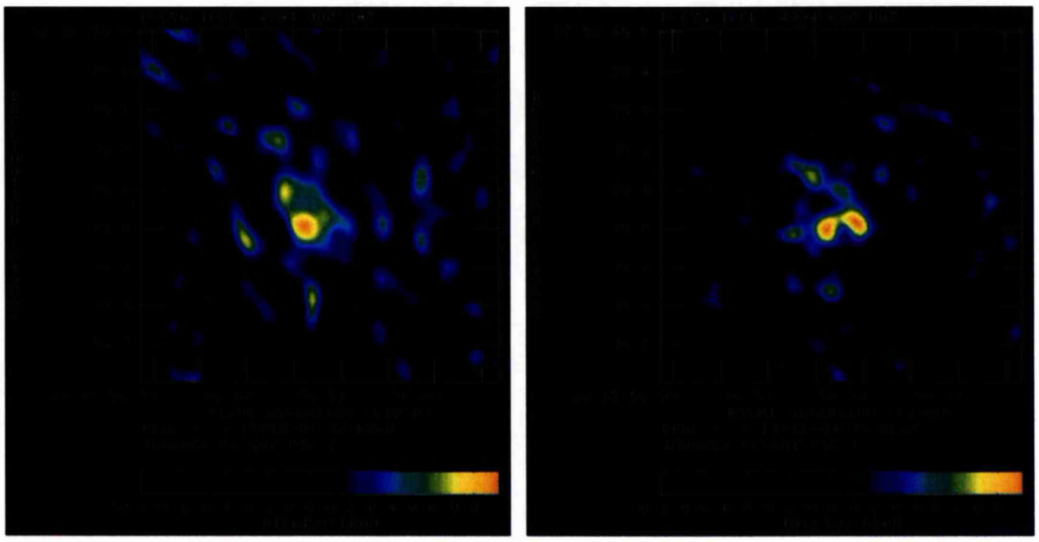

Figure 1.3: Merlin observations (courtesy of S. Watson) of P Cygni at 5 GHz obtained on the 16 January, 1996 (left) and on the 19 January, 1996 (right).

thesis. Results on the environs of P Cygni obtained with MOMI are presented in Chapter 4.

1.2 Planetary Nebulae

1.2.1 Introduction

Planetary nebulae are generally accepted to be formed by the interaction of winds from red giant stars as they evolve into white dwarfs. Many spectacular and evocatively named nebulae are known. Some of the more famous include the Cats Eye Nebula (NGC 6543), the Engraved Hourglass Nebula (MyCn 18) and the Eskimo Nebula (NGC 2392). PNe were named after their disc–like appearance to early observers; they looked like planets.

Stars with mass $0.8M_{\odot} \lessapprox M \lessapprox 8M_{\odot}$ follow a loop around the Hertzsprung–

Russell diagram (Fig. 1.4). The central stars of PNe determine the evolutionary behaviour as one of the two post core nuclear–burning shells, either hydrogen or helium, provide the energy for the surface luminosity until the fuel runs out and the star radiates away its remaining gravito–thermal energy. After the star has inflated through the red giant phase, having lost significant mass, in the form of the red giant wind, helium burning commences and the star rises to the asymptotic giant branch (AGB). During the AGB phase the stellar structure is unstable. Most of the energy generating the luminosity is released by hydrogen burning in a shell. An instability is generated by a helium burning shell which contributes little to the luminosity apart from spikes during 'thermal' or 'helium shell' flashes. Most of the energy is consumed in raising the hydrogen shell which then cools and almost extinguishes. At this time the helium shell is the major energy contributor until the hydrogen shell settles, contracts and again becomes the major energy contributor.

Significant mass–loss at the upper part of the AGB phase is most important in determining the final mass of the star. The ratio between the energy released in helium and hydrogen burning as the star leaves the AGB determines the speed and path of a star through the HR diagram to the white dwarf phase . As mass–loss determines the point at which the star leaves the AGB phase it also determines the stars point of entry into the PN phase. From this point nuclear burning controls the evolution of the star. Eventually the star runs out of fuel having shed the outer layers of material and the hot core remnant is exposed. The expansion of the cool dusty envelope lost during the AGB

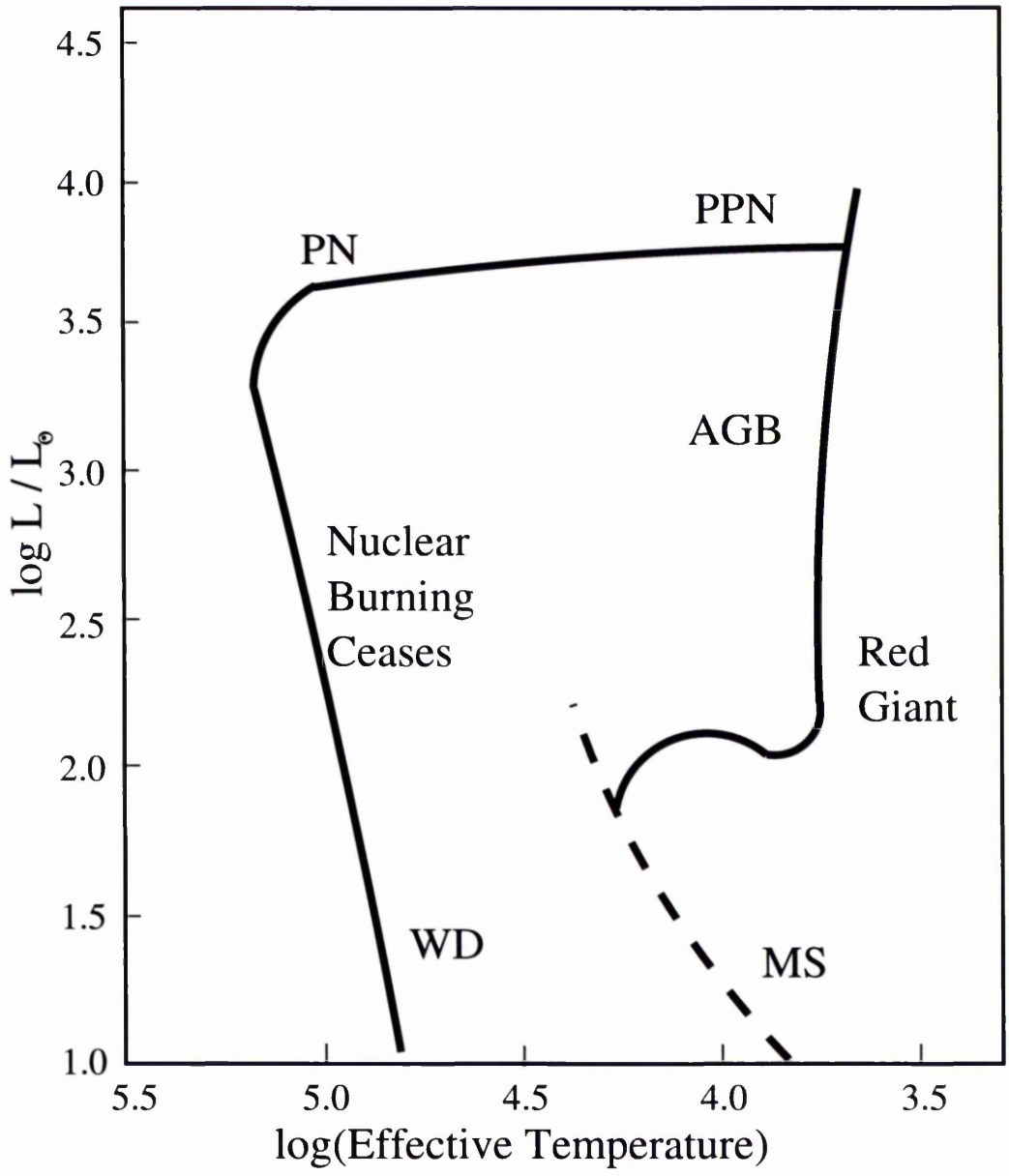

Figure 1.4: Hertzsprung –Russell diagram showing the evolution of a star M = 3 $M_{\odot}$. After leaving the main sequence (MS) the star moves up through the red giant phases (RG, AGB) before moving blue-ward at constant luminosity, through PPN and PN phases, and down towards the white dwarf phase.

phase reveals the proto–white dwarf at optical wavelengths

The exposed core drives a fast, tenuous wind into the AGB super–wind sweeping the denser super–wind into a thin shell. The shell is is radiatively ionised by the the UV flux from the central star. The shell radiates strongly in characteristic lines such as Hα, [N II] λ6584 Å, and [O III] 5007 Å[3].

1.2.2 Generalised interacting winds models

The generalised interacting stellar winds models can, in many cases, convincingly reproduce the global structure and bulk dynamics of the majority of PNe (see e.g., Mellema 1995 and references therein; see also García-Segura et al. 1999 for magneto-hydrodynamical considerations). In these models, the shape of a PN is determined by the interaction between the slow wind lost by the star whilst on the asymptotic giant branch (AGB) and the fast wind and ionizing radiation that emerges from the exposed hot stellar remnant. These models can even reproduce some aspects of the often visually spectacular class of bipolar PNe. Numerically, modest asymmetries between the equatorial and polar regions in either the AGB mass loss rates and/or the subsequent fast wind speed can lead to the characteristic hourglass or butterfly morphologies of bipolar PNe. However, the physical reasons for such asymmetries are far from clear and the study of bipolar PNe is motivated in part by the possibility of obtaining insights into the physics of circumstellar matter.

[3]These lines were not originally identified and were attributed to an element not occurring on Earth, nebulium.

The central stars of these more extreme bipolar PNe may differ from those of ordinary elliptical PNe. Corradi & Schwarz (1995) find evidence (small Galactic scale-height, high N-abundance, high effective temperature of central star) that suggests that the progenitors of some bipolar PNe are more massive than those of elliptical PNe. This is supported by the numerical calculations of Mellema (1997) who shows that, by including the evolutionary tracks of PNe precursor stars, bipolar PNe develop around the slightly higher mass stars since the evolutionary time-scale is shorter and the AGB ejecta is exposed to a more sudden 'switch on' of ionizing photons (and so has less time to dynamically relax to an elliptical shape) than for lower mass progenitors. Meaburn & Walsh (1989) argue that a bipolar, 'slow-nova' ejection leads to the very high speed motions they detect in the extreme bipolar PN He 2-111.

1.2.3 Hypersonic phenomena

Although the bright core morphologies and kinematics are beginning to be understood by the generalised interacting stellar winds models, a broader range of dynamical mechanisms should be considered to explain the many attendant phenomena of PNe. Small scale structures (such as the Helix knots, Meaburn et al. 1998), symmetric intermediate scale structures (such as 'FLIERS', e.g., Balick 1987; Balick et al. 1993; Schwarz, Corradi & Melnick 1992; Cliffe et al. 1995) and large faint extended structures (such as the envelope of KjPn8, López et al. 1997) have all attracted interest in recent years. A particular phenomenon that cannot immediately be accounted for by

the generalised interacting stellar winds models is the generation of hypersonic outflows in the extreme bipolar PNe. High–speed characteristics are found in objects such as He 2-111 (Meaburn & Walsh 1989), He 3-1475 (Bobrowsky et al. 1995), KjPn 8 (Lopez, Vazquez & Rodriguez 1995; Lopez et al. 1997) and MyCn 18 (Bryce et al. 1997). Knotty outflows are seen in the extended strings of lower speed knots found emerging from Fleming 1 (Lopez, Meaburn & Palmer 1993; Lopez, Roth & Tapia 1993). It is important to establish how such high speed flows originate so that it can be inferred whether or not such unusual features require only additions to the interacting winds models (such as the effects of binarity) or whether they instead imply that the physical basis of these models requires substantial revision.

Observations of the PN IC 4593 are presented in Chapter 5 of this thesis. IC 4593 appears to have a morphologically complex system of jet like flows both within its nebula and in the giant halo which surrounds it. The newly discovered hypersonic outflow from PN MyCn 18 is investigated in detail in Chapter 6. Observations of PN Mz 3 are presented in Chapter 7 which may indicate that the hypersonic flow observed in MyCn 18 have their origins in the venting of an over pressured bubble.

Chapter 2

The Manchester occulting mask imager

2.1 Introduction

The Manchester Echelle spectrometer, MES (Meaburn et al. 1984), in its imaging mode, and with an occulting strip in its focal plane, was used to obtain imagery of the V=4.8 mag LBV P Cygni. In this auxiliary mode, MES has a very restricted field–of–view (1.9 arcmin × 1.5 arcmin) on the Isaac Newton 2.5-m telescope (INT) consequently any nebular ejecta from P Cygni of larger angular diameter would remain undetected. The Manchester occulting mask imager (MOMI) has now been manufactured to overcome this restriction. This is a device dedicated to occulting mask imagery and had its first use on the Nordic Optical telescope (NOT) where [N II] λ6584 Å images of the environs of P Cygni have been obtained over a field area of unprecedented

size. Furthermore MOMI has now been commissioned on the Isaac Newton 2.5-m telescope during which time further emission line images of P Cygni were obtained.

The design of MOMI is discussed in detail in this Chapter and suggestions for future refinements, in the light of the results (Chapter 4) from the first uses of the instrument in combination with the NOT and the INT, are made.

2.2 Optical layout of MOMI

The optical layout of MOMI, at the Cassegrain focus of the NOT telescope, is shown in Fig. 2.1. The light is collimated for passage through a narrow–band interference filter, centred on a nebular emission line and placed in the pupil. The field is re–imaged on the 'science' CCD.

The most critical aspect of the design is that the chromium occulting mask, $\equiv 4''$ on the sky, is on the first surface of the optical chain. With this arrangement, when faint nebulosity around a bright star (e.g. the V = 4.8 P Cygni) is being imaged, the only contamination of the field is then by the starlight scattered in the atmosphere and reflecting optics of the two–mirror telescope, along with diffraction spikes caused by the spines of the telescope's secondary mirror mounting. Any refracting optical component prior to this mask floods the field with 'ghosts' with such a bright star as a result of multiple reflections. The chromium mask transmits 0.01 percent of the incident light. This is useful in two ways. The position of the star relative to the mask is recorded

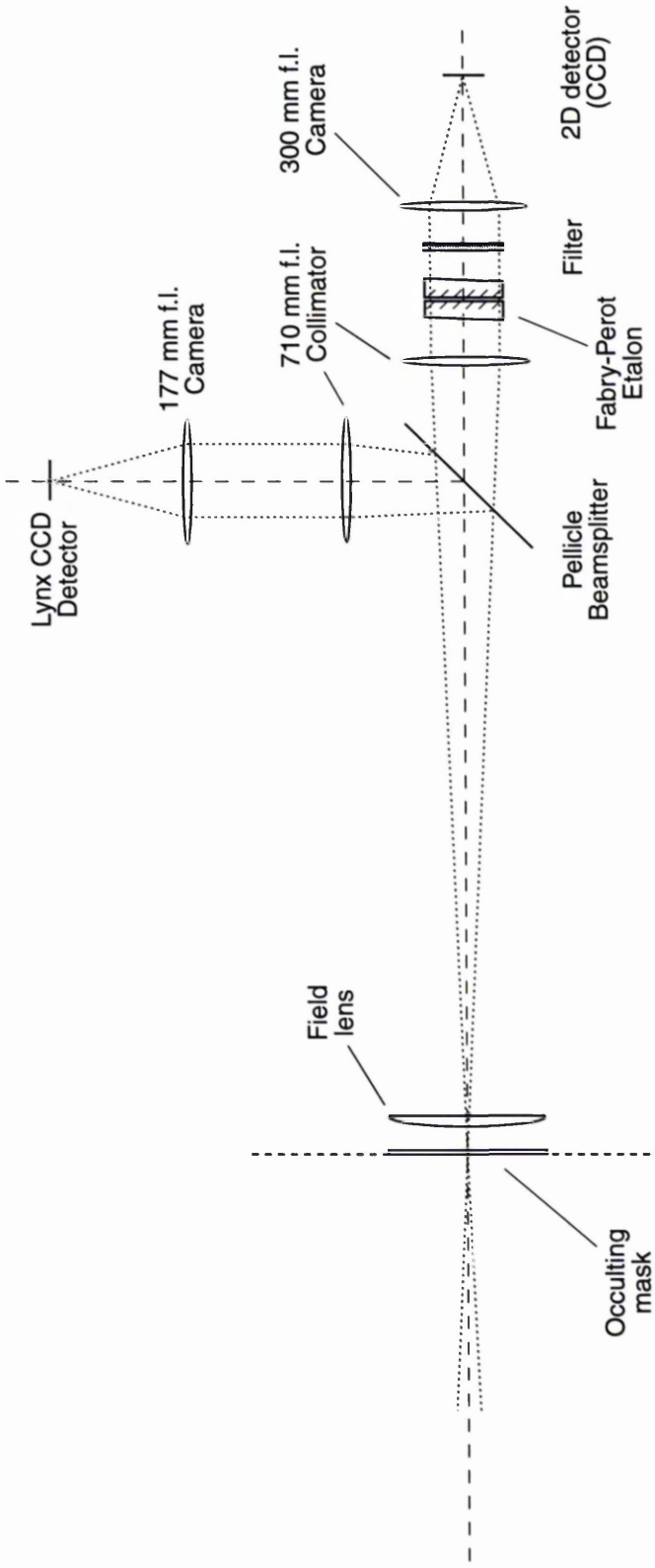

Figure 2.1: The optical layout of MOMI.

by the science CCD. Also the stellar position can be monitored throughout the integration by reflecting 8 percent of this light out of the beam with a mylar beamsplitter and forming a broad–band image on a secondary CCD, in this case a thermo–electrically cooled Lynx.

2.2.1 Using narrow–band filters for wide–field imagery

Narrow band–width filters are of the interference type, they are, in essence, low order Fabry–Pérot (see Appendix B) etalons and their properties can be understood when considered as such. The most important property of a Fabry–Pérot etalon is the dependence of wavelength transmission peak and width on input angle. As an etalon is tilted with respect to the optical axis the effective separation between the reflective plates increases changing the interference conditions for a given etalon. This property is exploited when interference filters are tuned down to a particular passband by tilting.

Unlike Fabry–Pérot etalons, which are usually placed in a collimated beam at a pupil, interference filters are classically used close to the Cassegrain focal plane. Close to the focal plane the filter 'sees' a pencil of light from a given position in the field, the opening angle of the pencil is determined by the speed of the optical configuration and this spread in input angle is far more important than the angular difference between different points in the field. Thus, it can be assumed that a perfectly manufactured filter will give even transmission over the field (this assumption must be carefully considered when fast optical systems and/or narrow filters are used). For wide–field imagery

on large telescopes, however, the field size is limited by the physical size of the filter close to the Cassegrain focal plane. Large format filters can be produced by a variety of methods (Meaburn 1959) but are expensive and it is difficult to get even performance over their larger physical area. For this reason the interference filters in MOMI are placed at a pupil in a collimated beam. The input angle is then determined by the field position and care has to be taken to minimise the angular difference across the field. This has been achieved in MOMI by the choice of a long focal length (710 mm) for the Tessar collimator. The change of input angle across the field, and hence the passband centre and FWHM, is illustrated in Fig. 2.2 for various filter tilt angles for MOMI.
For completeness the dependence of passband centres and half-widths of an interference filter are shown in Fig. 2.3. The measurements, made by the author, are of a 70 mm diameter filter nominally centred on 6592Å with a nominal full-width at half-maximum of 20Å. The measured maximum passband differs from the value quoted by the manufacturer. Furthermore the passband depends upon temperature and, as a rule of thumb, a drop of 1 K results in shifting the passband by 0.2Å down the spectrum.

2.2.2 Occulting masks

The optimum size of any mask must depend on the size of the maximum 'seeing' disc encountered in any one integration, yet be small enough not to obscure any useful circumstellar nebulosity. The 'seeing' disc considered must include the contribution from the movement of the star in the focal plane. For

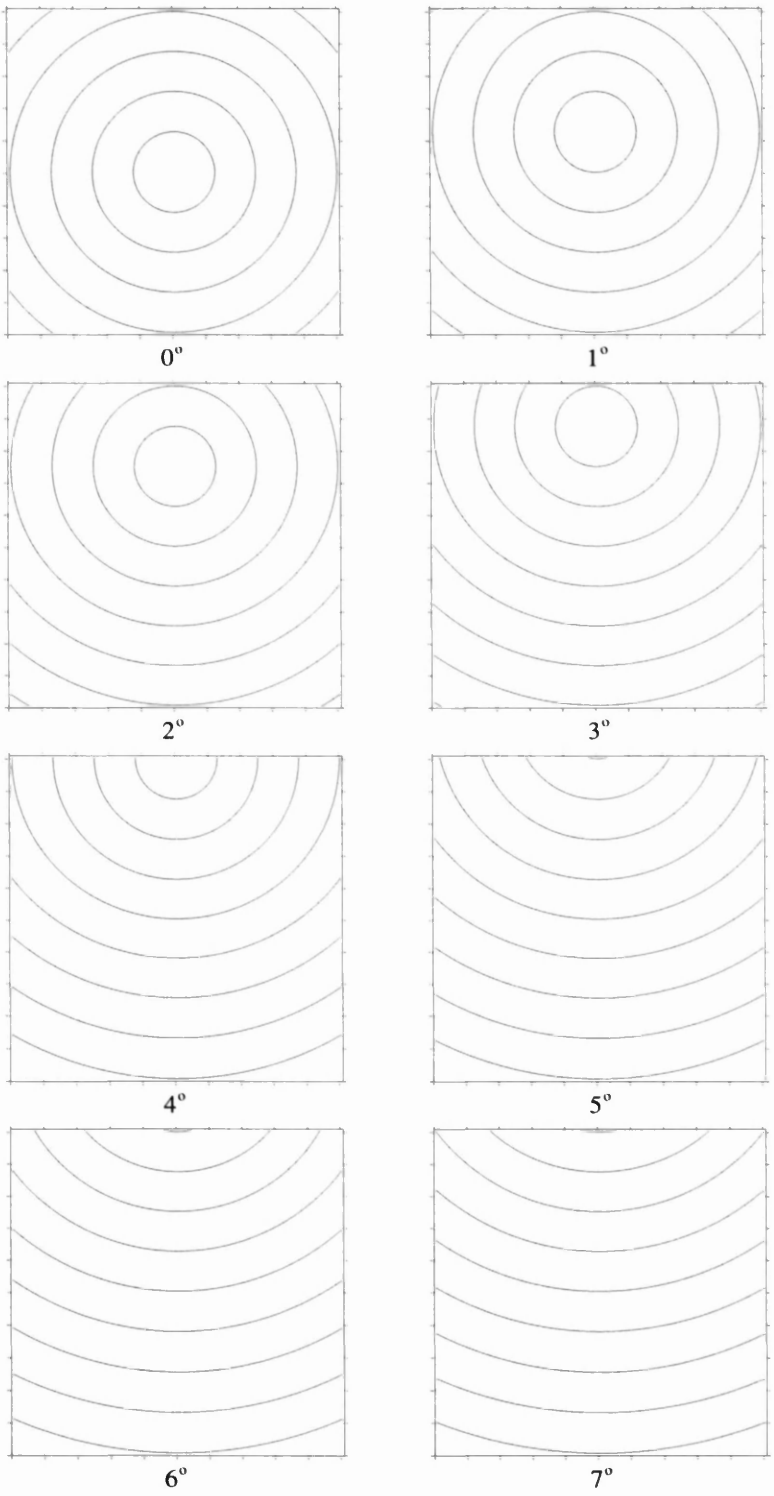

Figure 2.2: Contour maps indicating the angle from the normal incident light subtends for various filter tilts over the full field of MOMI. Starting in the 0° frame the contours are at intervals of 1° with 0° in the centre. The contours may be followed through each frame as they move towards the top of the figure.

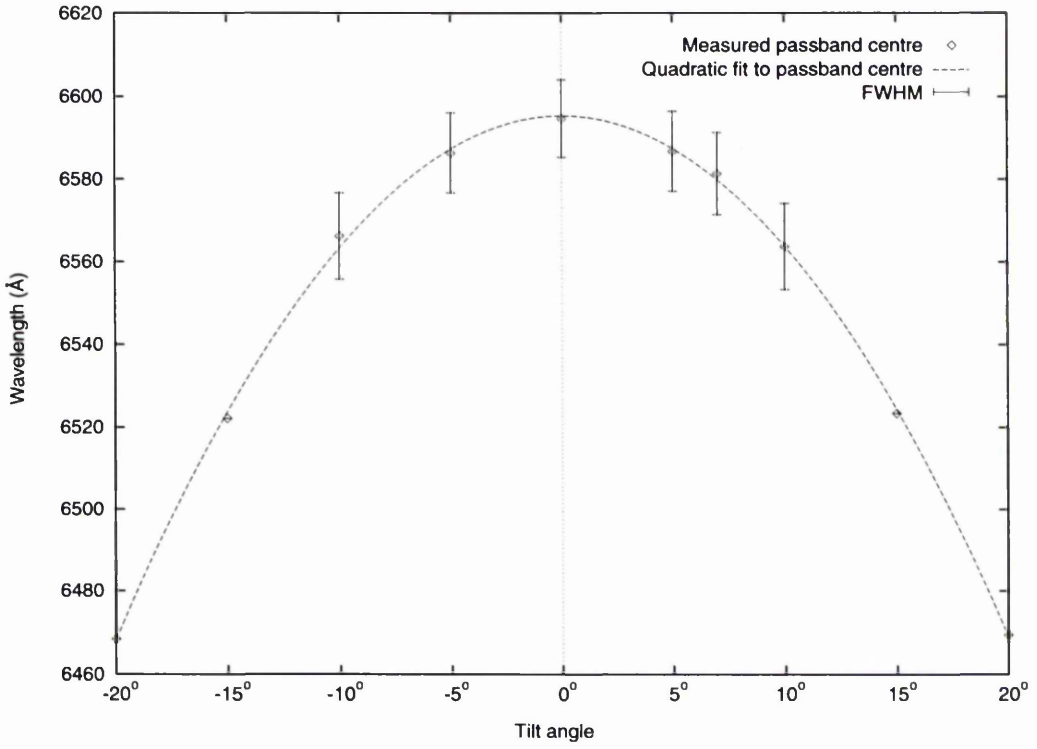

Figure 2.3: Passband properties of a narrow-band multi–layer interference filter. The passband centre is indicated by the open diamonds. The error bars indicate the FWHM. The solid line is a simple quadratic fit to the passband centres. The measurements were made at 17° C using a high resolution grating spectrometer

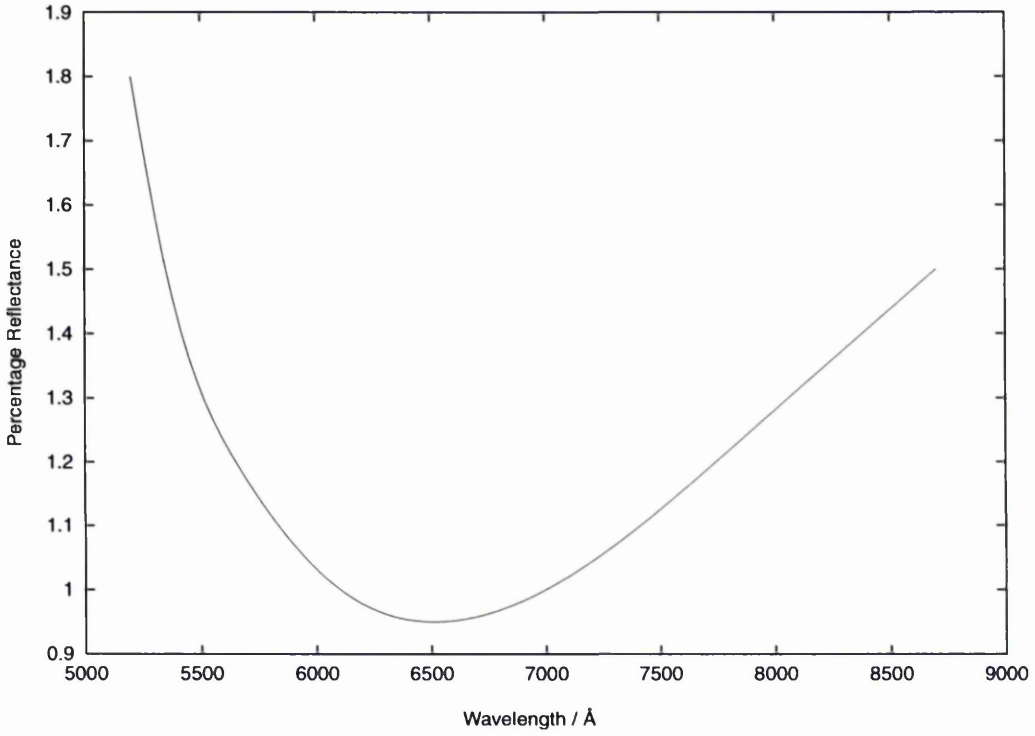

Figure 2.4: The theoretical reflection amplitude plotted against wavelength for the MgFII coating applied to MOMI's occulting mask.

instance, during commissioning of MOMI on the INT it was found that there were large guiding errors. These errors effectively increased the diameter of the 'seeing' disc.

The initial occulting mask prepared for MOMI, and the one used for the observations presented in this thesis, is a 400 μm circular disk of chromium deposited onto a 150 mm diameter BK7 'Superwhite' glass substrate. The mask and substrate have a MgF_2 anti-reflection coating (see Fig. 2.4 for reflection properties) applied after the deposition of the chromium. The optical density of chromium is a strong function of wavelength[1]. The transmission

[1] I must thank an anonymous referee for bringing this to my attention

λ (Å)	ξ
5020	1.555
5880	1.261
6680	1.311
7000	1.105
7500	0.978

Table 2.1: The wavelength dependance of the extinction coefficient for Cr (Fréedericks 1911)

function for a thin metallic film, of thickness d, may be given as

$$I = I_0 \exp \frac{-4\pi\xi d}{\lambda} \tag{2.1}$$

where ξ is the extinction coefficient (see Table 2.1 for tabulated values near wavelengths of interest here) and the other symbols have their usual meaning. It is obvious from the above equation and table that to achieve similar rejection properties over a wide waveband (4500 Å – 7500 Å) chromium is not the most well behaved mask material.

It is perhaps worth re–iterating here that the primary science driver for MOMI was the search for faint nebulosity at large angular distances from a bright star. For this purpose an occulting mask system is required to extend the integration times possible when observing with what amounts to a bright field star. The relationship between the occulting mask size and the relayed pupil (see §2.3) is not as critical as when one wishes to observe close to a bright star (as in the case of the search for extra–solar planets, Malbet 1996). It was for this reason that in its initial commissioning the exit pupil of MOMI was not fully apodised. Apodisation was performed in the exit pupil of MOMI on the f/11

NOT telescope by the filter holder. This apodisation only affects the intensity of the Airy disk caused by the circular telescope entrance aperture and not the spikes due to the secondary mirror support struts which rotate with respect to the field during the night.

Occulting masks need not be single circular deposits but may be made to mask any object or objects which detrimentally affect an image. For instance, the Trapezium stars in Orion (Fig. 2.5, see also Weigelt et al. 1999) inhibit the study of their environs. A mask could be manufactured that would simultaneously occult the Trapezium stars and the other bright stars in the field allowing extremely deep imagery to be obtained.

For the study of phenomena extremely close to any star the occulting mask must be made smaller. As the mask size is reduced the residual diffracted energy in the relayed pupil naturally increases as less is removed in the focal plane. Thus it becomes more difficult to apodize the diffraction pattern and other types of masks may prove more effective. Recent investigations by Guyon et al. (1999) have shown that phase masks outperform occulting masks in their rejection of unwanted light and offer a higher increase in contrast between the star and the surrounding light. Phase masks have a limited wavelength coverage as the technique relies upon the complete phase reversal of a fraction of the unwanted light which then interferes with the non-phase shifted light from the diffraction pattern. Phase masks could feasibly be used in MOMI however much development would be needed and, in any case, very narrow field investigations would be better achieved with an integrated adaptive optics and

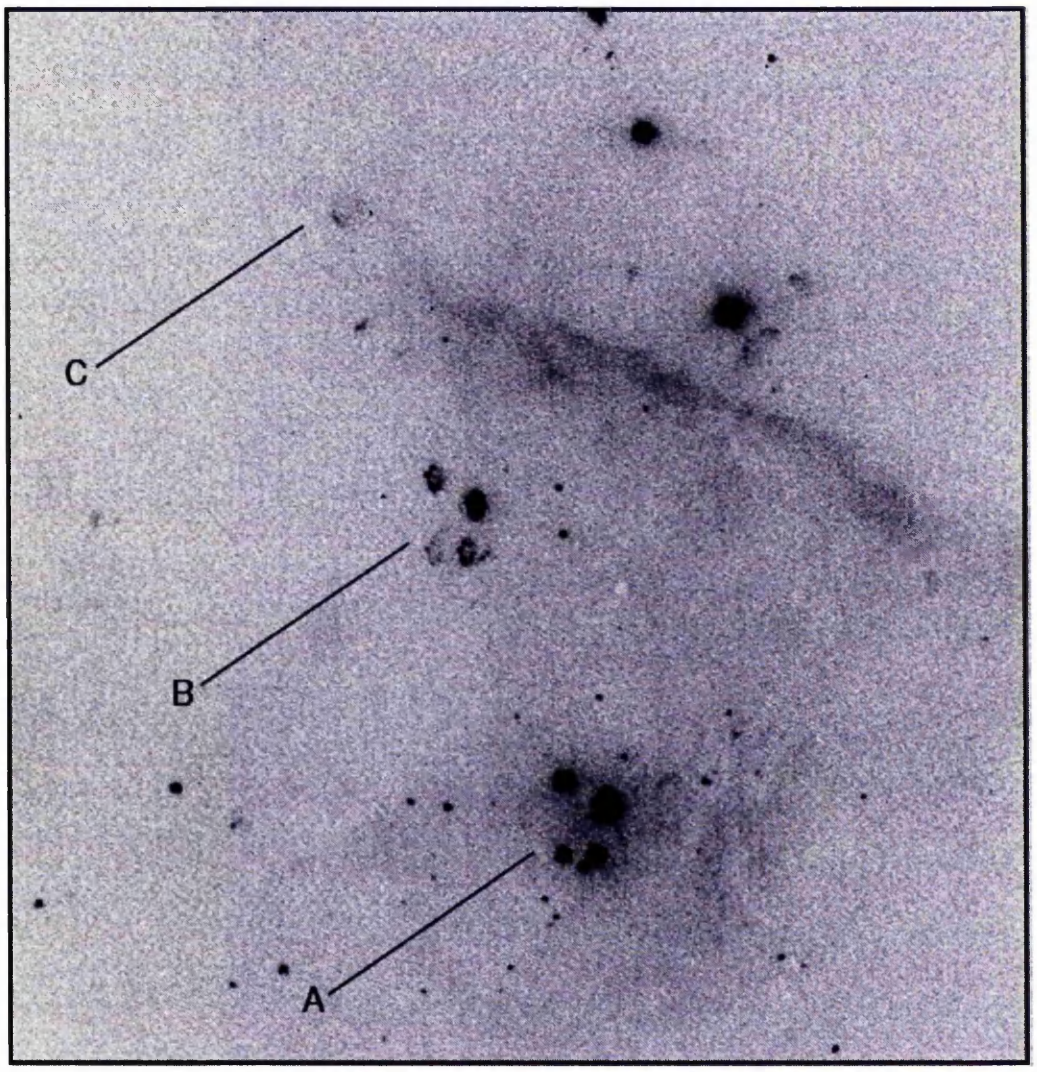

Figure 2.5: The Trapezium stars (labelled A) in Orion are extremely bright and produce multiple ghosts (labelled B & C) in this [S II] $\lambda\lambda$6717, 6730 Å image. The integration time of 2 s is sufficient to saturate the CCD.

coronographic device.

2.3 Apodisation of the diffraction pattern

The occulting mask in the focal plane of the telescope is of finite size. This finite size limits the amount of unwanted starlight that can be removed from the system; any light that falls outside the mask cannot be removed by it. In particular, light diffracted in the telescope's entrance aperture will be imaged off the occulting mask. MOMI's primary function is to image faint nebulosity around bright stars, although, with the 3″ diameter (INT) mask currently used in MOMI, the light in the seeing disk is removed, a considerable amount of light remains in the diffraction pattern. The diffraction spikes caused by the telescope spines are of great concern as they overlay any faint nebulosity to a much greater radial extent than the Airy pattern.

A solution to the parasitic obscuration of faint light was first applied to the problem of imaging of the solar corona by Lyot (1939). Lyot empirically discovered that a mask in the focal plane of an instrument leaves light at the edge of the pupil (more generally at discontinuities in the pupil). The diffraction feet could be removed by a process now known as apodisation (from the Greek α, to take away, and $\pi o \delta o \zeta$, foot; Jacquinot & Roizen-Dossier 1963). The method simply removes the bright areas in the exit pupil of an instrument, in the case of the Lyot stop, by obscuring the edge of the pupil. By apodising the exit pupil of his coronograph Lyot was able to study the solar corona and

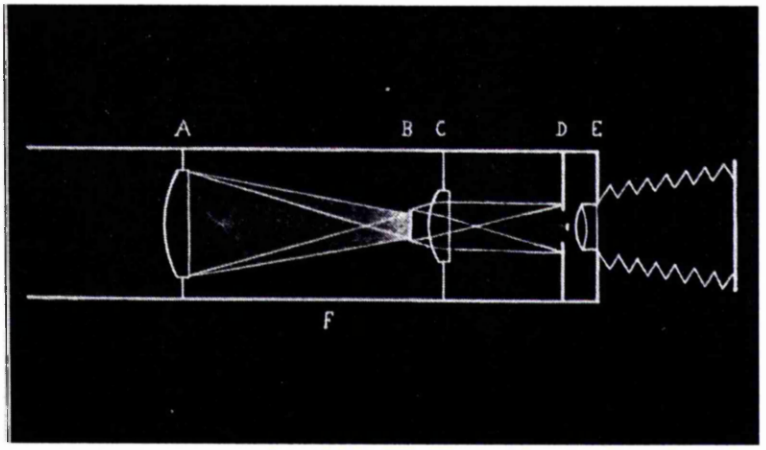

Figure 2.6: The Lyot coronograph. 'B' the occulting mask is in the focal plane of lens 'A'. Lenses 'C' and 'E' re-image the focal plane of 'A' plus the mask onto the detector (not labelled). 'C' also forms an image of the entrance pupil on 'D', the Lyot stop. After Lyot (1939).

prominences without eclipses. A sketch of the coronograph used by Lyot is shown in Fig. 2.6.

The process when applied to MOMI combined with a Cassegrain telescope, in which the secondary support obstructs the light a finite distance from the primary mirror, may be understood in terms of Fourier optics. The disturbance, due to a plane monochromatic incident wave, at a point in the focal plane of a lens, with a pupil function P projected in the aperture plane and centred on $(x = \frac{d_0}{f}\xi, y = \frac{d_0}{f}\eta)$, due to an obstruction, $t_0(x, y)$, at a distance d_0 in front of the lens is given by (Goodman 1968)

$$U(\xi,\eta) = \frac{A \exp\left[i\frac{k}{2f}(1-\frac{d_0}{f})(\xi^2+\eta^2)\right]}{i\lambda f} \times \int_{-\infty}^{\infty}\int_{-\infty}^{\infty} t_0(x,y)\ P(x+\frac{d_0}{f}\xi, y+\frac{d_0}{f}\eta)\ \exp\left[-i\frac{2\pi}{\lambda f}(\xi x+\eta y)\right]dxdy, \tag{2.2}$$

where x, y and ξ, η are coordinates attached to the secondary obstruction and image planes respectively, $t(x,y)$ is the aperture transmission function of the secondary obstruction (which may be complex), λ is the wavelength of the incident light, $k = \frac{2\pi}{\lambda}$ and f is the effective focal length of the telescope. If the projected pupil includes all the aperture for all points in the focal plane which contribute significantly to the amplitude spread function then

$$U(\xi,\eta) = \frac{A \exp\left[i\frac{k}{2f}(1-\frac{d_0}{f})(\xi^2+\eta^2)\right]}{i\lambda f} \times \int_{-\infty}^{\infty}\int_{-\infty}^{\infty} t_0(x,y) \exp\left[-i\frac{2\pi}{\lambda f}(\xi x+\eta y)\right] dxdy. \qquad (2.3)$$

In the focal plane of the lens, following the aperture, i.e. the telescope's Cassegrain focus, the amplitude function, $U'(\xi,\eta)$, is given by

$$U'(\xi,\eta) = \begin{cases} U(\xi,\eta) & \xi,\eta \notin \mathbf{\Sigma} \\ 0 & \xi,\eta \in \mathbf{\Sigma}. \end{cases} \qquad (2.4)$$

That is to say the amplitude within the area of the mask, and outside the field stop defined by the edge of the occulting mask substrate, $\equiv \mathbf{\Sigma}$, is identically zero.

It is the intensity distribution and not the amplitude distribution that is normally measured in the focal plane. A CCD, for example, would measure $|U'(\xi,\eta)|^2$ and the quadratic phase factor is unimportant. Thus the intensity

distribution in the telescopes focal plane is given by

$$I(\xi,\eta) = \frac{A^2}{\lambda^2 f^2}\left|\int_{-\infty}^{\infty}\int_{-\infty}^{\infty} t_0(x,y)\,\exp\left[-i\frac{2\pi}{\lambda f}(\xi x+\eta y)\right]dxdy\right|^2. \quad (2.5)$$

Immediately following the telescope's focal plane is the field lens–Tessar combination with a focal length, $f_{\rm fl}$. Incident on this lens is a disturbance $U_{\rm fl}(\xi,\eta) = U'(\xi,\eta)$, the amplitude distribution behind the lens is given by

$$U'_{\rm fl}(\xi,\eta) = U_{\rm fl}(\xi,\eta)P_{\rm fl}(\xi,\eta)\,\exp\left[-i\frac{k}{2f_{\rm fl}}(\xi^2+\eta^2)\right], \quad (2.6)$$

where $P_{\rm fl}(\xi,\eta)$ is the pupil function of the lens defined by

$$P_{\rm fl}(\xi,\eta) = \begin{cases} 1 & \text{inside the lens aperture.} \\ 0 & \text{otherwise.} \end{cases} \quad (2.7)$$

For a field lens with an aperture of sufficient size to accept the field within the field stop $U_{\rm fl}(\xi,\eta)P_{\rm fl}(\xi,\eta) = U_{\rm fl}(\xi,\eta)$. The amplitude distribution in the exit pupil of MOMI is given by the Fresnel diffraction formula (Goodman 1968),

$$U_{\rm epm}(x',y') = \frac{A\,\exp\left[i\frac{k}{2f_{\rm fl}}(x'^2+y'^2)\right]}{i\lambda f_{\rm fl}}\int_{-\infty}^{\infty}\int_{-\infty}^{\infty} U'_{\rm fl}(\xi,\eta) \times\exp\left[i\frac{k}{2f_{\rm fl}}(\xi^2+\eta^2)\right]\exp\left[-i\frac{2\pi}{\lambda f_{\rm fl}}(\xi x'+\eta y')\right]d\xi d\eta. \quad (2.8)$$

Substituting Eq. 2.6 into Eq. 2.8 and noting that the quadratic phase factors

cancel within the integrand leaves

$$U_{\mathrm{epm}}(x',y') = \frac{A\,\exp\left[i\frac{k}{2f_{\mathrm{fl}}}(x'^2+y'^2)\right]}{i\lambda f_{\mathrm{fl}}} \times \int_{-\infty}^{\infty}\int_{-\infty}^{\infty} U_{\mathrm{fl}}(\xi,\eta)\exp\left[-i\frac{2\pi}{\lambda f_{\mathrm{fl}}}(\xi x'+\eta y')\right]d\xi d\eta. \quad (2.9)$$

It is seen that the field lens performs the Fourier transform of the amplitude distribution in the Cassegrain plane at the exit pupil of MOMI scaled by a quadratic phase factor. It is now possible to apodize this pupil to remove any significant energy not removed by the finite occulting mask. The final image plane is again given by Eq. 2.8.

Analytical solutions for even the most simple occulting mask instrument are not straightforward to derive (Noll 1985; Wang & Vaughan 1988). Where there is a complicated aperture function, as in the case of a Cassegrain telescope, a repeated use of 2D Fourier transforms and a modern computer makes progress possible.

This system has been simulated for a Cassegrain telescope, in which the secondary mirror is supported by four equidistant struts, combined with MOMI. The aperture function is somewhat unwieldy and extensive use of Fast Fourier Transform (FFT) algorithms has been made. The resolution of the FFT grid is such that the struts have adequate sampling over them.

The entrance aperture of a large Cassegrain telescope ($t_0(x,y)$ in Eq. 2.2) is shown in Fig. 2.7, this is the initial array passed to the FFT algorithm. The focal plane image of a point source at infinity due to the aperture depicted

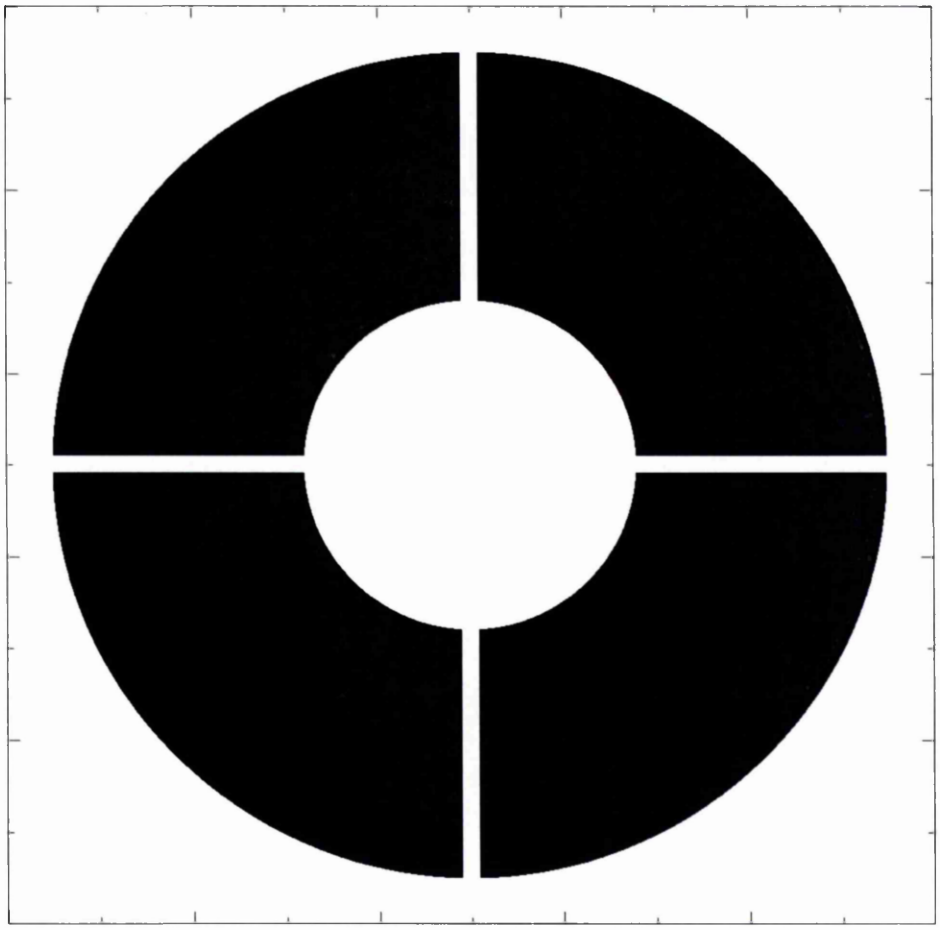

Figure 2.7: Entrance aperture of a Cassegrain telescope, obstructions are shaded white whilst areas of transmission are shaded black.

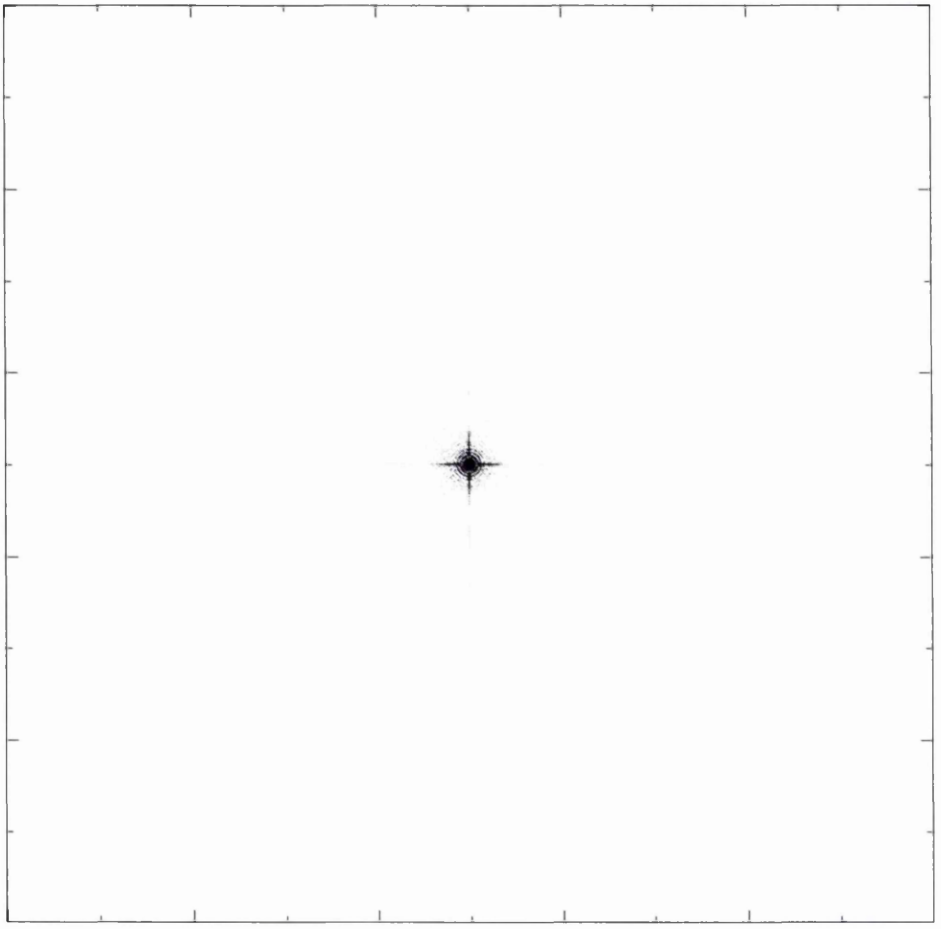

Figure 2.8: The Point Spread Function due to the obstructed pupil shown in Fig. 2.7.

in Fig. 2.7 is shown in Fig. 2.8. A cross-section through the centre of the pattern is shown in Fig. 2.9, the amount of energy in the diffracted pattern can be seen to be significant, the peak level is not shown but at the scale used would be several $\times 10^5$. A circular area, of diameter 400 μm ($\equiv 3''$), centred on the point spread function (PSF) is removed from the image to simulate the mask. Figure 2.10 is presented to illustrate the size of the mask in relation to the diffraction pattern, it can be seen that much of the light has

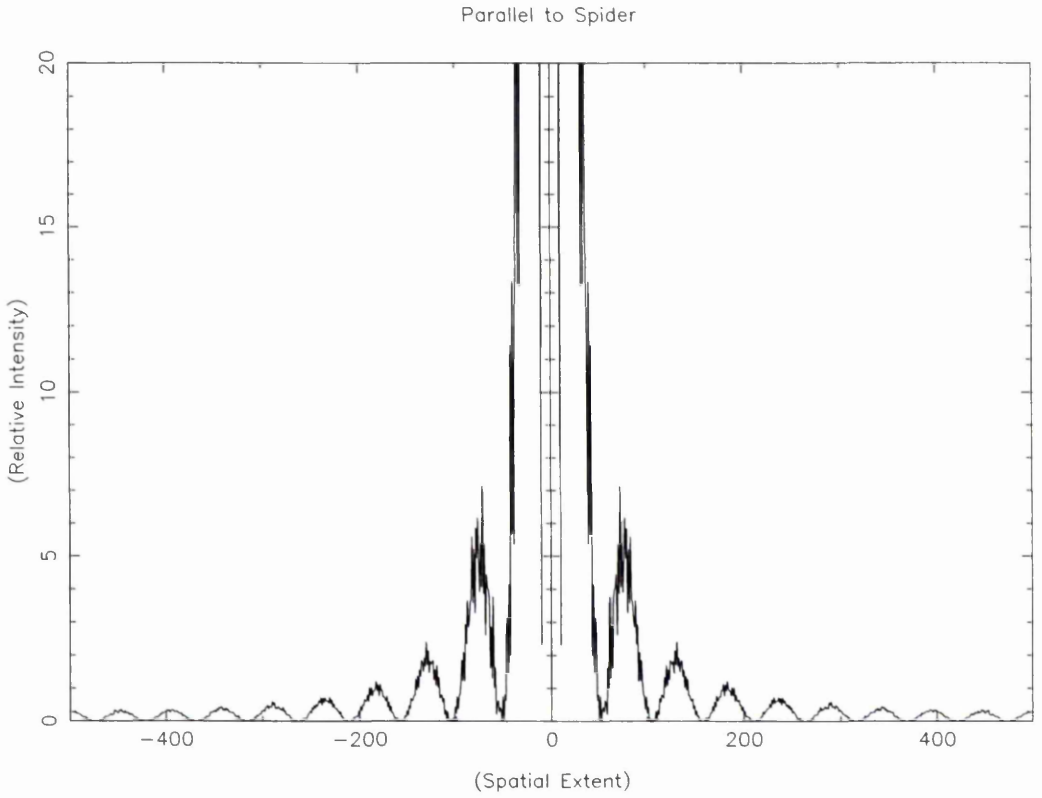

Figure 2.9: A cross–section through the centre of the Point Spread Function due to the obstructed pupil shown in Fig. 2.7. The peak level is not shown but at the scale used would be several $\times 10^5$

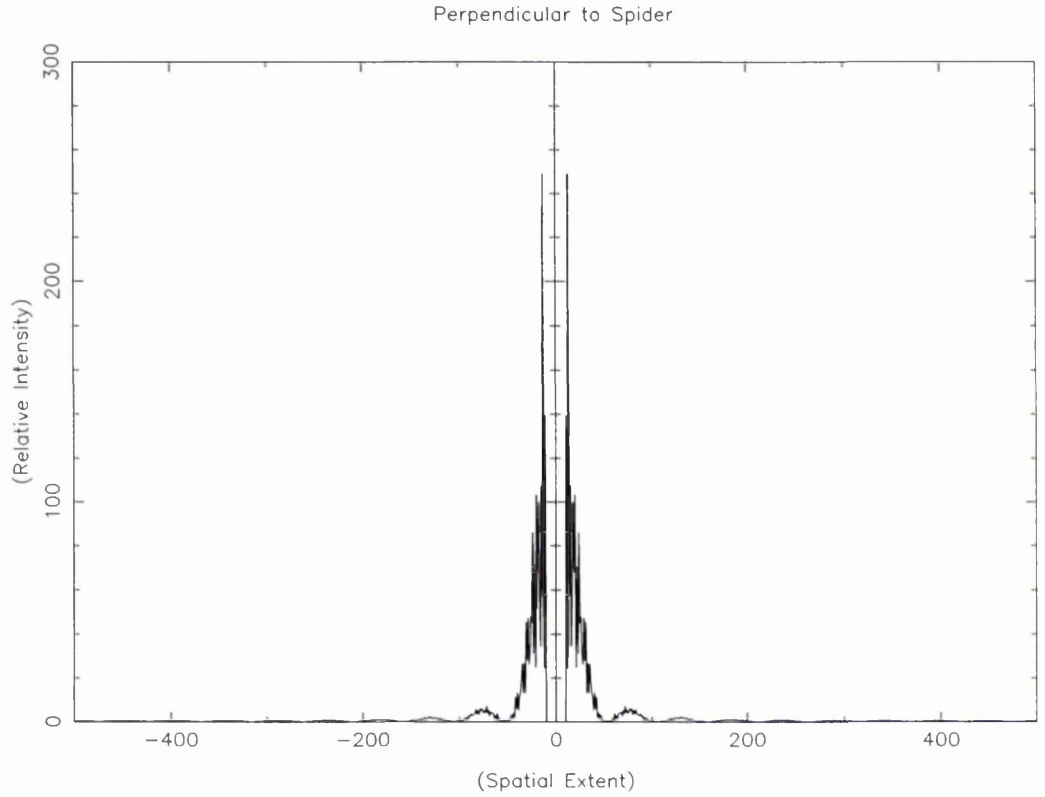

Figure 2.10: A cross–section through the centre of the Point Spread Function due to the obstructed pupil shown in Fig. 2.7 with the occulting mask placed over brightest part. The mask is the same diameter as that used with MOMI combined with the NOT. The intensity scale is the same as for Fig. 2.9.

not been removed, particularly in the diffracted side–lobes associated with the secondary support struts, but also in the circular diffraction rings associated with the circular aperture. In Fig. 2.11 the function illustrated in Fig. 2.10 has been transformed and the squared modulus taken. This is the response in the exit pupil on MOMI to a point source at infinity after the occulting mask has been applied. The important point to note is that the light is concentrated at the discontinuities in the entrance pupil i.e. at the edges of the obscurations. It is now easily seen that if a mask is placed in the exit pupil which obscures the light areas in Fig. 2.11 much of the remaining energy, not removed by the

mask, will be removed from the system. The shape and dimensions of the mask will simply be an exaggeration of the entrance pupil. An example mask is shown in Fig. 2.12 in the exit pupil, the resulting image at the detector is shown in Fig. 2.13. Figure 2.13 also illustrates the disadvantage of the apodising mask, the telescope's effective aperture has been reduced and the secondary mirror and support strut obscurations have effectively increased in size. This has the effect of increasing the FWHM of the PSF due to the circular aperture and reduced the collecting area of the telescope for all points in the field of view. The effectiveness of the apodising mask and occulting disk are best illustrated by a plot (Fig. 2.14) of a cross–section through the centre of the PSF. The benefits of a fully apodised system are clearly illustrated in the above example. The shape of the required apodising mask has been shown to be non-radially symmetric for the best rejection of the PSF of the occulted source. The asymmetry of the mask introduces a further level of complexity when MOMI is used in combination with an altazimuthly mounted telescope as the mask would need to be rotated in the opposite direction to that of the field de–rotator to maintain alignment with the entrance pupil. Rotation of the mask is not necessary when MOMI is used in combination with an equatorially mounted telescope.

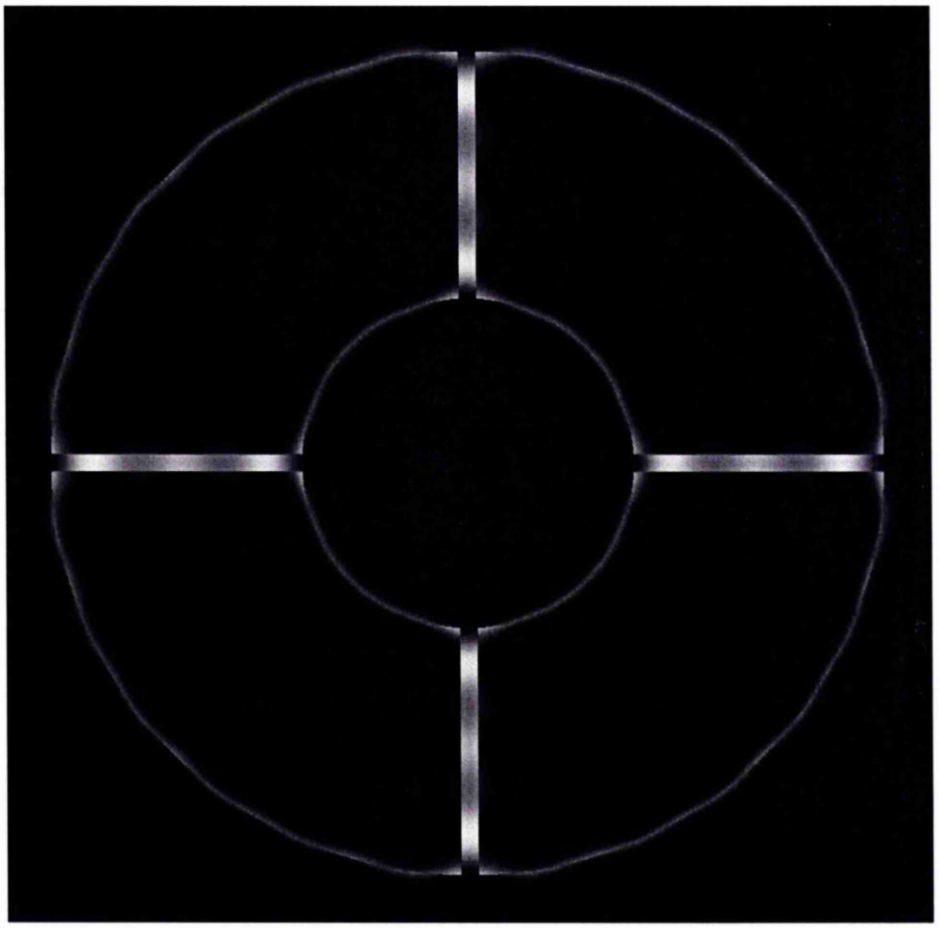

Figure 2.11: A greyscale representation of the light distribution in the exit pupil of MOMI in response to an occulted point source (Figs. 2.8 & 2.10)

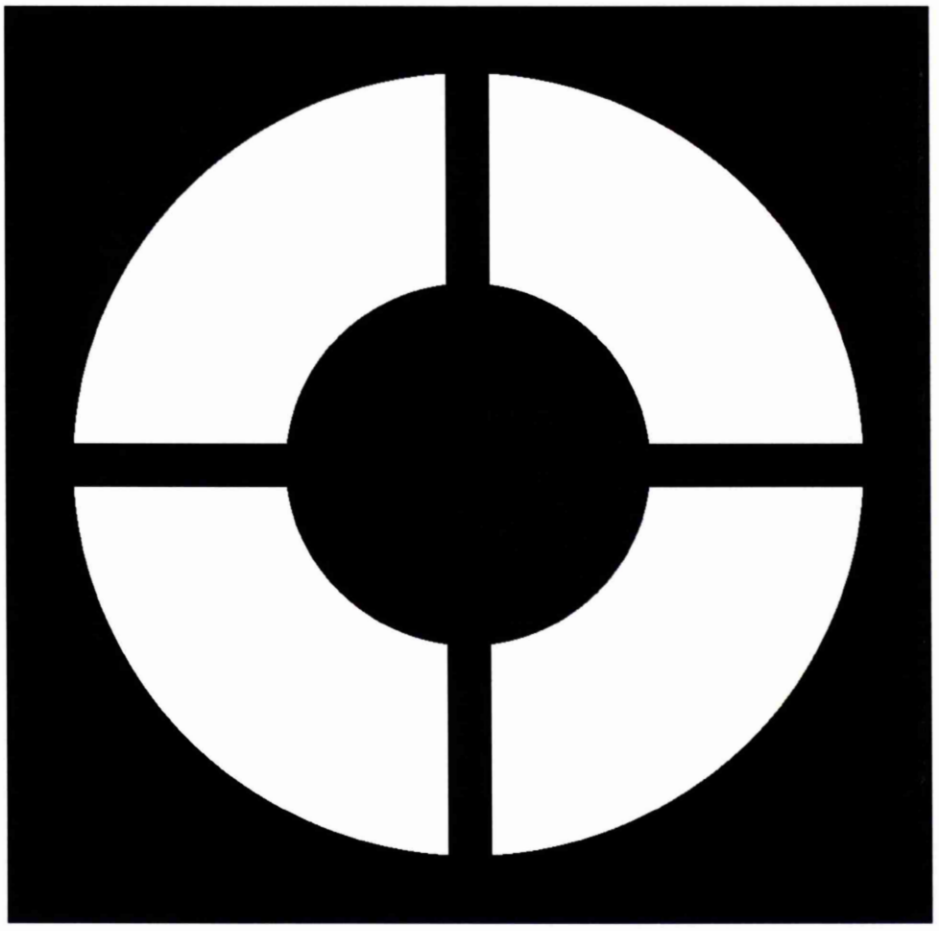

Figure 2.12: An apodising mask for the exit pupil of MOMI (Fig. 2.11), the dimensions of the obstructions (shaded black) are sufficient to remove the residual light from the pupil.

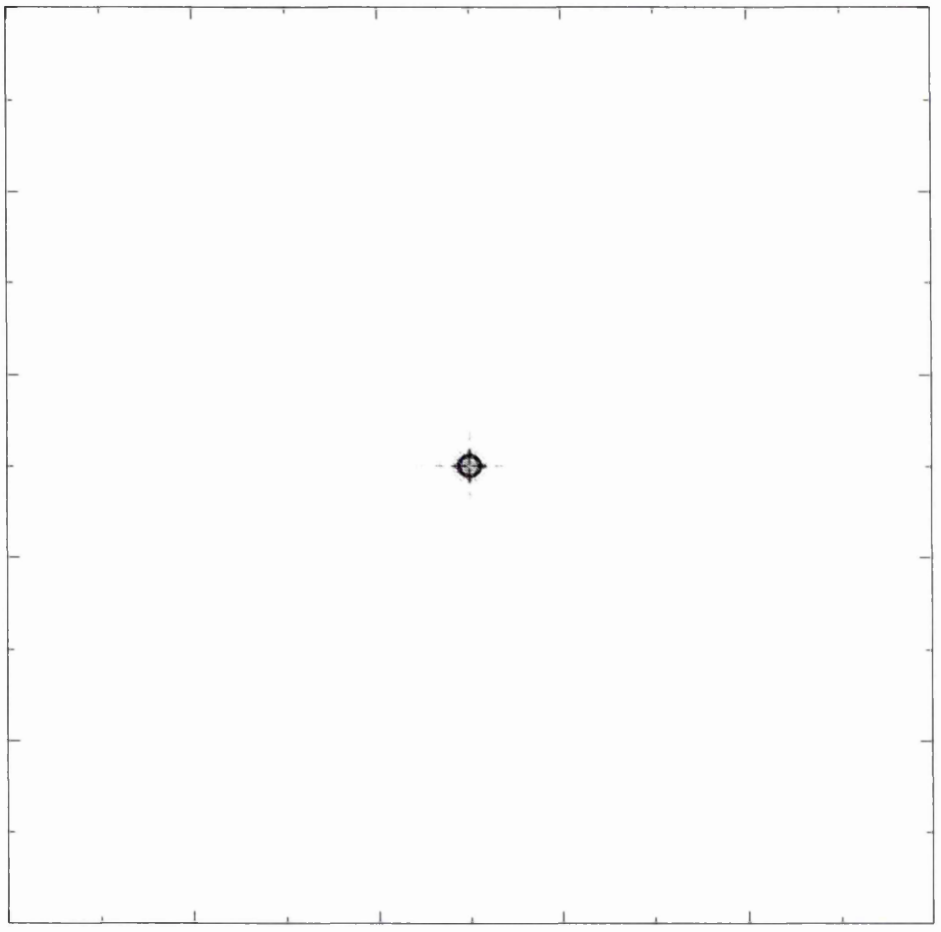

Figure 2.13: The final image at the detector, after apodisation of the pupil (Fig. 2.12). The image appears to be that obtained with a smaller aperture and with broader support spines as would be expected from Fig. 2.12.

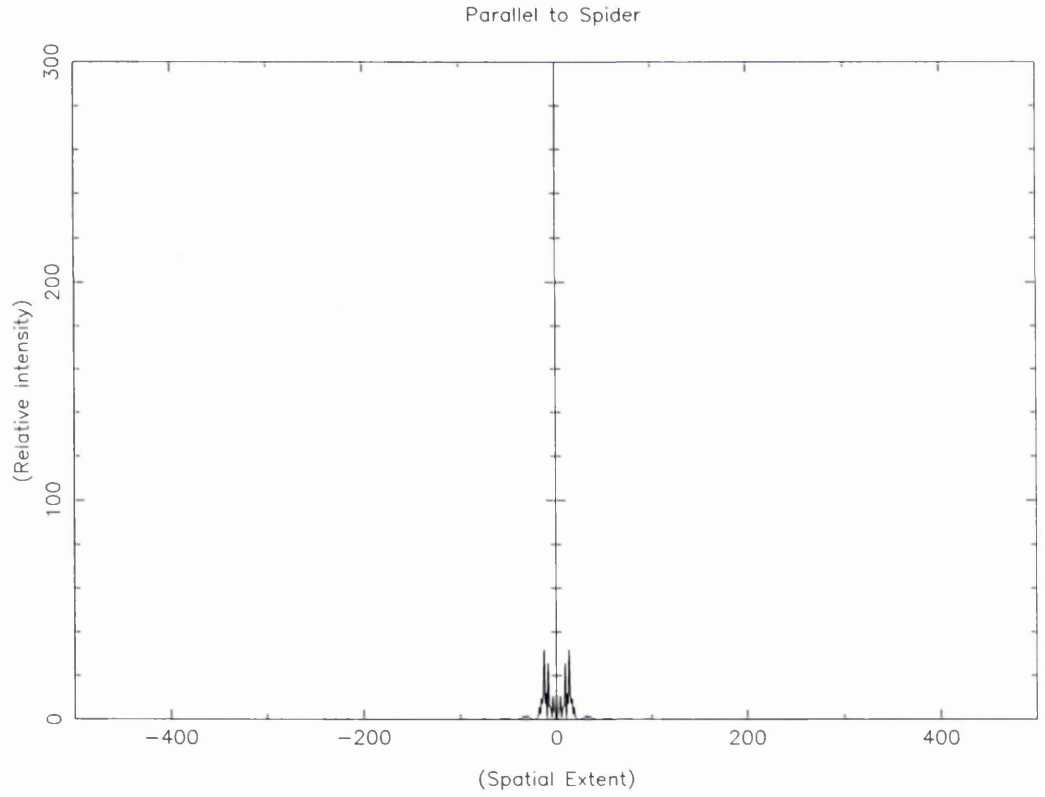

Figure 2.14: Cross–section through the centre of the final image at the detector after apodisation of the pupil (Fig. 2.12). The image appears to be that obtained using a smaller aperture and with broader support spines as would be expected from Fig. 2.12. The levels are greatly reduced as most of the energy from the point source has been removed by the occulting mask and the apodising mask. The intensity scale is the same as for Fig. 2.10.

2.4 Occulted scanning Fabry-Perot imagery

The forerunner of MOMI was a two–beam scanning Fabry-Pérot interferometer (Meaburn & White 1982) and some of its functionality has been retained in the new instrument. A pressure chamber has been retained in a collimated beam and coincident with a pupil. It is therefore possible to scan Fabry–Pérot etalons in wavelength (see Appendix B) by changing the refractive index of the surrounding gas by changing the pressure of the gas (Meaburn 1976).

A Fabry–Pérot etalon has been acquired for use with MOMI. The etalon was tailored to meet the demands of the observation of the shells around P Cygni in both [N II] λ6584 Å and [Ni II] λ7378 Å . The inner shell has an expansion velocity of 140 km s^{-1} in the light of [N II] λ6584 Å but only 110 km s^{-1} in the light of [Ni II] λ7412 Å (Barlow et al. 1994). The outer, [N II] λ6584 Å emitting shell has an expansion velocity of 185 km s^{-1} (Meaburn et al. 1996a). The outer shell parameters place a greater constraint on the free spectral range of the etalon and therefore the etalon was specified to meet these criteria. For an unambiguous range in wavelength of 450 km s^{-1} at 7000 Å the free spectral range required is (10.51 Å) $\times$ (7000 Å)$^{-2}$. Using Eq. B.3, the plate separation required is 233 μm. The etalon has a reflective finesse, N_R, of 25, given by a coating reflectance of 0.89 (Eq. B.12). This implies a resolution of 0.42 Å ($\equiv$ 18 km s^{-1}). The etalon has an anti-reflection coating between 6500 Å and 7500 Å and its outside surfaces are tilted to reduce ghosting. The 50 mm operating diameter of the etalon is sufficient to accept the full field of MOMI combined with the INT and the 1024$\times$1024 24 μm Tektronix CCD.

In order to scan the above etalon (see Appendix B) through one order at 7000 Å the refractive index, μ, of the surrounding gas must be increased by $1.43\times\ 10^{-3}$. This may be accomplished, when the etalon is immersed in nitrogen, by increasing the pressure of the gas to 5.1 atm above atmospheric. Much lower pressures may be used if the scanning gas is propane (C_3H_8), the refractive index change required could be achieved by a pressure change of only 1.3 atm above atmospheric (Meaburn 1976).

2.5 Data reduction

2.5.1 Charge Coupled Devices

An understanding of the basics of the Charged Coupled Device (CCD) is necessary for the correct reduction of data acquired. A CCD is a 2-dimensional array of photon counting cells. Each cell or pixel has a linear response to the light falling on it and holds charge with stability over time-scales of up to 100,000 s. They are sensitive, to a varying degree (see Fig. 2.15), to light between 3500 Å and 1 μm. The data delivered by a CCD system can be decomposed into two parts, signal from the object being observed and noise. Following the formalism of Tyson & Seitzer (1988) the contributions to the raw data frame can be written as

$$\mathrm{RAW} = (\mathrm{OBJ} + \mathrm{LED} + \mathrm{SKY})(\mathrm{QE}) - \mathrm{SKIM} + \mathrm{BIAS} + \mathrm{RNOISE}, \quad (2.10)$$

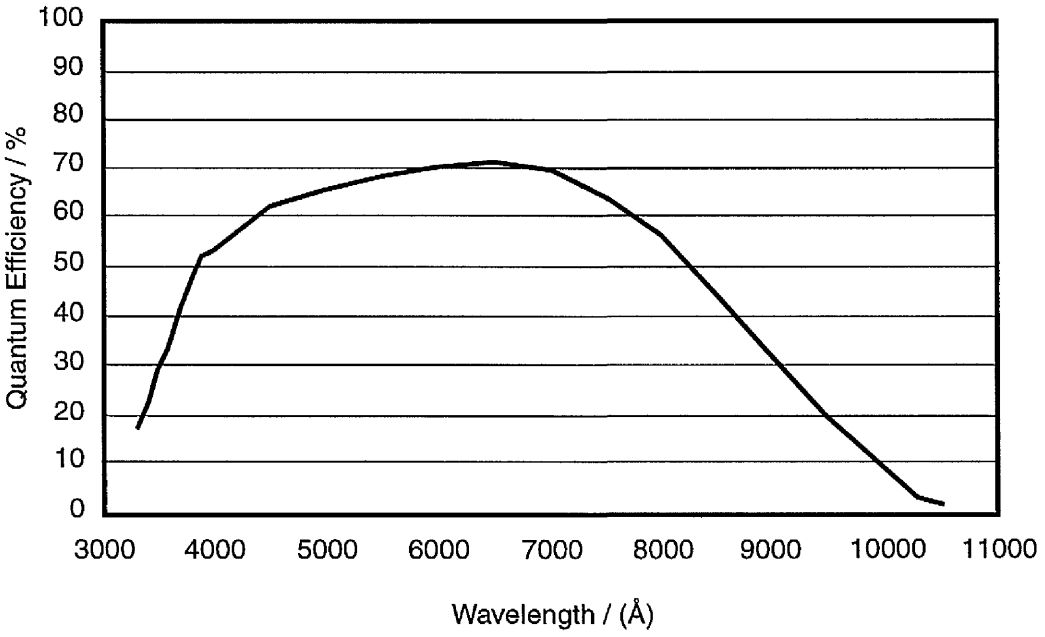

Figure 2.15: The spectral response of Tek5 1024×1024 24 μm CCD used as a detector with MOMI in combination with the INT.

where SKIM represents charge depletion, BIAS is the fixed pattern introduced by the CCD, RNOISE is the (random) read noise of the CCD, LED is the light-emitting-diode flux on the CCD or any other source of continuous additive signal, QE is the quantum efficiency of the CCD. OBJ and SKY are the fluxes from the object and the sky background respectively. Dealing with each component individually, SKIM occurs during the readout of a CCD and in modern chips can be ignored for the observations presented here. A BIAS charge is applied to the CCD chips to raise all cells above the zero level. The BIAS charge is therefore present in all readings acquired with the CCD and needs to be subtracted before processing takes place. LED or dark current occurs even when the CCD is not illuminated and can be calibrated out by

use of a suitable number of CCD integrations with the shutter closed with exposure times normalised to that of the RAW data. Again to follow Tyson & Seitzer (1988)

$$< \text{DARK} > = (\text{LED})(\text{QE}) - \text{SKIM} + \text{BIAS}, \tag{2.11}$$

where <> indicate that the mean of several integrations is normally required. In the reduction of data presented in this thesis dark frames were not necessary as the CCDs used had very low dark currents and did not suffer from bad columns. The RAW data is now considered, as reduced in the work presented here, to be

$$\text{RAW} = (\text{OBJ} + \text{SKY})(\text{QE}) + \text{BIAS} + \text{RNOISE}. \tag{2.12}$$

The QE factor varies from pixel to pixel and can be broken down into a number of components not necessarily directly attributable to the CCD itself. There is a real QE variation pixel to pixel but also under this factor the effects of non-uniform transmission in the optics and non-uniform thinning (Lesser 1990) of the CCD are included.

The practical method of reducing the data acquired with a CCD by MOMI will now be discussed.

2.5.2 Bias frames

Bias frames are taken at the start and end of the night and are really zero time integrations. Normally five such integrations are made and a mean bias frame produced. In the data presented here the CCD is windowed for each exposure during the night and bias strips record the bias level at the time of each exposure. This level can then be used to scale the mean bias frame allowing the endpoint biases to be used throughout the night. The Starlink package CCDPACK is used to scale the mean bias to a zero averaged level before the bias strips scale this 'master bias' to the correct level. The application then takes a subset of the CCD data excluding the bias strips and subtracts the 'master bias' resulting in bias corrected data arrays corresponding to the detector area presented to the sky.

2.5.3 Flat fields

To calibrate the non-uniform response of the instrument/CCD system images of a photometrically flat field are made. For the observations presented here the dusk or early dawn sky was used in preference to artificially projected flat fields. Bias levels are subtracted from the flat field frames before a weighted combination of the multiple exposures is made to produce a 'master flat'. The master flat is normalised to have an average pixel value of one and its inverse applied as a factor to each data array.

Complications arise when automated algorithms are used to clean the flat fields of defects such as cosmic rays. The algorithms treat the occulting mask

as a cosmic ray and attempt to clean it. It thus proves necessary to patch the occulting mask with a local pixel average to allow the automated routines, such as CCDPACK, to function properly. This has no effect on the information derivable from the data as diffraction effects overwhelm the data very close to the mask.

2.5.4 Co–addition of multiple integrations

Although the occulting mask used in MOMI should theoretically extend the integration time by a factor of the order of 10^4 in practice this can never be achieved. Imperfect tracking of the field, scattering from the telescope and instrument optics and variations in 'seeing' place a significant amount of energy outside the occulting mask. The use of CCDs as detectors also places a restriction on the integration times as they are sensitive to cosmic rays. Integrations of much longer than 1000s become unuseable due to the large number of cosmic rays events detected by the chip[2].

For the observations of the faintest nebulosity in a field it is necessary to break long integrations into many sub–integrations and recombine by co–addition. In effect, a set of measurements are made on pixel sized areas of the sky. Poissonian counting statistics can then be assumed to give a reduction in random noise[3] of $\sqrt{n}$, where n is the number of measurements made, on the mean value. It is possible at this point to filter cosmic ray events out of the

[2]The sensitivity to cosmic rays varies from chip to chip.

[3]Readout noise will, however, not be reduced and will ultimately place a limit on the detection of faint light

data set as they tend to add significant signal to a measurement raising it above a nominal confidence level. The signal to noise reduction in the whole data set now depends on the sensitivity of the CCD to cosmic rays and the probability of a cosmic ray falling on a particular pixel position.

2.5.5 Removal of ghost images

Georgelin (1970) discussed the appearance of parasitic images when using interference filters to isolate emission lines in a Fabry–Perot interferogram. The optical arrangement of MOMI produces ghosts from the imperfections present (Fig. 2.16) in the interference filter in the detector plane. The ghosts are unique to each filter and can be considered to be part of the point spread function (PSF) of MOMI when used with a particular filter. Various methods can be devised for removing the filter ghosts. As the ghost is essentially part of the PSF it is possible to deconvolve an empirical PSF from an image. Two other alternatives rely on changing the position of the ghosts with respect to the field which can be accomplished by either rotating the field on the mask or reversing the filter orientation.

If the filter ghost can be placed away from the central maximum (Fig. 2.17) of the PSF by tilting the filter it is possible to reverse the orientation of the filter and place the ghost on the opposing side of the PSF. The pass–band characteristics of an interference filter should be identical at either orientation. This gives two sets of data with pixel values given (after standard data reduction)

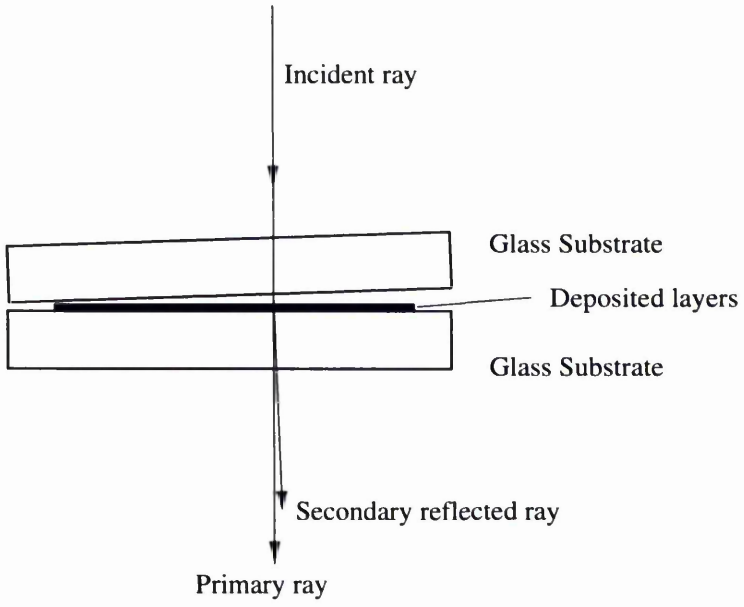

Figure 2.16: The ghosts produced by an interference filter can have their origins in the imperfections in the substrates used to support the dielectric interference layers. Here an error in parallelism produces a secondary ray which may contribute to a ghost image in the focal plane.

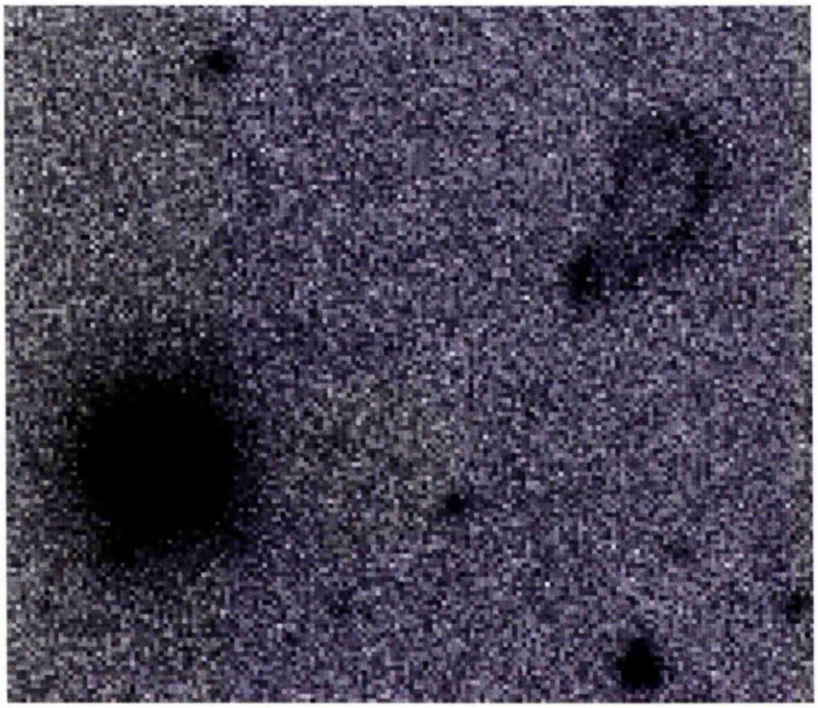

Figure 2.17: The ghost produced by a 70 mm diameter [N II] λ6584 Å interference filter tilted by 3.2 ° away from the optical axis displays a well behaved pattern to one side (top right) of the main PSF.

by

$$\mathbf{A}_{ij} = \mathbf{O}_{ij} + \mathbf{G}_{ij}$$

$$\mathbf{B}_{ij} = \mathbf{O}_{ij} + \mathbf{G}'_{ij}.$$

where $\mathbf{O}$ are the images of the object and $\mathbf{G}$ and $\mathbf{G}'$ are the ghosts produced by the filter in the normal and reversed orientations respectively. If the two sets of data are combined the resulting array has pixel values of

$$\mathbf{C}_{ij} = 2 \times \mathbf{O}_{ij} + \mathbf{G}_{ij} + \mathbf{G}'_{ij}. \tag{2.13}$$

It is critical that the ghosts are not coincident for, if this condition is satisfied, the modulus of the difference between the two images ($|\mathbf{G}' - \mathbf{G}|$) is equal to the sum of the two ghosts ($\mathbf{G}' + \mathbf{G}$) and this array may be subtracted from $\mathbf{C}$ to leave

$$\mathbf{D}_{ij} = 2 \times \mathbf{O}_{ij}. \tag{2.14}$$

Chapter 3

Manchester echelle spectrometer

3.1 Introduction

The two Manchester echelle spectrometers (MES – Meaburn et al. 1984) were designed for problems which require the detection of faint light over an extended field of view, within very small wavelength ranges but at high resolution. The first was commissioned in 1983 on the Anglo-Australian telescope (AAT) and the second in 1986 on the William Herschel telescope (WHT). Both initially used IPCS as the detector (Boksenberg & Burgess 1973) but were later combined with CCDs.

There are several properties of an echelle reflection grating which lend themselves to the observation of faint emission lines from extended sources. Firstly, an echelle can have a wider slit at a given spectral resolution (i.e. a higher

luminosity × resolution product; L×R; Jacquinot 1954) than a conventional spectrometer using first or second order gratings. Secondly, each spectral element may be recorded simultaneously by 2D television like detectors and, with a long slit and suitable filtering of the orders, each spectral element over a range of spatial elements may be recorded simultaneously.

The sacrifice made to achieve the high L×R of an echelle is of a lowering of the free spectral range. For example the inter-order separation of the echelle grating used in MES is 75 Å at 6500 Å. It is for this reason that many of the astronomical echelle spectrometers manufactured employ a cross-dispersive element to separate the orders. This method allows these devices to simultaneously record spectral elements over many thousands of angstroms but of a reduced spatial extent. As a consequence, these cross-dispersed echelles are principally applied to the investigation of single, faint sources of small angular extent, which emit over a broad range in wavelength. MES, however filters the incident radiation in wavelength prior to the echelle with broad (100 Å) interference filters to isolate echelle orders. In this way it is possible to produce high resolution spectra over a wide spatial extent but over a limited spectral range.

In the present instrument the spatial extent of the spectra is not limited to a single slit. Multiple slits, separated spatially at greater angular distances than the expected dispersion scale, may be used to acquire up to five spectra at differing positions on the sky. In work where full 3D velocity maps are required this ability reduces the time needed by a factor of up to five. Multi–

configuration masks may be used where either similar criteria to the use of multi-slits must be met or a unique position in the spatial direction for each element is used. This facility also allows for the use of optical fibres (Matador – Clayton 1987).

3.2 Data Reduction and analysis

This section will deal only with the reduction of narrow–bandwidth longslit spectra acquired with MES and narrow–bandwidth imagery.

3.2.1 Spectrometric mode

The non–cross dispersed mode of MES allows extended areas of sky to be analysed. The data have two dimensions, a spatial dimension equivalent to the patch of sky which is imaged on the slit and a wavelength dimension. In the following discussion it is assumed that the spectra are imaged onto a 2D detector and that this detector has an $n_i \times n_k$ array of bins into which the light falls (such as a Charged Coupled Device – CCD). Thus, when discussing spectra, rows of bins are termed increments in the spatial direction and channels in the direction of dispersion.

Wavelength calibration

When analysing high–resolution longslit echelle data one is often most interested in determining velocity information over an object. It is therefore

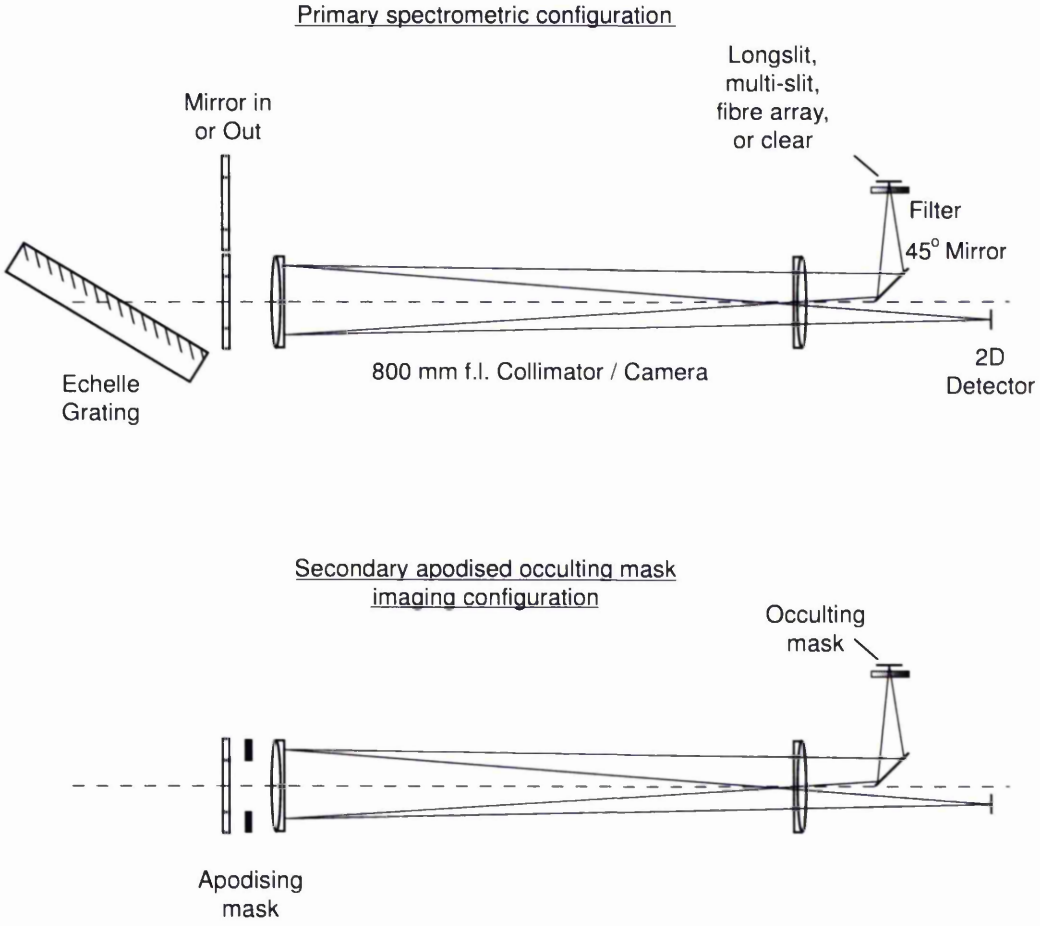

Figure 3.1: The two common modes of operation of MES are spectrographic (Top) and imaging or coronographic (Bottom).

necessary to accurately calibrate the spectra in wavelength along across all increments. To allow this procedure to be performed spectral images of known emission lines are acquired after each science integration[1]. Arc lamps in the telescope's chimney are used as sources for the calibration lines and the same narrow–bandwidth interference filter as is used to isolate the science spectra isolates the calibration spectra.

The difference in distance of each point along the slit from the echelle grating causes spectral lines to be curved across the detector (Fig. 3.2 and Appendix C). After de-biassing and removing any parasitic features, such as cosmic ray hits, Gaussian profiles are fitted to the features corresponding to emission lines of known wavelength across all increments. This almost automated process is performed with software from Starlink's TWODSPEC package. It is often necessary to bin–up the calibration data from multiple increments to increase the signal to noise ratio for the fainter arc-lines. Third order polynomial fits are made to the (binned) curved arc-lines to allow accurate Gaussian profile centres along the full length of the unbinned line to be determined. For each increment along the slit length a dispersion measure is calculated from the fitted Gaussian centres and the known wavelengths of the emission lines from the arc lamp. With the dispersion measure known a program from Starlink's FIGARO package, ISCRUNCH, is used to rebin the data.

A one–dimensional spectrum is shown in Fig. 3.3 of the emission lines from a

[1]This minimises differences in instrumental performance between science and calibration exposures.

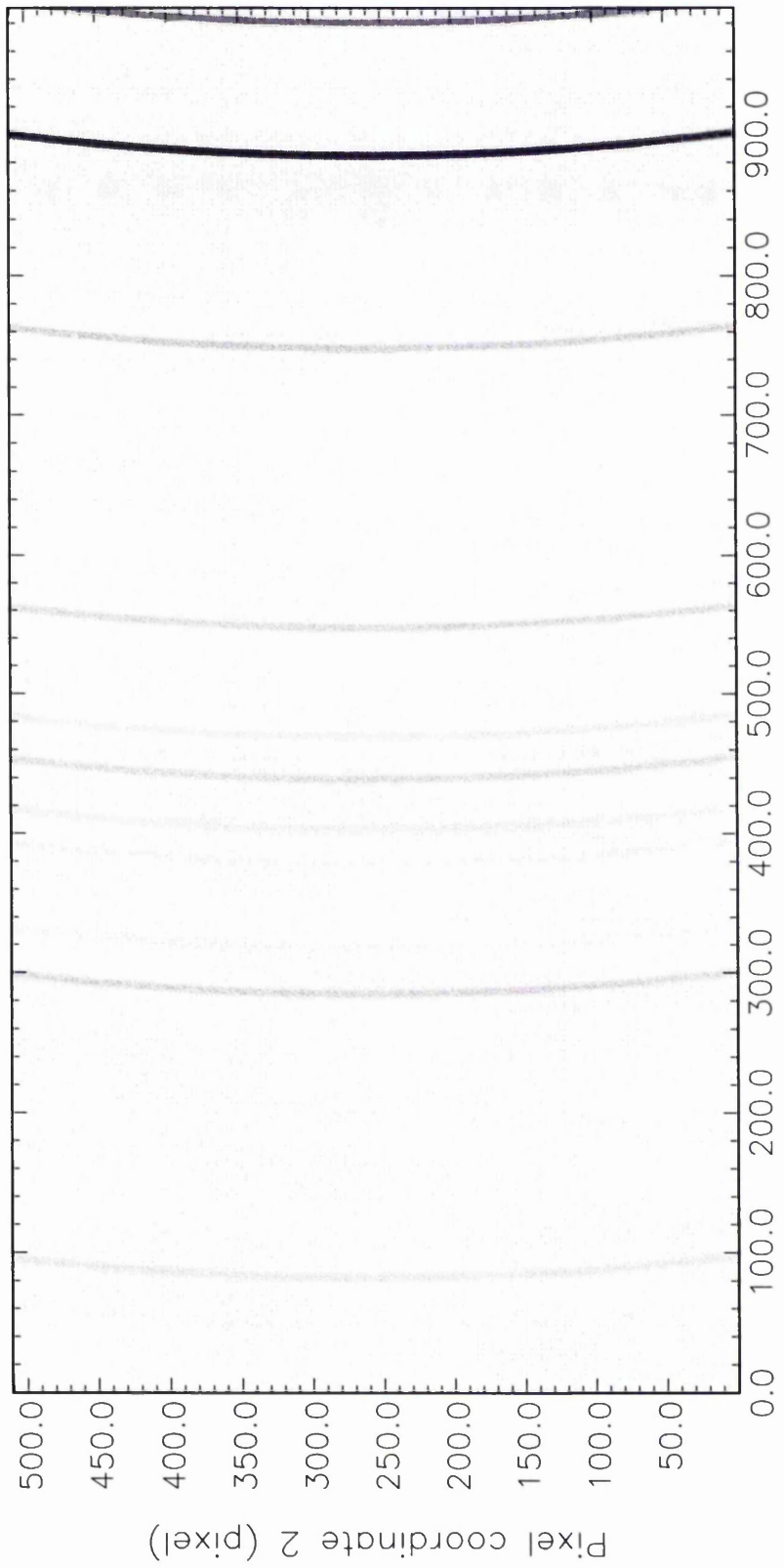

Figure 3.2: Greyscale plot of spectra from a ThAr arc–lamp across the field of view of a longslit. Note the curvature as the transmission maxima satisfies the echelle equation over the length of the slit.

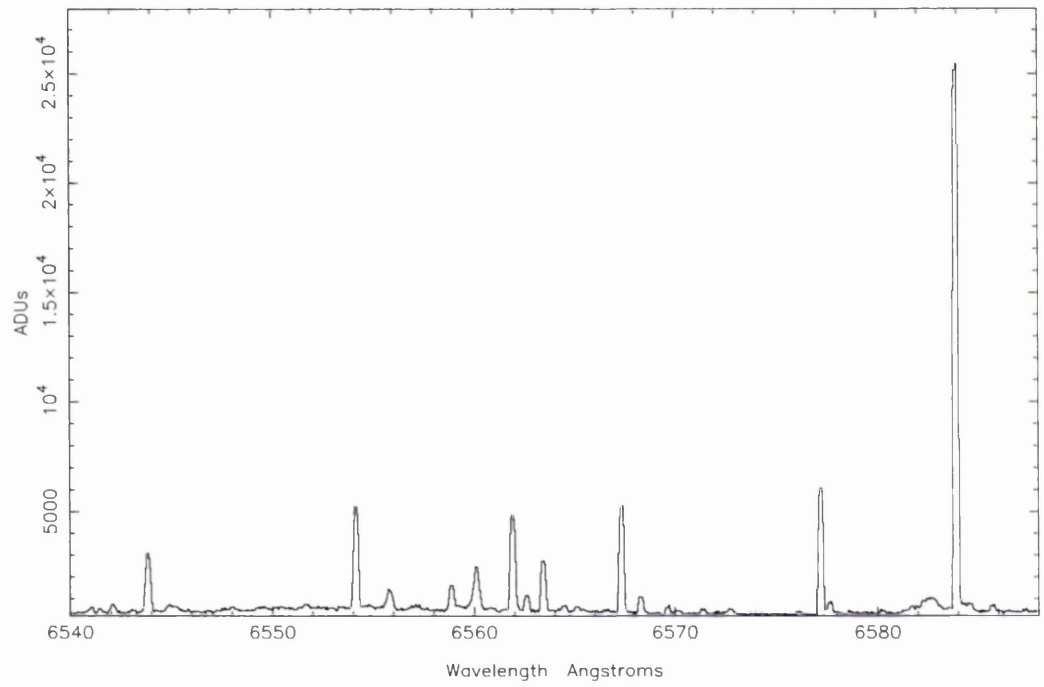

Figure 3.3: The spectral lines of ThAr in the region of Hα and [N II] λ6584 Å.

thorium–argon (ThAr) arc lamp between 6540 Å and 6588 Å. This appears in the 87th echelle order and is isolated by a 100 Å interference type filter centred on 6570 Å. This area of the spectrum contains the two forbidden nitrogen lines [N II] $\lambda\lambda$6548, 6584 Å and Hα. Parasitic lines can originate in both the neighbouring orders (within the passband of the order filter) or much longer wavelengths outside the effective blocking range of the order filter but still within the working bandpass of the detector. The 'leak lines', as they are known, are broader than the intrinsic lines due to lower spectral resolution away from the working order. The 'leak lines' from much longer wavelengths are known as the 'red leak lines' and may be removed from the system with a 'hot mirror' – a broad filter which attenuates at wavelengths greater than 7500 Å.

An example of a wavelength calibrated arc–line spectrum is shown in Fig. 3.4, it should be noted that as the science data was positioned between increments 300 and 400 in this instance, it was only necessary to calibrate the spectra over these increments.

Intensity calibration

Where photometric information is required it is necessary to calibrate the spectra for changing instrumental efficiency over the field (in wavelength and space). This is most easily accomplished by a technique, referred to as 'flat fielding', where a spectrally and spatially 'flat' source is imaged through the spectrometer. The varying sensitivity measured across the field may then be used to normalise the science spectra. This technique alone normalises sensitivity over the longslit spectra which allows relative measurements of intensity to be made. For absolute measurements the spectra must be calibrated against a known source. MES has a parasitic, ghost image of the longslit which falls onto the detector. This is easily recognised as it is not dispersed by the echelle grating and therefore does not exhibit curvature. It is necessary to remove this ghost prior to any flat-fielding and preferably prior to scrunching.

Emission line profile fitting

It is well known that much information is contained within the profile of an emission line. In many cases this can only be retrieved after a careful analysis in which the profile is modelled as a number of individual velocity components.

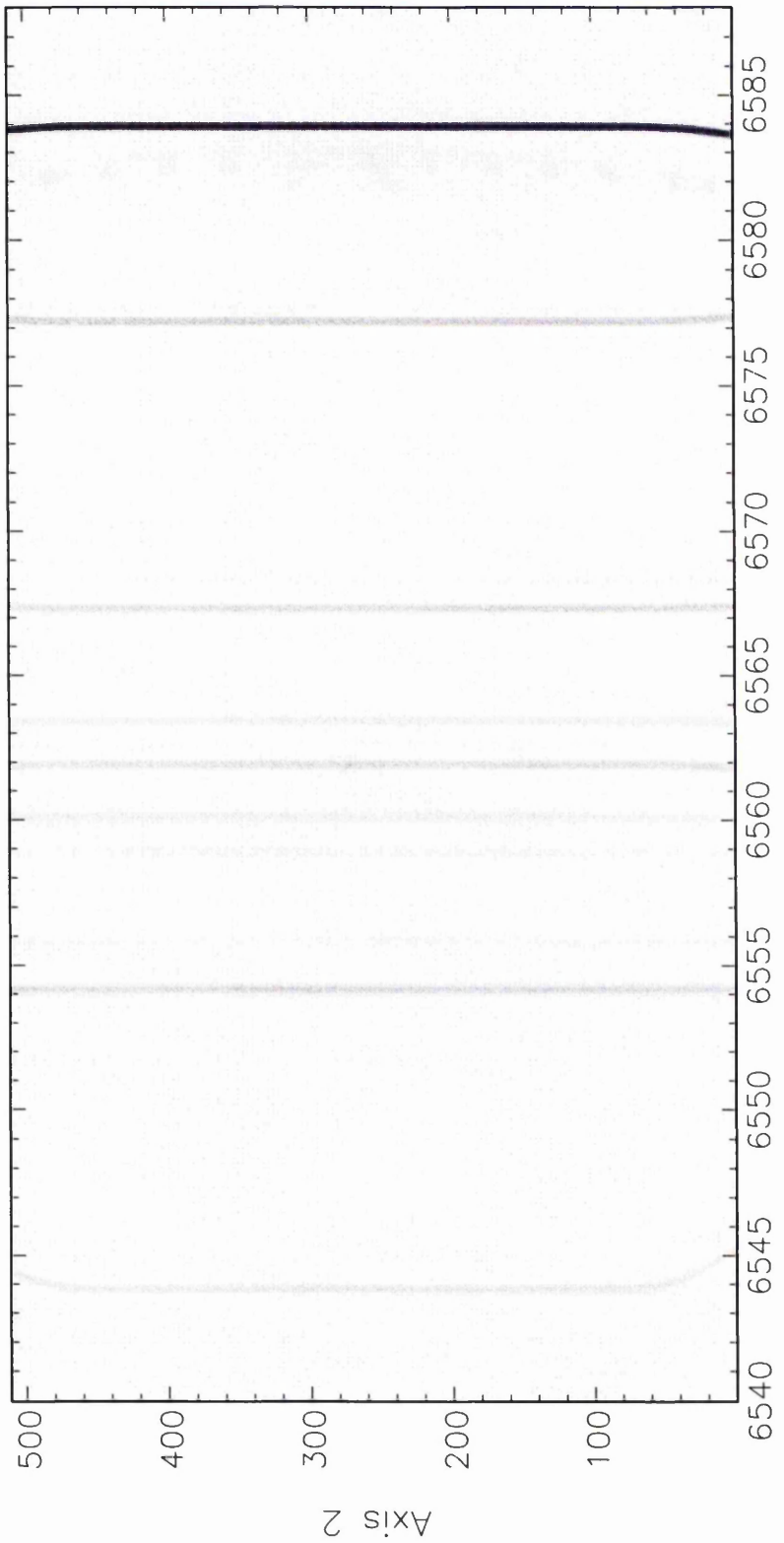

Figure 3.4: For a 'rule of thumb' test of the scrunch parameters the calibration arc–lines are scrunched, if the lines are straight across the area of interest then the scrunch parameters are in the right ball-park.

Simple kinematical information may, in many cases, be deduced from simple inspection, where this is not possible multiple Gaussian profiles may be employed to reveal obscured details. In this thesis extensive use has been made of Starlink's TWODSPEC package to iteratively fit single and multiple Gaussian profiles.

The widths of emission line profiles obtained with any spectrographic instrument are affected by several phenomena. The intrinsic width of a line may, in most cases, be treated as insignificant. A single emission line from a volume of gas is Doppler broadened by two distinct processes, thermal broadening and turbulent broadening. Thermal broadening is produced by the distribution of velocities in the emitting gas due to its temperature and is a well known phenomenon in the laboratory. Turbulent broadening is due to bulk motions within the volume of gas and is associated with flows or turbulent mixing. An extra broadening effect is due to the instrument and is known as instrumental broadening. The aforementioned effects are convolved with the intrinsic width of the emission line to produce the observed profile.

3.2.2 Imaging mode

If a plane mirror is placed in front of the echelle grating the MES behaves as a simple camera. The collimating optics are not entirely superfluous when used in this mode, however, as it is possible to operate MES as a Coronograph by placing an apodising mask at the pupil formed by the collimator and an occulting mask at the Cassegrain focus.

Data acquired with MES in imaging mode is reduced in a similar fashion to that acquired with MOMI and the reader is referred to §2.5.

Chapter 4

First use of MOMI – Results on the environs of P Cygni

4.1 Introduction

The nebulosities surrounding luminous blue variables (LBVs) are of considerable interest for they are the relics of the most recent eruptions of these stars. Expanding shells of circumstellar gas have now been found around six galactic LBVs (see Barlow et al. (1994) and Nota et al. (1995) for a summary of these observations). So far, two distinctly different shells have been found (Barlow et al. 1994) with occulting–mask imagery around P Cygni (V = 4.8 mag). A bright inner shell (IS), $\approx$ 22″ diameter, has a radial expansion velocity of 140 km s^{-1} in the [N II] λ6584 Å line but only 110 km s^{-1} in the exceptionally bright [Ni II] λ7412 Å lines. A fainter, outer, [N II] λ6584 Å emitting shell (OS) of $\approx$ 1.6 arcmin diameter has been shown to be expanding

at 185 km s^{-1} to give a kinematical age of 2100 yr for a distance of 1.8 kpc to P Cygni (Meaburn et al. 1996a).

The results from the first use of MOMI on the Nordic Optical telescope (NOT) are presented here. MOMI was used to image the nebula surrounding P Cygni in the light of [N II] λ6584 Å. The instrumental performance of MOMI on the NOT is discussed in the light of these new results. Further results obtained during commissioning of MOMI on the Isaac Newton telescope (INT) are also presented. For comparison with the [N II] λ6584 Å images obtained with MOMI on the NOT, images of the inner shell of P Cygni were obtained in the light of [Ni II] λ7378 Å .

4.2 Observations and results

For the observations at the f/11 Cassegrain focus of the 2.56-m NOT telescope the 710 mm focal length Tessar collimating lens combined with the 300 mm focal length 'off–the–shelf' Nikkor refocussing lens gives a field scale of $1'' = 0.058$ mm in the MOMI focal plane. With the LORAL 2048 $\times$ 2048 CCD, with 15 μ m ($\equiv 0.26''$) square pixels, the field size is 8.83 arcmin $\times$ 8.83 arcmin.

Figure 4.1. The full–field image in the light of [N II] λ6584 Å. North is to the top and East to the left.

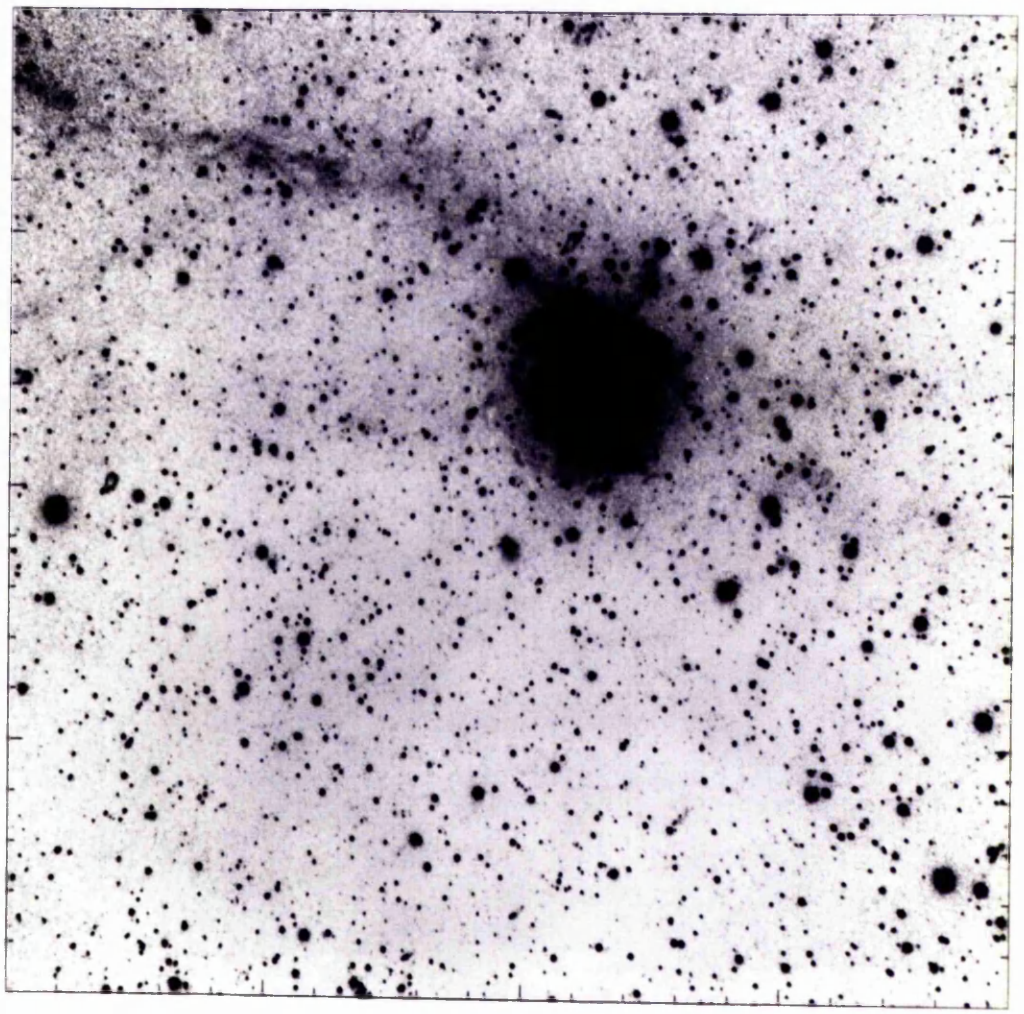

5 arcmin

Figure 4.2. The outer shell of P Cygni in the light of [N II] λ6584 Å. The bright feature to the NW of the star is a 'ghost' generated within the layers of the interference filter. North is to the top and East to the left.

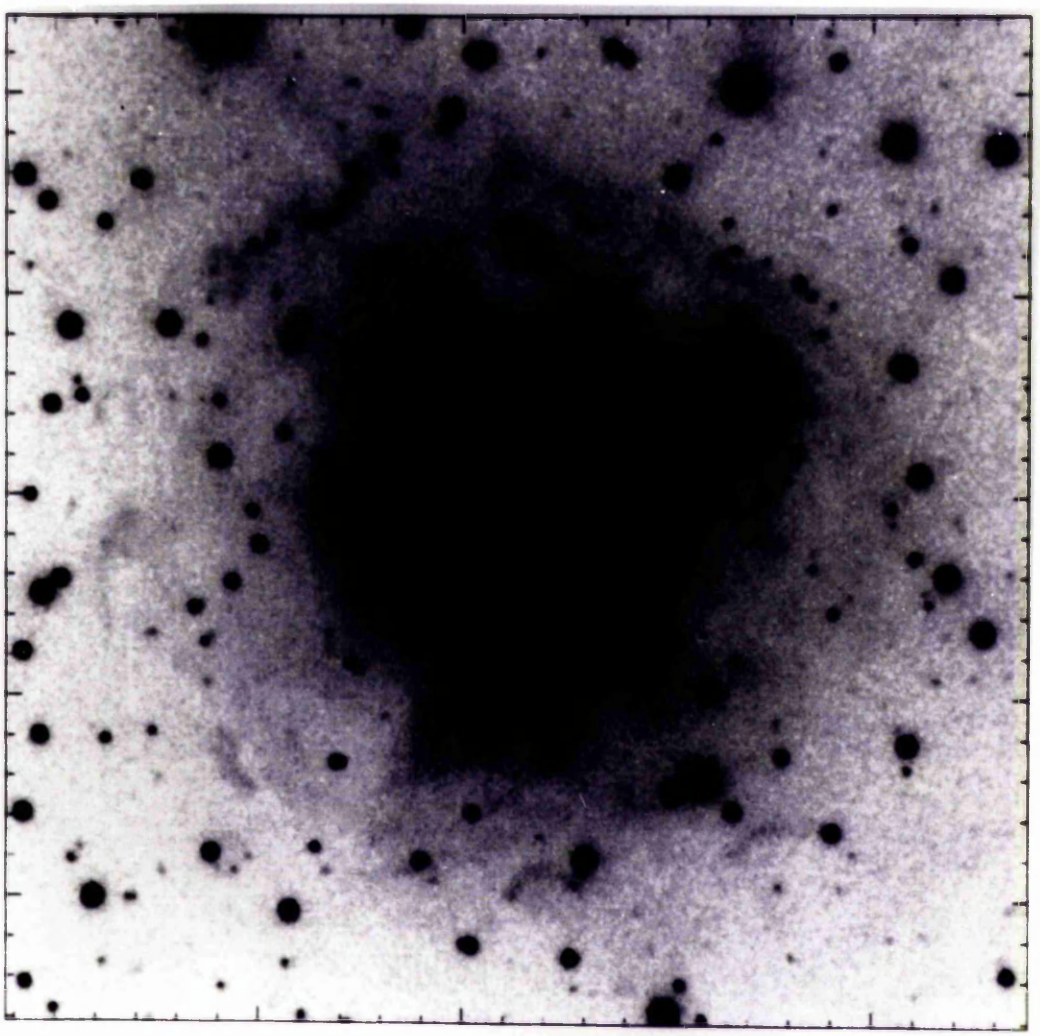

1 arcmin

Figure 4.3. A positive greyscale representation of the inner shell in the light of [N II] λ6584 Å. No attempt has been made to remove the prominent diffraction spikes. North is to the top and East to the left and the image covers an area of $33'' \times 33''$ centred on P Cygni.

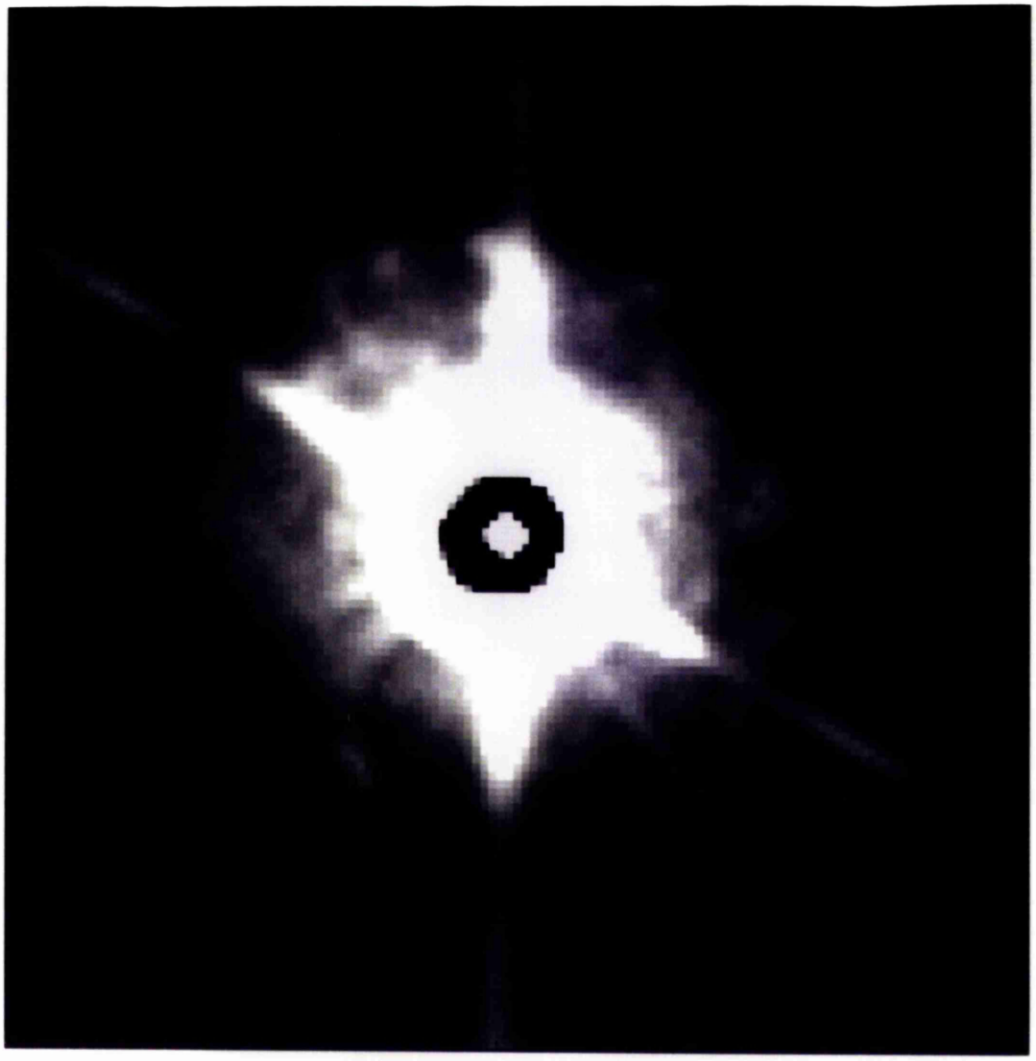

10 arcsec

Narrow band images of P Cygni in the light of [N II] λ6584 Å were obtained during the night of 1997 November 14. A thinned LORAL 2048 $\times$ 2048 15 μm CCD was used throughout these observations as a detector. A three–period (square profile), 20 Å bandwidth, interference filter was centred on the [N II] λ6584 Å nebular emission line by tilting it by 3.2°. Fourteen integrations, of 500 s each, were taken with P Cygni centred on the chromium spot.

The data were processed at the University of Manchester STARLINK node with programs from the CCDPACK, FIGARO and KAPPA packages. The data arrays were debiassed and any cosmic ray hits were removed. Flat–field corrections were applied using a combination of dusk sky exposures as a reference. The resulting frames were aligned and co–added to give an image with an effective integration time of 7000 s. A star of a similar brightness to P Cygni was also observed in a similar way to permit the correction of the residual scattered stellar continuum from P Cygni.

The full field of MOMI was not used due to a significant drop in quantum efficiency at two adjacent edges of the thinned Loral chip. The occulting spot, which is mechanically offset by a small amount from the centre of the chip, is further offset from the centre of the reduced image when the affected edges are removed from the data array.

A negative, high contrast, greyscale representation of the trimmed field (8.5 arcmin $\times$ 8.5 arcmin) is shown in Fig. 4.1. An arc of emission can be seen extending some 5 arcmin from the outer shell towards the North–Eastern corner of the image. There is a counterpart to this 5 arcmin arc to the south possibly

indicating the arc is one edge of a lobe.

In Fig. 4.2 a subsection of the full field array enclosing the outer shell is shown. Emission extending in the direction of the aforementioned arc is visible. Small bow shaped knots are apparent in the outer shell at distances 47″, 48″, and 52″ to the North–East, South and South–West of the central star respectively. The prominent dark feature to the North–West of the central star is an artifact produced by ghosting within the layers of the interference filter.

The inner shell is shown in Fig. 4.3 as a subsection of a single data array (500 s integration time) as a positive greyscale. A two dimensional analytical profile, with parameters taken from the continuum reference data, has been subtracted from the P Cygni data in this image. The central star is seen through the mask. Filamentary loops and arcs, particularly to the North–West, are most striking. Knots are found throughout the shell. Diffraction spikes from the spines of the secondary mirror are broadened due to the field rotation corrector of the altazimuthly mounted NOT. The central spike is due to a fine thread spanning the secondary mirror to secure an alignment cap. Over the full co–added data array the rotation of the field causes the diffraction spikes to confuse the image.

For comparison with the [N II] λ6584 Å images (Figs. 4.1, 4.2, 4.3) an image in the light of [Ni II] λ7378 Å was obtained with MOMI combined with the f/15 Cassegrain focus of the INT (1998 September 5). A Tektronix 1024×1024 CCD with 24 μm square pixels ($\equiv$ 0.31″) was used as the detector.

For these observations the central star was attenuated by a chromium occulting

spot which subtended an angle of 3″ on the sky. The [Ni II] λ7378 Å nebular emission line and the scattered continuum light were isolated by 10 Å bandwidth and 100 Å bandwidth (centred on 7390 Å) interference filters respectively. To allow for the removal of cosmic ray events and to limit the response of the CCD to within its linear range, ten integrations of 600 s were made. For half of the integrations the orientation of the interference filter was reversed to enable the subsequent isolation and removal of the filter ghost (O'Connor, Meaburn & Bryce 1998). The data were processed in the usual manner with programs from the CCDPACK and KAPPA packages at the University of Manchester's Starlink node. The processed arrays were aligned and co-added to give an array with an effective integration time of 6000 s. Although the seeing (measured from 10 s exposures not presented here) varied below 0″.8 the effective seeing, as measured from a star within the full field of MOMI, was 1″.2 due to an RMS tracking error of approximately 0.25″ during each integration.

A subsection of the processed data array including the IS in the light of [Ni II] λ7378 Å is shown on Fig. 4.4. The central star is apparent through the O.D[1]. = 4 occulting mask. The maximum extent of the IS in the light of [Ni II] λ7378 Å from the central star is 12″ (in the direction of North–East). The clumpy nature of the [Ni II] λ7378 Å emission within the IS is immediately apparent particularly to the North.

[1]Optical density.

Figure 4.4. A logarithmically scaled subsection of the data array containing the inner shell in the light of [Ni II] λ7378 Å . The spatial scale and orientation are identical to that of Fig. 4.3.

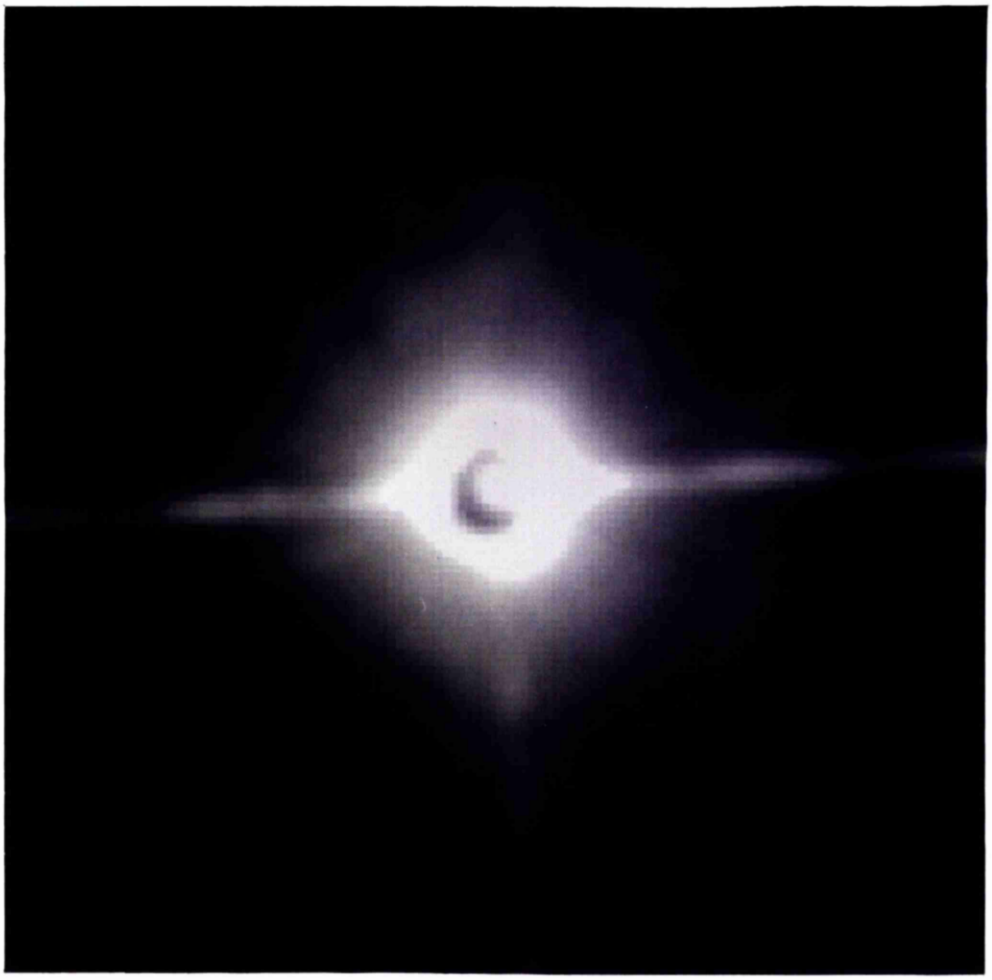

4.3 Discussion

4.3.1 Instrumental performance

Images of the nebulosity around the bright (V = 4.8 mag) star P Cygni have been obtained over a uniquely wide field with MOMI. Better resolution of the small–scale features in the inner and outer nebular shells of P Cygni has been obtained than previously. Furthermore, a faint, extensive nebular arc has been discovered apparently projecting from these two shells. These observations were made possible by the effectiveness of the chromium occulting mask at limiting the amount of light, from the intense central star, which is transmitted through the refracting optics. Consequently 'ghosting' of transmitted starlight from the refractive elements has been reduced to a level that is undetectable in the final image over the whole field.

The present version of MOMI has been designed to be transportable between several telescopes with Cassegrain focal ratios greater than 10 and it has not been optimised for one in particular. Within this limitation, MOMI has performed to design expectations, producing excellent imagery (0.9″ FWHM in 0.7″ seeing) to a field radius of ≈ 4 arcmin. Off–axis optical aberrations in the corners of the field broaden the stellar profiles to ≈ 1.2″. The Tessar collimator is operating beyond its design limit at the these extreme field angles in a square field and at f/10.

Secondary 'ghosts' of the brightest parts of the nebulosity which originate within the multi–layers of the interference filter (see Fig. 4.2) place restrictions

on the filters that can be used with this system. All multi–layer, narrow–band interference filters suffer from minor defects in their construction. With careful selection of filters, and with tilt tuning of the passband position, the filter 'ghosts' can be minimised and placed away from areas of interest. The filter 'ghosts' can be removed by the subtraction of an image of the same object with the filter tilted by the same amount but in the opposite direction. However, for such a procedure to be successful, when MOMI is combined with an altazimuthly mounted telescope such as the NOT, would also require careful alignment of the diffraction spikes during observations and was not attempted here.

The processing of data acquired with an equatorially mounted telescope is far simpler than that obtained with the altazimuthly mounted NOT. The spikes could be reduced with the use of a fixed apodising mask in the pupil near the interference filter (see Fig. 2.1) which is technically more complex to achieve when altazimuth field rotation is involved.

The present version of MOMI also permits the use of a gas pressure stepped Fabry–Perot interferometer in the pupil of the 'science' arm. When this option is commissioned complete image/velocity data 'cubes' will be obtainable around bright sources.

4.3.2 P Cygni phenomena

The most striking feature of these initial observations of the environment of P Cygni is the ≥ 5 arcmin long faint nebular arc shown in Fig. 4.1. This exten-

sive arc appears to be associated with P Cygni and not simply foreground or background nebulosity: it originates at the northern edge of the outer nebular shell and has a clear connecting filament (see Fig. 4.2) to the latter: there is a hint of a complementary southern arc, extending nearly west to east from P Cygni. The two arcs could then be the edges of a mono-polar lobe projecting from P Cygni. Obviously, the presence of this southern arc needs confirming with much deeper imagery and a corresponding western lobe searched for.

With a distance to P Cygni of 1.8 kpc (Lamers, De Groot & Cassatella 1983b) then, if the arc (or lobe) is nearly in the plane of the sky its linear extent is $\geq$ 2.6 pc from P Cygni. It is then comparable in dimensions to the extraordinary, faint lobes projecting from the planetary nebula KjPn 8 (Lopez, Vazquez & Rodriguez 1995). The large angular extent of the giant lobe suggests that its origin predates both the 880 yr. age (Barlow et al. 1994) of the inner shell in Fig. 4.3 and the 2100 yr. age (Meaburn et al. 1996a) of the outer shell in Fig. 4.2, and, indeed, (Meaburn, López & O'Connor 1999) find that the lobe is of the order of 20,000 yrs old. This places its time of ejection prior to the LBV phase which is thought to last only 10,000 yrs.

It is interesting to note that the optical arc/lobe shown in Fig. 4.1 appears to have a radio counterpart in the maps of Baars & Wendker (1987) and Skinner et al. (1998). As a thermal origin for the radio emission is indicated, radiative ionization of this extensive feature seems likely.

Barlow et al. (1994) explained the difference in velocities observed in the inner shell in the light of [N II] λ6584 Å and [Ni II] λ7378 Å as being due to the

emission originating in different locations within the shell. They suggested that the [N II] λ6584 Å emission was primarily observed from gas stripped from clumps by the 206 km s^{-1} wind from P Cygni. They also suggested that the [Ni II] λ7378 Å emission, with its lower ionisation potential, originates in the clumps. For this model to be supported by the morphological observations presented here the [Ni II] λ7378 Å image would be expected to appear far 'clumpier' than the [N II] λ6584 Å image. Indeed, it would be expected that the [N II] λ6584 Å emission would be from areas around clumps in the [Ni II] λ7378 Å image. The new [Ni II] λ7378 Å image does reveal the structure of the IS to be clumpier than the [N II] λ6584 Å image. The [N II] λ6584 Å image of the IS, however, appears to have a loopy structure, not confined to regions around clumps in the [Ni II] λ7378 Å image. One interpretation of this structure would be that it is formed from the superposition of many bubbles. It is quite clear that the IS should not be considered as a simple spherical shell.

4.3.3 Broader use of MOMI

The possible ionized environments close to a large number of bright ionizing stars other than LBVs (e.g. symbiotics, O & B stars etc.) can be investigated with MOMI in its present form.

However, chromium deposited occulting masks can easily be manufactured to prescribed patterns, consequently, MOMI can be used beneficially on a broad range of problems where central sources, of any shape, are extremely

bright compared with the adjacent line emission phenomena; e.g. where faint [O III] 5007 Å emitting halos of PNe surround dominantly bright and compact (say 20″ diam.), similarly [O III] 5007 Å emitting, cores. These PNe cores can be occulted with customised masks. The imagery of the Laques and Vidal knots (Laques & Vidal 1979) close to the Trapezium group of stars would also benefit if all images of the bright stars in the same field were occulted simultaneously.

Chapter 5

Kinematical observations of the planetary nebula IC 4593

5.1 Introduction

The striking planetary nebula (PN) IC 4593 has attracted much observational and theoretical interest in recent years. It consists of a complex system of shells and condensations that extend to in excess of 1′ from the variable central star (Mendez, Herrero & Manchado 1990). The principal features (beginning from the central star and moving outwards) are as follows and are depicted in Figs. 5.1(a) & 5.2 .

The bright core is an asymmetrical, 10″ diameter, shell within which there is a high density 'rim' (Zucker & Soker 1993, Corradi et al. 1997 - henceforth CGMM) and a highly asymmetrical system of [N II] λ6584 Å bright knots superposed on fainter irregular emission. CGMM measured the expansion

velocity of the core as $\approx$ 15 km s^{-1}.

Protruding from this bright core, into the 'inner halo', are what appear to be opposing, collimated outflows culminating, at $\approx 12''$ from the central star, in lowly ionized bright knots (X and Y in Figs. 5.1(a) & 5.2, A & B in CGMM). These knots share many characteristics of the low ionization features described by Lopez, Roth & Tapia (1993) and Balick et al. (1993; 1994). These structures are often found as diametrically opposite pairs with the same, high, outflow speeds. CGMM obtained excellent imagery and high-resolution spectrometry of the core and inner halo. They demonstrated that the lowly ionized knots X and Y had radial velocities of -5 km s^{-1} and 0 km s^{-1} respectively with respect to the systemic heliocentric radial velocity $V_{\rm sys}= 21 \pm 3$ km s^{-1} .

The inner halo is bounded by a shell that is strongly brightened to the north-west forming an intriguing arc-like feature (Fig. 5.2). This arc has a noticeable bulge (e.g. Zucker & Soker 1993).

Finally, within the south-west segment of the faint, clumpy outer halo there are irregular strings of lowly ionized emission line knots. The outer halo is irregular and may be described as elliptical; CGMM measured its extent to be $\approx 130'' \times 120''$ from a deep Hα & [N II] λ6584 Å image. It is not centred on the inner shell. To date there has been no kinematical information presented on the outer halo knots.

As with most PNe, the distance to IC 4593 is not well known. Estimations range from d = 1.5 kpc (Amnuel et al. 1984) to d = 4.3 kpc (Cudworth 1974). This range of values combined with galactic latitude b = 41° places

IC 4593 significantly above the galactic plane.

Efforts to model this PN have mainly focussed on the arc feature of the inner halo (see Fig. 5.2), which has been the subject of some recent controversy. Zucker & Soker (1993) presented a model in which the highly supersonic movement of the planetary nebula with respect to the interstellar medium causes the interstellar medium to stream into the body of the nebula and generate a bow-shock structure around the central regions. Bohigas & Olguin (1996) raised objections to the Zucker & Soker (1993) model, many of which were addressed by Dgani & Soker (1998). The reader is referred to these papers, and to Soker (1998a), for details of the discussion. An important problem that has not been resolved is that at the height above the galactic plane of IC 4593 (at least 1 kpc) the density of the interstellar medium may be too low to dominate the dynamics of the nebula even at the high relative velocity of IC 4593 (estimated to be $\gtrsim 100$ $\mathrm{km\,s^{-1}}$ by these authors).

The origin of the condensations in the outer halo of IC 4593 is also not yet clear. Zucker & Soker (1993) suggest that the condensations are formed from a thermal instability in the halo by an oscillating bow shock interaction between the nebula and the ISM. Alternatively, Bohigas & Olguin (1996) find several arguments for an origin in the kinematic interaction between mass lost from the central star and the ISM.

In this chapter a kinematical study of the various features of this PN is carried out based on observations obtained with the Manchester echelle spectrometer (MES - Meaburn et al. 1984) combined with the San Pedro Mártir 2.12 m

telescope.

5.2 Observations and results

Spatially resolved longslit spectra were obtained with MES for the EW slit positions A–H, marked in Figs. 5.1(a) & 5.1(b), over the nights 1995 April 6-7, 1996 April 14-15 and 1997 March 12-13. For these observations MES was combined with the $f/7.5$ Cassegrain focus of the 2.1m San Pedro Mártir telescope with a Tektronix 1024 × 1024 24 μm CCD as the detector. For the Hα and [N II] $\lambda\lambda$6548, 6584 Å lines (for all slit positions) a bandpass-type interference filter isolated the 87th echelle order and for the [O III] 5007 Å line (for slit A only) a similar filter isolated the 114th echelle order. For all observations the slit width was 150 μm ($\equiv$ 10 km s^{-1}) which projects to an angular width of 1″.9 on the sky. The CCD pixels along the length of the slit were each equivalent to 0″.6 on the sky. Integration times were 1200 s for all slit positions except C. For C, over the bright core, only 200 s was required. Seeing varied between 1″ and 2″ throughout the observations. The data were processed at the University of Manchester Starlink node with programs from the CCDPACK, FIGARO, KAPPA and TWODSPEC packages in the usual manner.

5.2.1 The bright core

The position–velocity (pv) arrays of Hα and [N II] λ6584 Å line profiles from the bright nebular core, crossed by slit C, are shown in Figs. 5.3 (a) & (b)

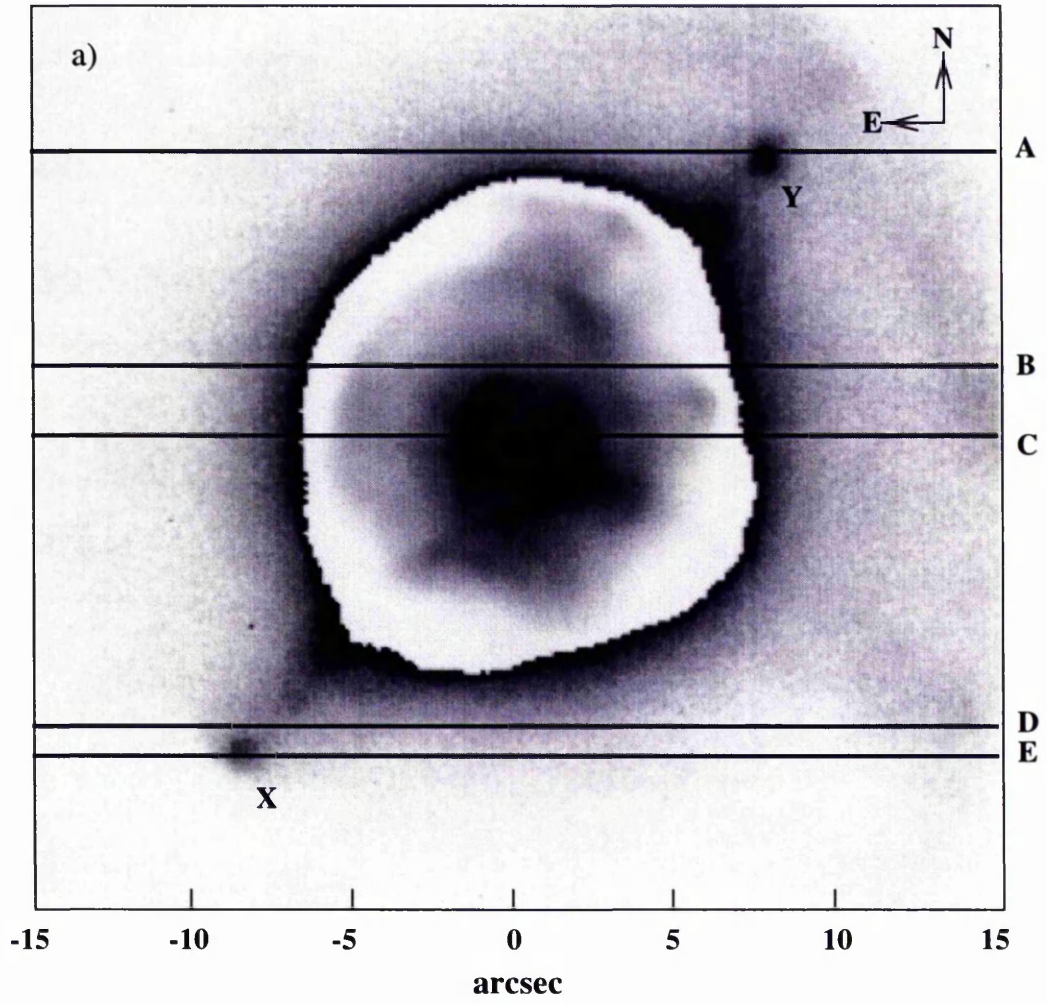

Figure 5.1: **a.** [N II] λ6584 Å image of the bright core and features in the inner halo from Manchado et al (1996). The positions of the slits A–E are marked as are the knots X & Y.

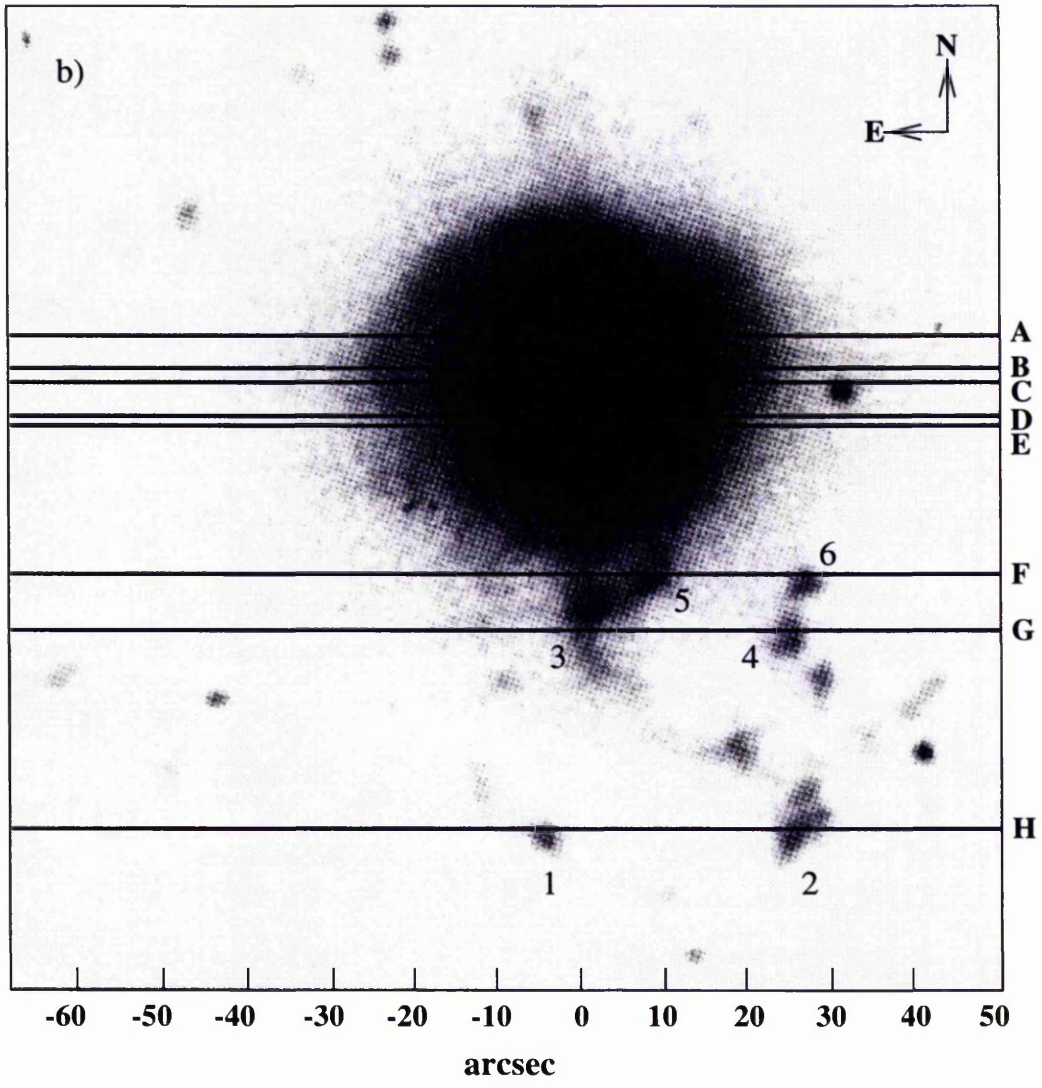

Figure 5.1: **b.** Longslit positions (A–H) for all of the spectral observations are indicated on an Hα image, from Zucker & Soker (1993). The halo knots discussed in the text are labelled (1–6).

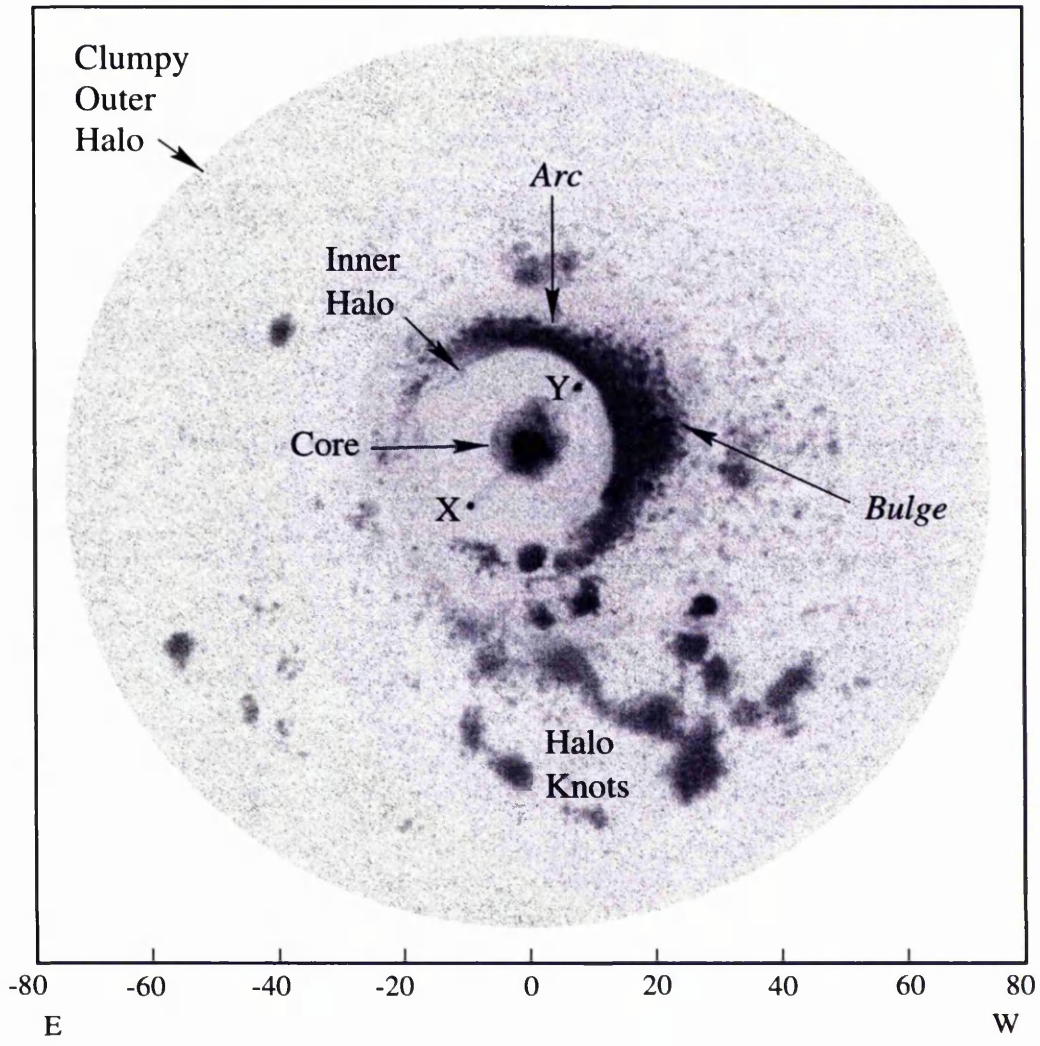

Figure 5.2: A sketch of IC 4593 with the main features that are discussed here indicated. Note that the circular shaded area only indicates the maximum radial extent from the central star at which the halo has been detected, see fig. 2 of CGMM for an excellent deep image of the halo.

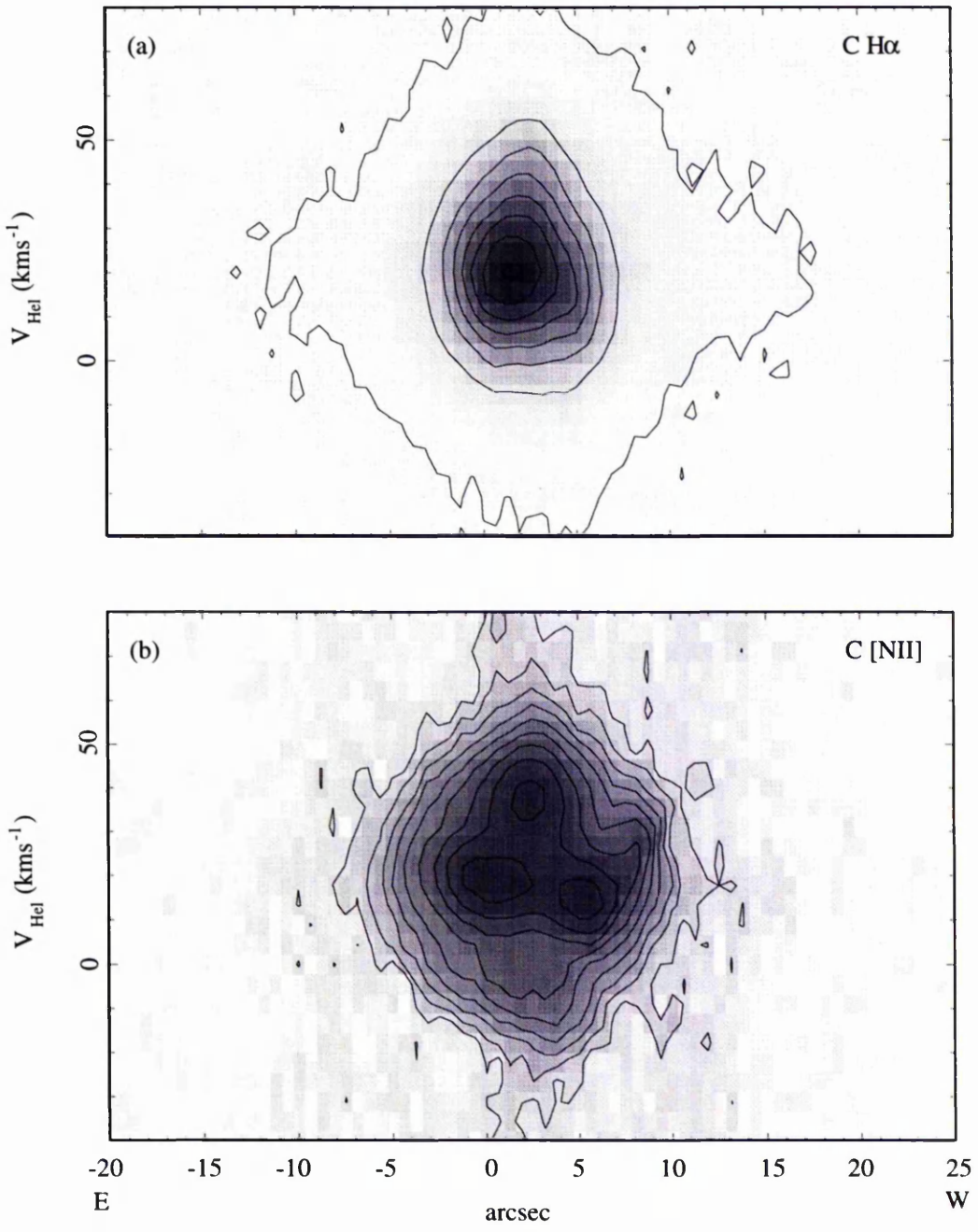

Figure 5.3: Negative, greyscale representations of the pv arrays over the core for slit position C, (a) in the light of Hα shown with linear contours equally spaced between 10 and 3500 and (b) in the light of [N II] λ6584 Å with contours rescaled to $\log_{10}$ and evenly spaced between 1.2 and 3.1.

respectively. Most noticeable are the distinct velocity features which appear in the [N II] λ6584 Å array (Fig. 5.3b) but are absent at Hα (Fig. 5.3a); the most striking of which is $\sim 2''$ from the central star at $V_{\rm HEL} \approx 40$ km s^{-1}.

5.2.2 Knots X & Y and inner halo

Striking velocity features are shown in Figs. 5.4, 5.5(a) & (b) and 5.6(a) & (b) for slit positions A and E which cross the nearly point symmetric knots X and Y projecting from the bright core into the inner halo (see Figs. 5.1(a) & 5.2). Firstly, the [N II] λ6584 Å profiles in Figs. 5.5(b) and 5.6(b) show that the lowly ionized knots X and Y have radial velocities of $V_{\rm HEL} = 10 \pm 2$ and 24 ± 1 km s^{-1} respectively (near $V_{\rm sys} = 21 \pm 3$ km s^{-1} given by CGMM). However, a $10''$ wide velocity feature has been discovered which extends from $V_{\rm sys}$ in the [O III] 5007 Å and Hα profiles out to $V_{\rm HEL} = 140$ km s^{-1} (Figs. 5.4 & 5.5(a)) for slit position A; and in the Hα profiles to −75 km s^{-1} for slit position E (Fig. 5.6(a)). These remarkable velocity features, which project above and below the core, are from the slit lengths between $\approx \pm 5''$ (with respect to the somewhat arbitrary zero shown in Figs. 5.4, 5.5, and 5.6.) and do not correspond spatially with the knots X and Y.

5.2.3 The outer halo knots

Kinematics

Heliocentric radial velocities for the bulk motions of the halo knots are found from the pv arrays for slits F, G and H and summarised in Table 5.1.

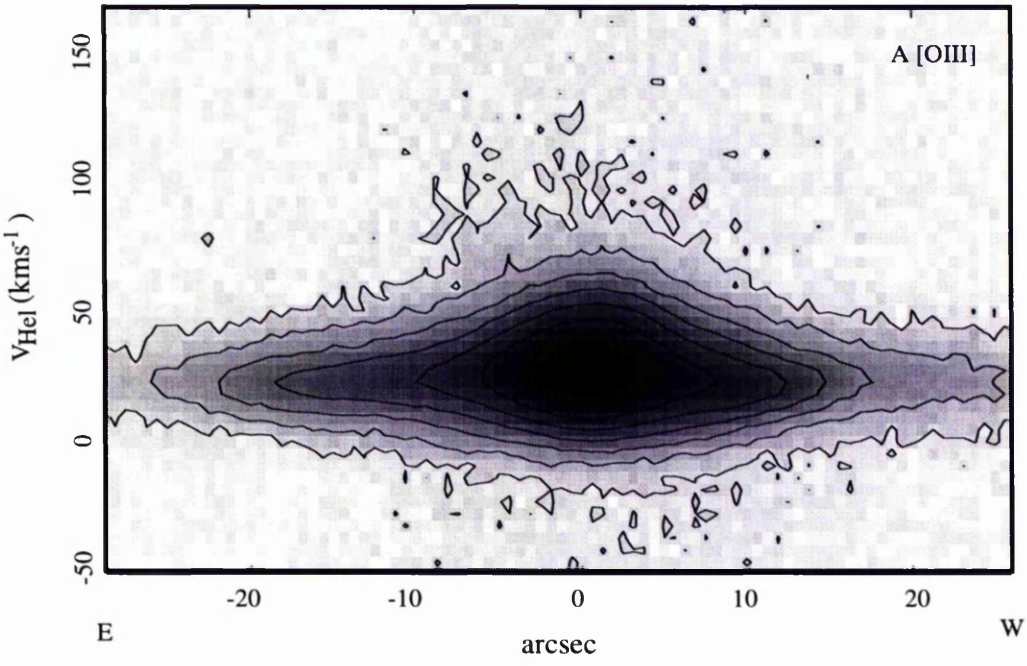

Figure 5.4: A negative, greyscale representation of the pv array of [O III] 5007 Å profiles for slit position A is shown. Also apparent is the projection to positive velocities from the inner halo. The superimposed contours are rescaled to $\log_{10}$ and equally spaced between 1.5 and 4.8.

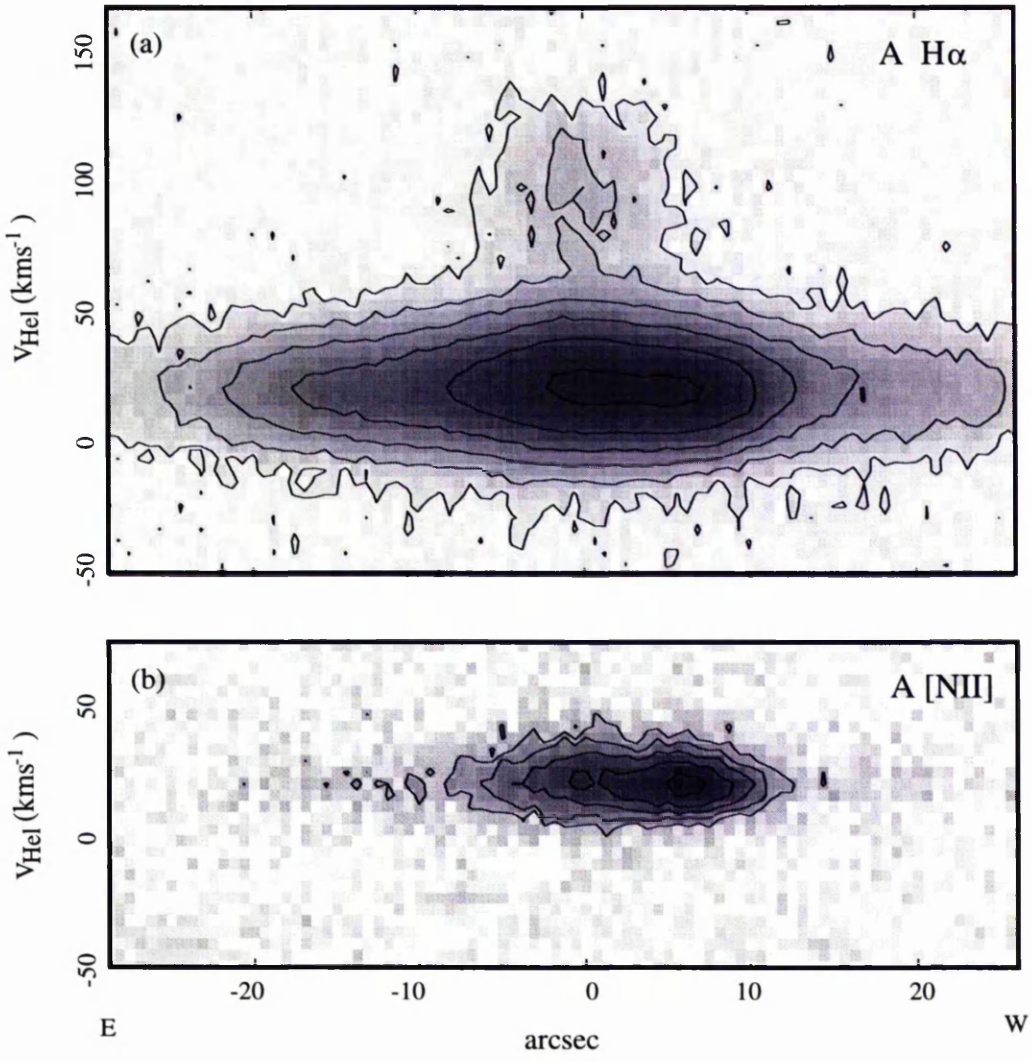

Figure 5.5: (a) A negative, greyscale representation of the pv array of Hα profiles for slit position A with $\log_{10}$ contours equally spaced between 1.35 and 3.2. (b) As for (a) but in the light of [N II] λ6584 Å with contours evenly spaced between 1.5 and 2.3.

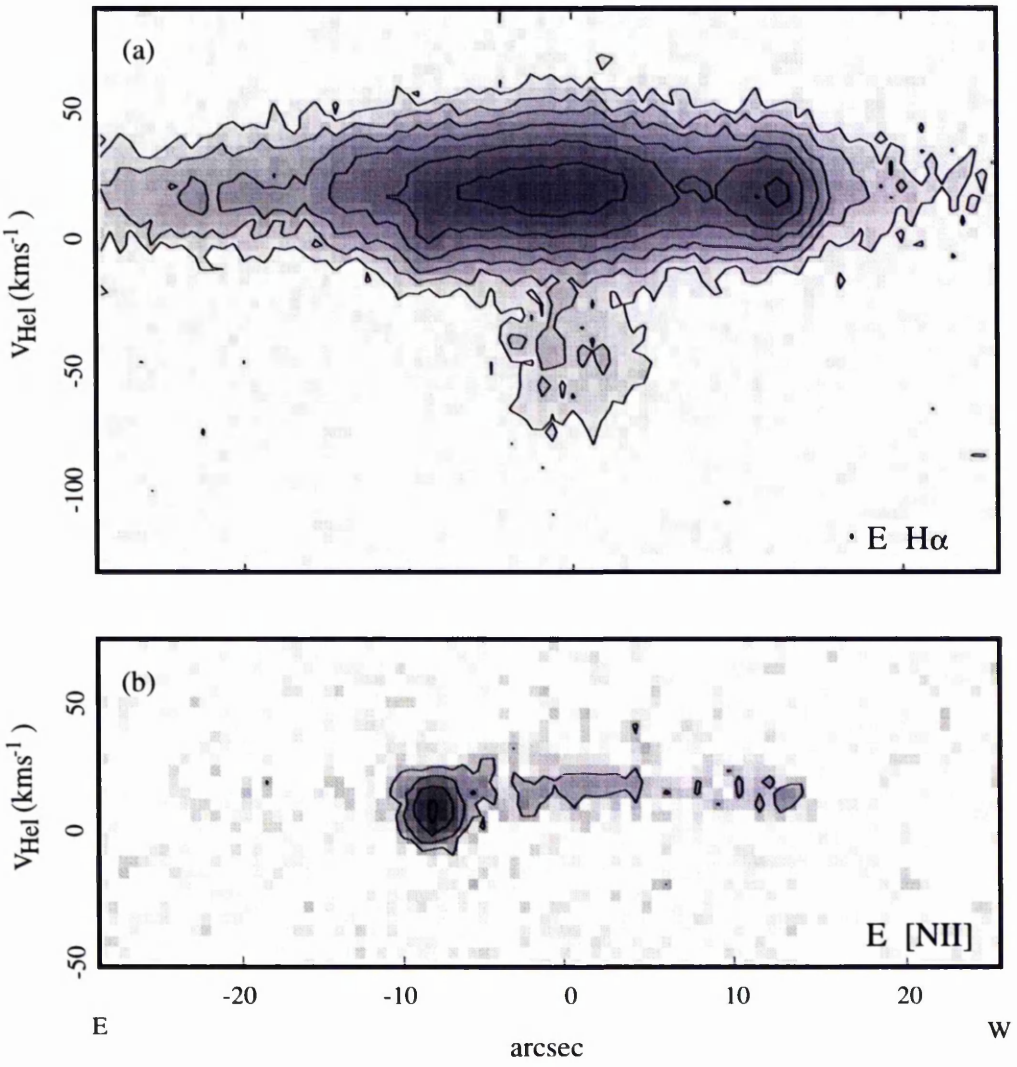

Figure 5.6: As for Fig. 5.5 but for slit position E. (a) $\log_{10}$ Hα contours equally spaced between 1.05 and 2.4. (b) $\log_{10}$ [N II] λ6584 Å contours evenly spaced between 1.1 and 1.9.

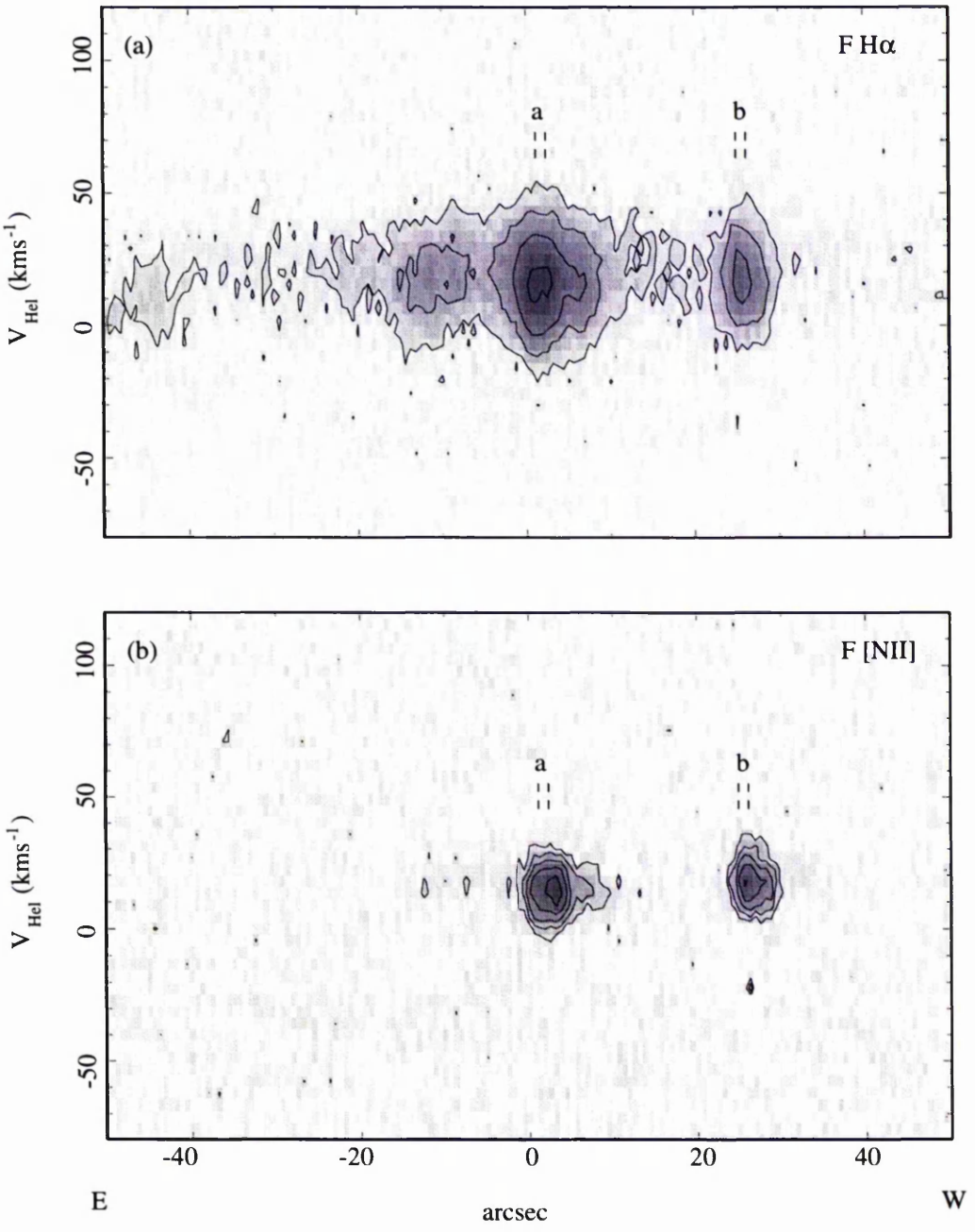

Figure 5.7: (a) A negative greyscale representation of the pv array of Hα profiles for slit position F is shown. Features associated with outer halo knots 5 and 6 (Fig. 5.1(b) are apparent. The $\log_{10}$ contours are spaced evenly between 1.3 and 2.5. (b) As for (a) but for [N II] λ6584 Å profiles with ($\log_{10}$) contours between 1.25 and 2.1. The turbulences and electron temperatures measured from profiles extracted between the incremental lengths marked a and b are summarised in Table. 1.

Knot	1	2	3	4	5	6
$V_{\rm HEL}$(km s^{-1})	26	25	22	23	16	18
	$\pm$ 3	3	3	3	2	2
$T_{\rm e}(\times 10^3{\rm K})$	–	9	–	14	12	9
	–	$\pm$ 4	–	6	1	1
$\delta V_{\rm Tu}$ (km s^{-1})	–	17	–	9	10	9
	–	$\pm$7	–	4	1	1

Table 5.1: Summary of derived values for $V_{\rm HEL}$, $T_{\rm e}$ and $\delta V_{\rm Tu[H\alpha]}$, the half–width of the turbulent component (Eq. 5.1), for the halo knots labelled 1–6 in Fig. 5.1 along with their uncertainties. Where no value is given low signal to noise in the [N II] λ6584 Å spectra made the results unreliable. (Note $V_{\rm sys} \approx 21$ km s^{-1}).

Negative, greyscale representations of the pv arrays of Hα and [N II] λ6584 Å for slit position F, which covers knots 5 and 6 (Fig. 5.1(b)) in the outer halo, are shown in Figs. 5.7(a) & (b) respectively.

Turbulence and $T_{\rm e}$ of the knots

Similar to the halo knots of NGC 40 (Meaburn et al 1996), a simple inspection of the pv arrays in Figs. 5.7(a–b) (sample line profiles are shown in Fig. 5.8) reveals that the strings of knots in the outer halo (1–6 in Fig. 5.1) have very low internal turbulent motions and are bright in the [N II] λ6584 Å emission line. This combination permits a reliable electron temperature to be derived from a comparison of the Hα and [N II] λ6584 Å profile half-widths (see Appendix A).

The observed profile of a single emission line of halfwidth $\delta\lambda$ is a convolution of several profiles (Courtes, Louise & Monnet 1968) given by

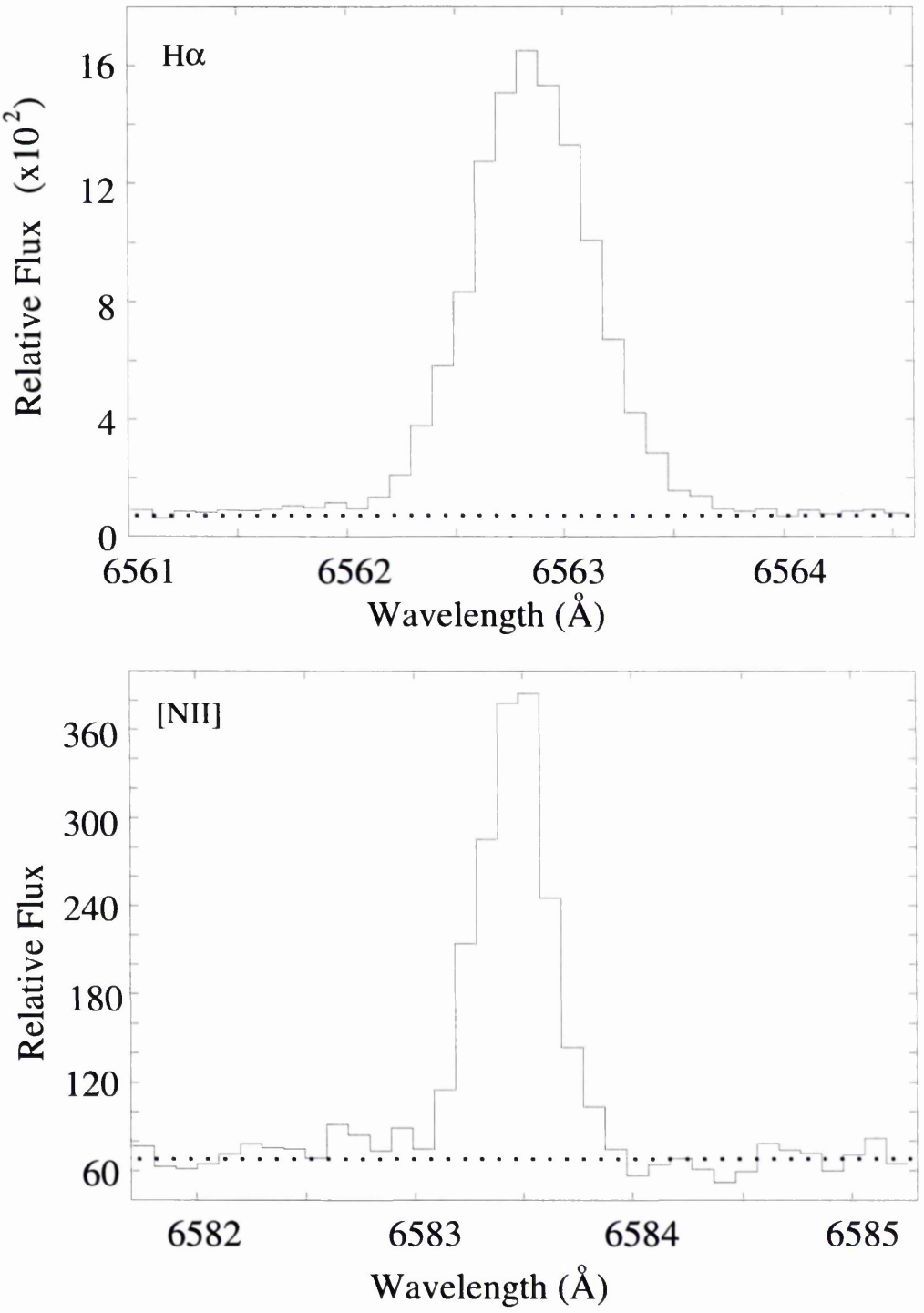

Figure 5.8: [N II] λ6584 Å and Hα line profiles from the pv array for slit F (from position a in Figs. 5.7(a) & (b)) from an outer halo knot to which Gaussians were fitted to derive an electron temperature.

$$\delta\lambda^2 = \delta\lambda_{\rm I}^2 + \delta\lambda_{\rm Tu}^2 + \delta\lambda_{\rm Th}^2 \ , \tag{5.1}$$

where $\delta\lambda_{\rm I}$ is the halfwidth of the instrumental profile, $\delta\lambda_{\rm Tu}$ is the halfwidth of the profile produced by turbulence in the emitting region and $\delta\lambda_{\rm Th}$ is the halfwidth associated with thermal broadening. For Hα a fine structural splitting component should also be considered (Meaburn 1970).

In regions where the turbulent motions are similar and assuming the instrumental broadening is the same for Hα and [N II] λ6584 Å and as

$$\delta\lambda_{\rm Th[H\alpha]} = \sqrt{14}\ \delta\lambda_{\rm Th[NII]}, \tag{5.2}$$

then

$$\delta\lambda^2_{\rm [H\alpha]} - \delta\lambda^2_{\rm [NII]} = \frac{52\ln 2\ \lambda_{\rm o}^2 k T_{\rm e}}{7c^2 m_{\rm p}} \ , \tag{5.3}$$

where $c, T_{\rm e}, k$ and $m_{\rm p}$ have their usual meaning and $\lambda_{\rm o}$ is the rest wavelength of Hα.

The Hα line has seven fine structure lines. Meaburn (1970) and Dyson & Meaburn (1971) showed that the seven lines can be modeled as the sum of two equal Gaussian components separated by 0.14 Å and that the half–width of the Gaussian components is a better estimate to the single line profile. A first order approximation, sufficient for the observations presented here, is

$$\begin{aligned} T_{\rm e} &= 49176(\delta\lambda^2_{\rm obs[H\alpha]} - \delta\lambda^2_{\rm obs[NII]} - 2\ln 2\ x_{\rm s}^2)\ K \ , \\ &= 49176(\delta\lambda^2_{\rm obs[H\alpha]} - \delta\lambda^2_{\rm obs[NII]}) - 1336\ K \ , \end{aligned} \tag{5.4}$$

where x_s is the separation of the two principal fine–structural Gaussians that simulate the Hα line.

After derivation of T_e an accurate estimation can then be made of the internal turbulent motions in the [N II] λ6584 Å emitting volume of a knot.

Gaussian fits were made to the observed Hα and [N II] λ6584 Å line profiles from halo knots 1–6 (Fig. 5.1(b)) for slit positions F–H. The FWHM of these fits, after substitution into Eq. 5.4, yielded values for T_e which are listed in Table 5.1.

The internal turbulent motions, $\delta\lambda_{Tu}$, are then found for these values of T_e and are listed in Table 5.1.

5.3 Discussion

5.3.1 Knots X & Y

The heliocentric radial velocity, near V_{sys} (see Fig. 5.5(b)), found for knot Y is in excellent agreement with the value given by CGMM. That found for knot X is somewhat less than the value given by these authors and also close to V_{sys}. Although both knots are close to V_{sys} they could still be nearly diametrically opposed high-speed ejecta, as suggested by their appearance in Fig. 5.1, with motions nearly in the plane of the sky. To project a radial velocity difference of 14 km s^{-1} knot X would need to be moving at an angle of $\sim 8°$, for an assumed speed of 100 km s^{-1}, away from the plane of the sky. It is interesting to note that knots X & Y appear to be embedded within a collimated flow originating

in the core (CGMM; a similar phenomenon is also seen in NGC 7009, Balick et al. 1998).

5.3.2 Velocity spikes

More difficult to explain are the spatially extended, 'velocity spikes' ($\pm$ 100 km s^{-1} with respect to $V_{\rm sys}$) in the Hα and [O III] 5007 Å profiles shown in Figs. 5.4, 5.5(a) & 5.6(a). These could be simple manifestations of diametrically opposed, diffuse ejecta from the core of IC 4593, in which case they are radiatively ionized, line emitting regions. The possibility that their Hα and [O III] 5007 Å line profiles are the consequence of the bright core line emission being scattered by out-flowing dusty gas is unlikely since the scattered light is expected to be red-shifted from both outflows (as has been observed for M2–9 by Schwarz et al 1997 and for NGC 2440 by López et al 1998) unless the light emitter has an expansion speed greater than the out-flowing dust which is not observed in IC 4593. Spectropolarimetric observations of these extended velocity components could clarify their origin. If the profiles are scattered to some extent by dust flows then they should be polarised by up to 30 percent. The present kinematical observations may contradict the Zucker & Soker (1993) interpretation. While these high velocity features may be as a result of the flow-through of interstellar matter at velocities of $\sim$ 100 km s^{-1} into the inner regions of the planetary nebula there should be many more easily discernible velocity features. In particular, the outer, less dense regions of the nebula should be more dramatically affected than the inner regions. In fact

the present results show that the outer halo and its knots are almost puzzlingly quiescent, given the complex morphological structure of the nebula.

5.3.3 The outer halo knots

The outer halo knots are shown here to have bulk motions very near to $V_{\rm sys}$, low turbulent motions in their Hα emitting volumes and [N II] λ6584 Å line emission prominent (i.e. lowly ionized). In fact, they have identical characteristics to their counterparts in the PN NGC 40 (Meaburn et al 1996). A similar interpretation is therefore invited. They appear to be radiatively ionized surfaces around dense condensations in the relatively inert circumstellar medium that preceded the formation of this PN. Of course, as proposed for knots X & Y in Sect. 3.1, any bulk motions of the outer shell of knots could be in the plane of the sky and therefore not cause significant Doppler shifts in the line profiles.

Chapter 6

The Engraved Hourglass planetary nebula, MyCn 18

6.1 Introduction

MyCn 18 (Bryce et al. 1997) is a representative of the extreme of the planetary nebulae (PNe) phenomenon for, amongst other curiosities, it exhibits hypersonic bipolar outflows of ionized gas. Similar high–speed characteristics are found in objects such as He 2-111 (Meaburn & Walsh 1989), He 3-1475 (Bobrowsky et al. 1995) and KjPn 8 (Lopez, Vazquez & Rodriguez 1995; Lopez et al. 1997).

MyCn 18 is also aptly known as the 'Engraved Hourglass' nebula due to the visually dramatic bipolar appearance of its bright core (Sahai et al. 1999 and references therein). However, interest in MyCn 18 has recently been further heightened by the discovery of the knots of ionized gas flowing in both direc-

tions along its bipolar axis at speed of $\geq$ 500 km s^{-1} (Bryce et al. 1997). Corradi & Schwarz (1993) had previously investigated the bright core of MyCn 18 and concluded that it is a young PN. The presence of a dusty neutral equatorial waist region, suspected by Sahai et al. (1999) on the basis of an excess in the stellar K-band photospheric flux, substantiated this young age. The radio thermal emission map of Bains & Bryce (1997) reveals the ionized inside surface of the dense waist region to be very bright in comparison to emission from polar directions.

A bi-polar, episodic jet, somewhat artificially rotating about an axis nearly perpendicularly to the plane of the sky, was invoked by López et al. (1993a) to explain the kinematics and morphology of the point symmetric knots in Fleming 1. Cliffe et al. (1995) sought an explanation in precessing jets but in Bryce et al. (1997) a wider range of possibilities to explain the hypersonic MyCn 18 knots were suggested. These models started with a simplistic bipolar, rotating jet interpretation (again rotating perpendicularly to the plane of the sky) but went on to consider wandering bipolar jets or 'grapeshot' outbursts. The limited observations of MyCn 18 at the time hindered the distinction between these possibilities.

In this chapter a complete spatio-kinematical mapping of the high-speed knots within MyCn 18 as well as the bright Hourglass nebular core is reported. In addition, a continuum subtracted image in the light of the Hα and [N II] $\lambda\lambda$6548, 6584 Å emission lines is presented to reveal the full extent of the knots.

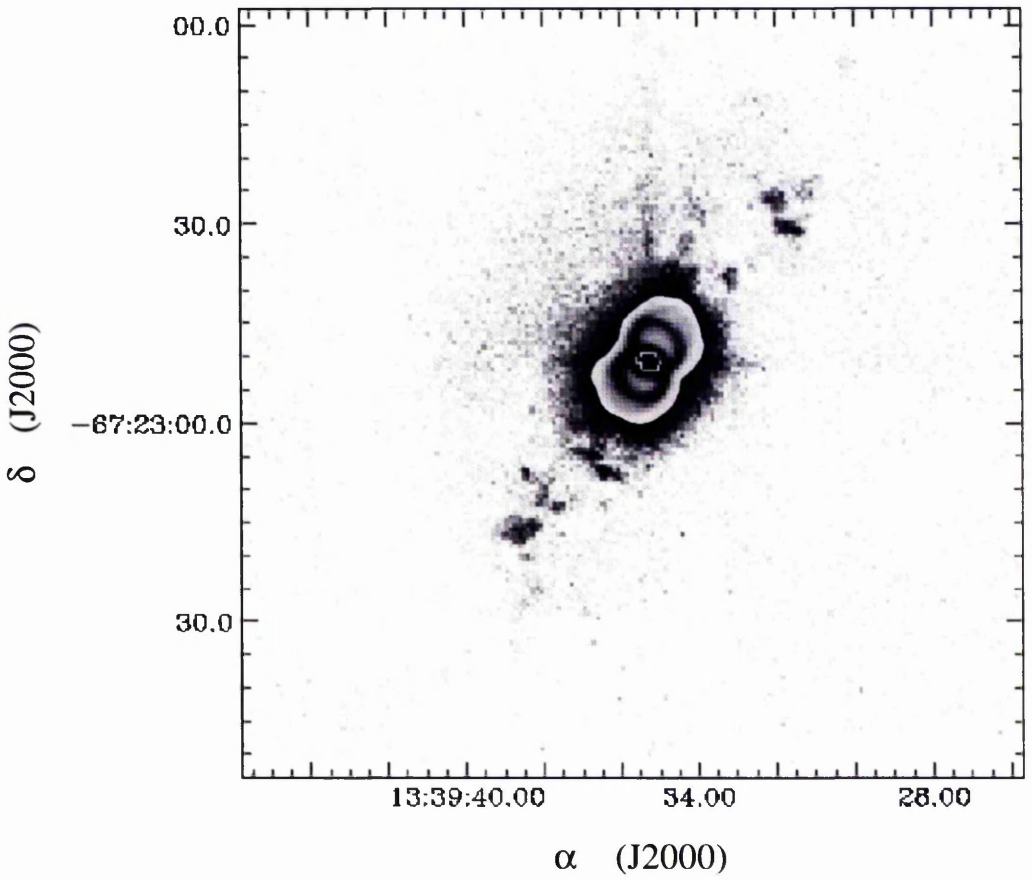

Figure 6.1: The continuum subtracted image of MyCn 18 reveals the elongated, bipolar system of high-speed knots in the light of the Hα and [N II] $\lambda\lambda$6548, 6584 Å nebular emission lines. From O'Connor et al. (2000).

6.2 Observations and results

Spatially resolved, longslit echelle spectra and Hα and [N II] $\lambda\lambda$6548, 6584 Å emission line images of MyCn 18 have been obtained with the Manchester echelle spectrometer (MES; Meaburn et al. 1984) combined with the f/7.9 Cassegrain focus of the Anglo–Australian telescope (AAT). A Tektronix CCD with 1024×1024 24 μm square pixels was the detector. All observations were made between 26–28 March, 1999 using a 100 Å wide interference filter to

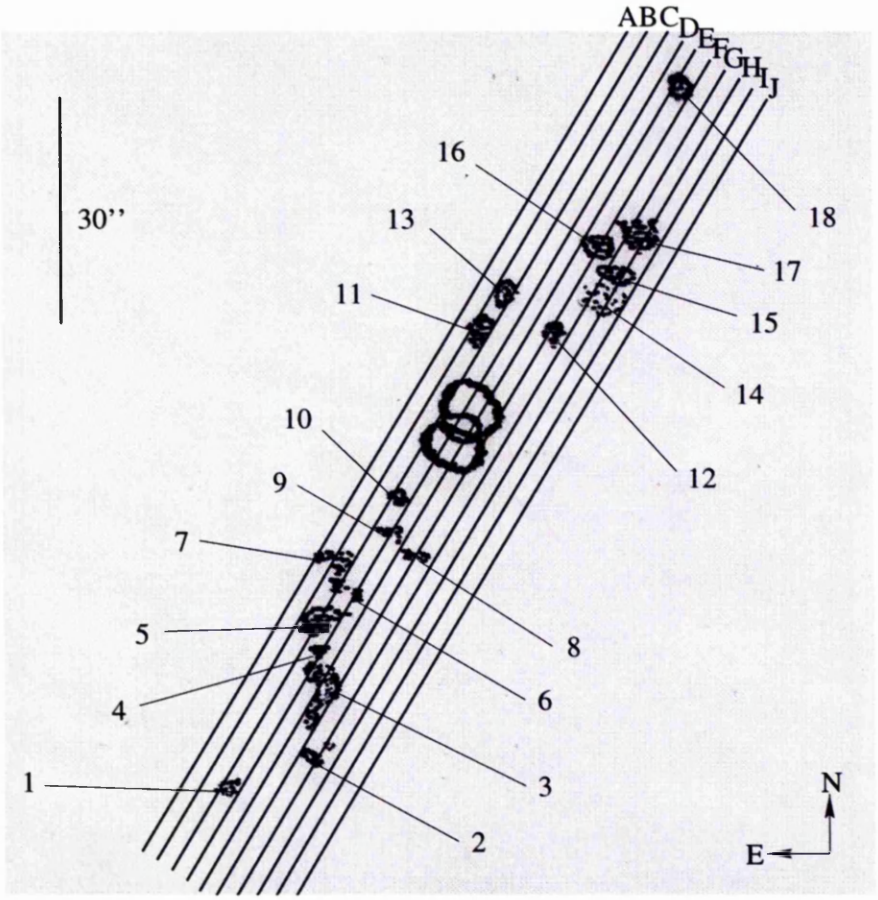

Figure 6.2: Sketch of the main features in the nebula. The slit positions A–J are shown against a sketch of the core and high-speed bipolar knots. The slit lengths correspond to the extents of the pv arrays of line profiles presented in Fig. 6.4.

isolate the 87th order containing the Hα and [N II] $\lambda\lambda$6548, 6584 Å emission lines. A slit width of 150 μm ($\equiv$ 10 km s^{-1} and 1″) was used throughout. The CCD was binned by a factor of two in the spatial direction to give a projected slit length of 512 $\times$ 0″.32.

MES was first used in its imaging mode to obtain continuum subtracted Hα and [N II] $\lambda\lambda$6548, 6584 Å emission line images of MyCn 18. Here integrations were obtained through the aforementioned 100 Å bandwidth filter centred on the lines followed by integrations with a different filter centred on 6690 Å to allow for continuum subtraction. Seeing varied between 1″ and 2″. These images were debiased, aligned and combined using a median filter in the usual way. The removal of stars from the emission line image was carried out by subtracting the continuum image. Due to varying seeing between exposures the subtraction was not perfect and hence the residuals have been patched out using the GAIA patch tool. The final image, re-binned to 0.64"/pixel, (Fig. 6.1) reveals that the faint, outer, high-speed knots are confined to within 10″ of the bipolar axis of the central nebula (along PA = 150°). The radial distance of the furthest knot detected from the central star is 54″.

The longslit spectra were obtained from 11 parallel slit positions (labelled A–J in Fig 6.2) equally spaced by 2″ (in the EW direction) and oriented at P.A. = 150°; details are given in Table 6.1. Each integration was debiased and wavelength calibrated to better than 0.5 km s^{-1} using ThAr spectra obtained between exposures. For slit positions where three integrations had been acquired, the resulting arrays were combined using a median filter to

Slit Position	Integration Time (s)	Seeing (″)	Offset from star (″)
A	3× 1200	1	6
B	3× 1200	1	4
C	3× 1200	1	2
D	2× 1200 & 1× 600	1	0
E	3× 1200	1.5	-2
F	3× 1200	1.5	-4
G	3× 1200	1.5	-6
H	2× 1200	1.5	-8
I	1200	2	-10
J	1200	2	-12

Table 6.1: Details of the integrations obtained for the spectra for slit positions A–J.

increase the signal to noise ratio and remove cosmic rays. Where one or two integrations had been obtained the arrays were cleaned in the usual manner and where possible co-added. Subsections of the resultant pv arrays of line profiles are shown in the greyscale representations in Figs. 6.3 & 6.4.

The pv arrays over the bright nebular core are shown in Figs. 6.3(a-f). These reveal a largely straightforward kinematical structure around a systemic heliocentric radial velocity $V_{\rm sys}$ = -71 km s^{-1}. For instance, the pv array along the central slit positions D & E, contains two distinctly separate velocity features. One, around 0″ offset from $V_{\rm HEL}$ = 0 to -140 km s^{-1} and the other, tilted and from $V_{\rm HEL}$ = -40 to -90 km s^{-1}. An outflowing, bipolar cavity is indicated (see Sect. 4). The latter feature seems to extend faintly from $V_{\rm HEL}$ = 10 to -40 km s^{-1} for offsets between -10 and -16″ and from -90 to -150 km s^{-1} for offsets between 10 and 16″.

The pv arrays of either Hα or [N II] λ6584 Å profiles in Figs. 6.4(a–j) for slit

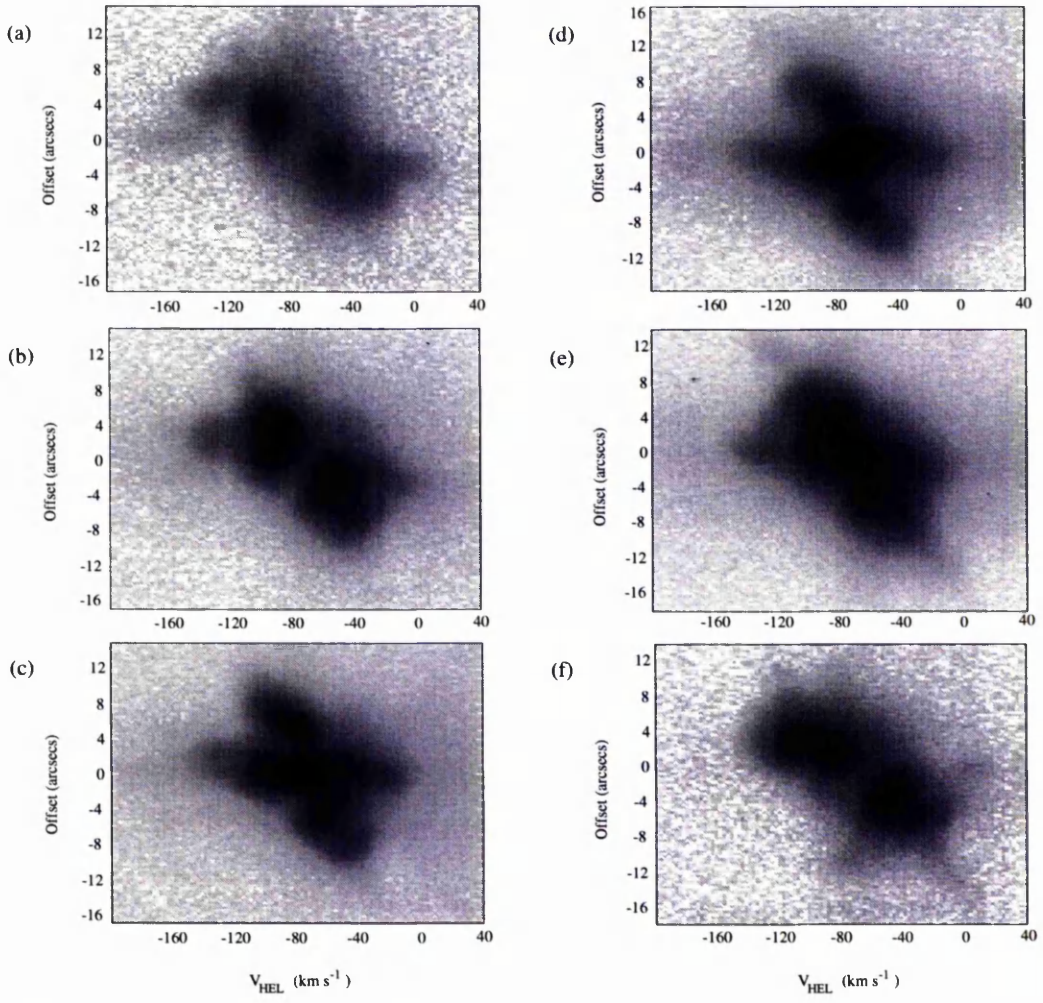

Figure 6.3: Greyscale representations of subsections of the PV arrays for slit positions B–G, displayed with a log scale, which cover the core.

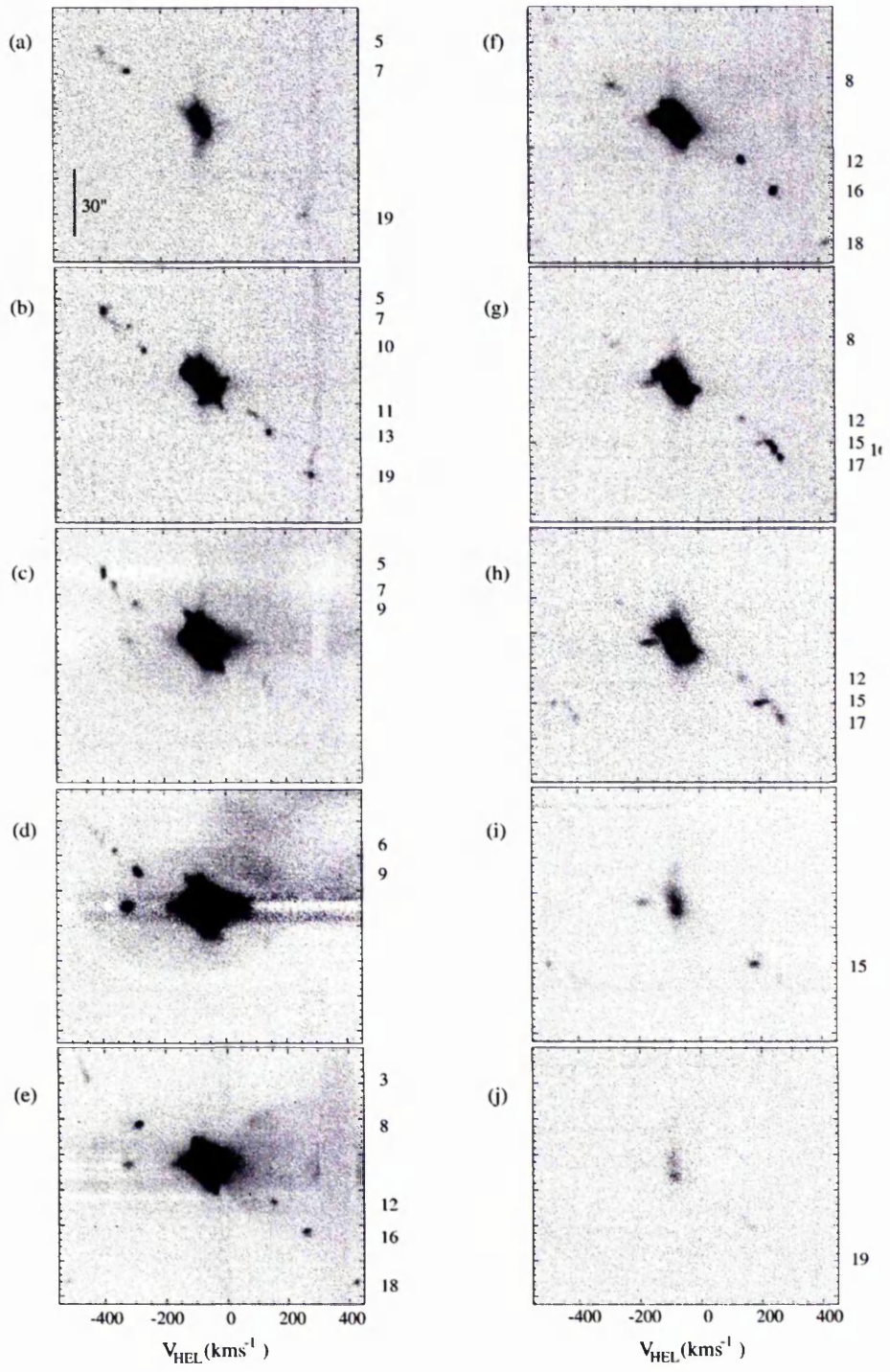

Figure 6.4: Greyscale representations of the PV arrays for slit positions B–K, displayed with a log scale except for positions J & K which are displayed with a linear scale, which cover the knots (labelled 2-19 on the right hand axis).

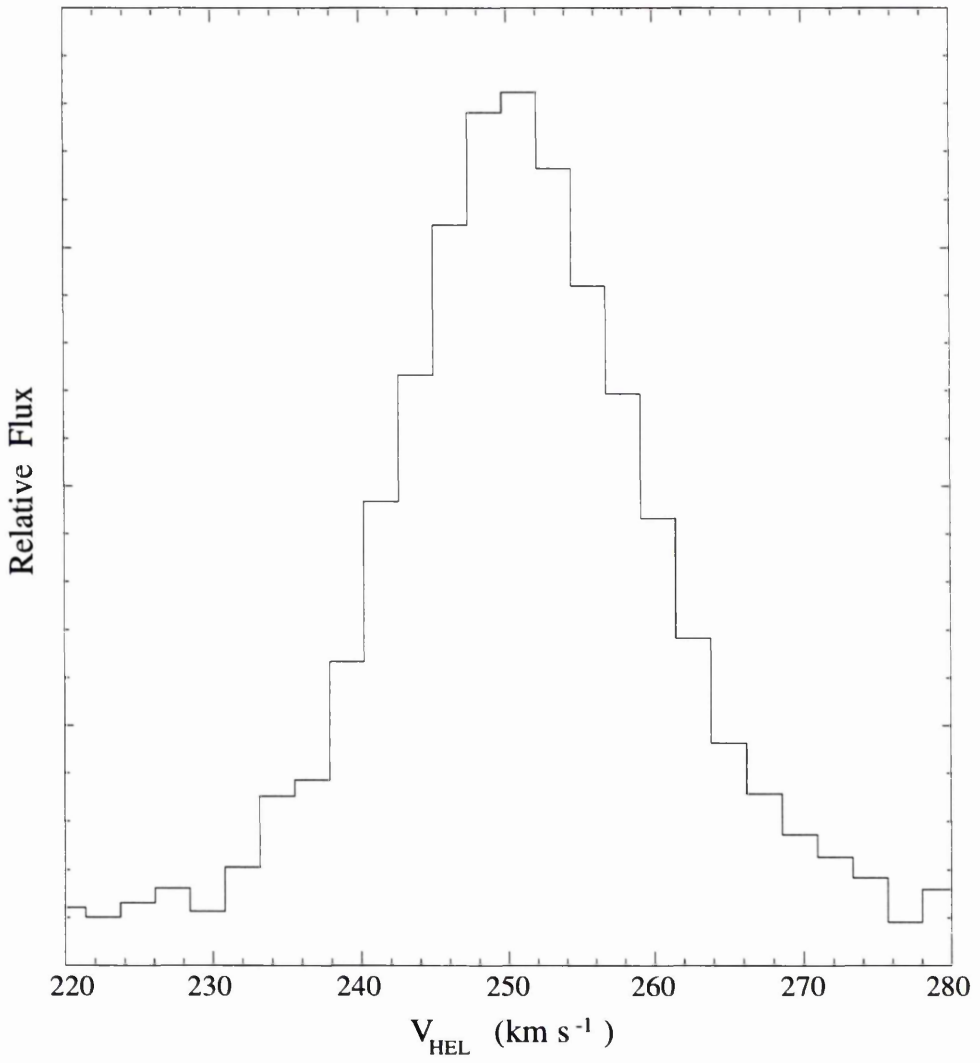

Figure 6.5: The observed profile of the [N II] λ6584 Å line from knot 16 (see Fig. 6.4f)

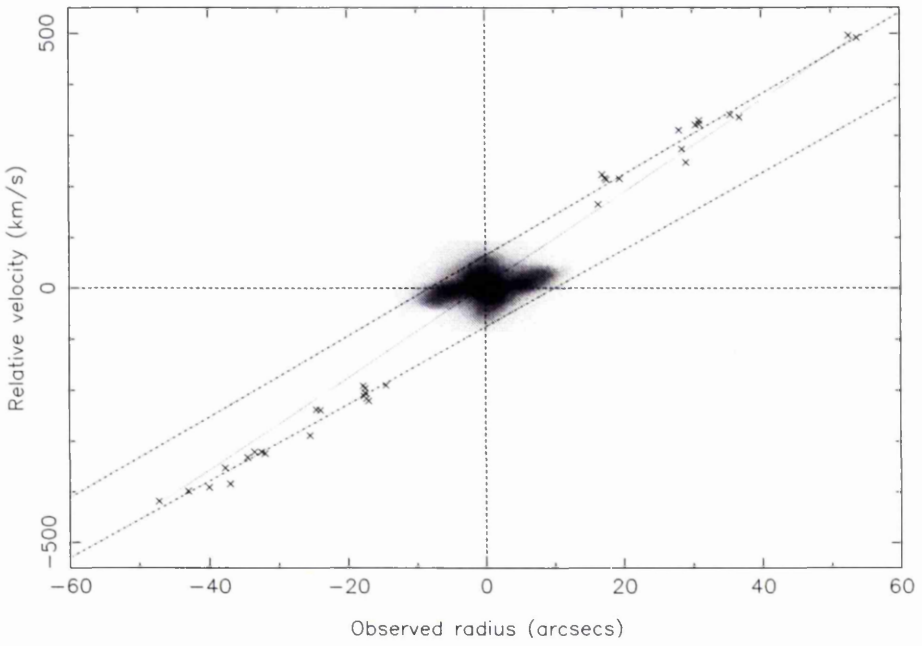

Figure 6.6: The observed radial velocity (relative to V_{sys}) is plotted against the apparent angular radius of each knot from the central star as given in Table 6.2. Superimposed on this plot is a logarithmically scaled greyscale representation of the pv array from the most centrally aligned slit position (D). The dash–dot–dash lines are independent linear fits to the data points on either side of the core. The dotted line is simply drawn between the two most extreme points.

position A–J respectively show the complete kinematical behaviour of the high-speed knots 2-18 marked in Fig. 6.2. Only knot 1 is missing. Values of $V_{\rm HEL}$ between -489 and 425 km s^{-1} are present (see Table 6.2) and curiously these are distributed about two offset straight lines in the plot of relative radial velocity (with respect to $V_{\rm sys}$) versus apparent angular distance from the central star as shown in Fig. 6.6. One significant kinematical characteristic of these knots is the narrowness of their observed line profiles (whose half-widths, δV, are also listed in Table 6.2). The observed profile of the [N II] λ6584 Å line from knot 16 (see Fig. 6.4f) is plotted in Fig. 6.5. These observed widths (which include the instrumental width of 11 km s^{-1}) can be as small as 15 km s^{-1} even with radial velocity displacements of several hundreds of km s^{-1}.

6.3 Discussion

These most recent pv arrays of line profiles reveal both the kinematics of the inner core of MyCn 18 and also offer nearly complete coverage of the high–speed knots, which can be investigated in detail with the aid of the new continuum subtracted image. The observationally determined kinematics and morphologies are now discussed in Section 6.3.1 and possible interpretations are considered in Section 6.3.2

Knot	Slit	$V_{\rm HEL}$	$\delta\ V_{\rm HEL}$	$r_{\rm obs}$
2	F	-489	18	47.2
3	D	-424	20	37.7
	E	-455	20	37
		-462	22	40
		-469	21	43
4	D	-403	21	34.5
5	A	-392	21	33.5
	B	-392	20	32.5
	C	-395	15	32
6	D	-360	17	25.5
7	A	-309	20	24.6
	B	-310	17	24
	C	-360	12	25.5
8	E	-287	23	17.3
	F	-276	31	17.5
	G	-267	38	17.5
	H	-262	23	17.8
9	C	-291	17	17
	D	-282	30	17.7
10	B	-261	15	14.5
11	B	95	20	16.4
12	E	153	20	17
	F	146	20	17.4
	G	143	19	17.6
13	B	145	20	19.5
15	G	240	29	28.1
	H	203	48	28.5
	I	177	28	29.1
16	E	259	22	31
	F	252	18	31
	G	250	20	30.5
17	G	270	17	35.5
	H	270	26	35.5
		265	25	36.8
18	E	425	18	52.6
	F	421	20	53.8
19	A	270	25	42
	B	281	30	42

Table 6.2: $V_{\rm HEL}$ (km s^{-1}), observed radius from central star $r_{\rm obs}$ (arcsec) and profile halfwidth δV (km s^{-1}) for each knot identified in each slit. Knots 1 and 14 exist in the image but gave no measurable profile in the corresponding pv array and so are not included. Knot 19 exists in the pv arrays but no corresponding signal was determined in the image. N.B. $V_{\rm sys}$ = -71 km s^{-1}

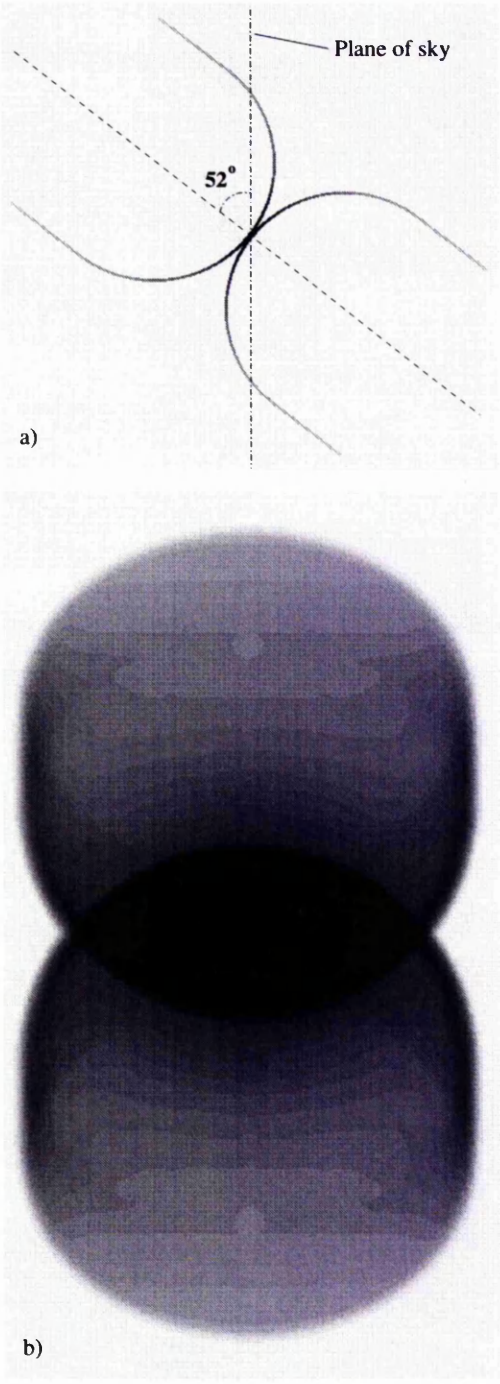

Figure 6.7: a. Cross section from a plane through the major axis of symmetry for the proposed model (b) formed by integrating this section through π about the major axis of symmetry. b. A 3D model composed of 2 extended hemispherical shells back to back (as indicated in a.) integrated along the line of sight. The volume emissivity falls as r^{-2}, where r is the radius from the central point. The nebula is oriented at an angle of 52° from the plane of the sky.

6.3.1 Kinematics and morphology

Firstly, in the image in Fig. 6.1 the bright nebular core appears to be composed of hollow, bipolar cavities, tilted at 52° (with circular cavity sections) with respect to the plane of the sky. This morphology is reasonably simulated by the bipolar structure shown in Fig. 6.7 composed of two hemispherical cavities which change into cylinders further from the star. The pv arrays for the central slits D and E (Figs. 6.3 c & d) along the bipolar axis indicate that accelerating outflows are occurring along the walls of these cavities with a speed for the bright material of ≈ 90 km s^{-1} i.e. 70/sin 52°. Even higher speed wall outflows further from the central star, are occurring in the faintly emitting material (see Figs. 6.3 d–f).

The blue-shifted velocity features at -160, -170 and -180 km s^{-1} in Figs. 6.4(g-i) (similar red-shifted features are seen in figure 3 of Bryce et al. (1997) and marginally detected in Fig. 6.4d) are of a different nature than the high speed knots. Their velocity widths indicate that they are not well collimated. This would be consistent with a rotating disk of material being sampled at different radii. Extremely deep imagery of the nebula obtained with the bright central regions occulted may reveal the origins of these features.

The image in Fig. 6.1 suggests that the high–speed bipolar knots are travelling within $\pm$ 10″ of the nebular bipolar axis and also tilted at 52° to the plane of the sky. The highest speed for any knot is that for Knot 18 in Table 2 for which an outflow velocity of 629 km s^{-1}, at this 52° tilt angle, is found. It is interesting to first consider the observed morphology and kinematics of these

knots before considering the physical mechanisms that could produce them. The ejection mechanism must produce a series of knots with a range of radial velocities. Furthermore, the apparent radial distances must scale with these radial velocities (Fig. 6.2) and, significantly, very narrow line profiles must also be explained.

Two distinct classes of models to explain these observations may be identified. The first achieves a spread in radial velocity by varying the angle in time between the outflow velocity and the line of sight. Such bipolar rotating episodic jet (BRET) models have been investigated by López et al. (1993a) and Palmer et al. (1996) . A variant includes a model with a precessing bipolar episodic jet as considered by Cliffe et al. (1995). The second class contains subsets in which the speeds of the knots can vary and either the time from ejection, the acceleration, the spatial origins of the knots or all can vary.

Constant speed and rotating direction

This class of model was considered in some detail in Bryce et al. (1997). It was thought that some degree of point symmetry (in positions with respect to the core and in the magnitudes of the radial velocity differences) of pairs of knots in MyCn 18 could indicate a rotating (bipolar) direction of episodic emission. It was surmised that the plane of this simple rotation of the ejection axis would then have to be nearly perpendicular to the plane of the sky but with all the knots travelling at the same speed. The knots' ejection axes would, therefore, not be co–incident with the nebular bipolar axis. In the light of the

new continuum subtracted image this now seems an unlikely possibility as the knots appear to be within 10″ of the bipolar Hourglass axis projected onto the plane of the sky and there would seem to be no reason for them not to be within 10″ of this same axis projected onto an orthogonal plane.

One diagnostic of this BRET configuration would be to observe knots beyond the turning point in the $|v_r|$ versus radius curve as depicted in figure 3c of Bryce et al. (1997) (where $|v_r|$ is the magnitude of radial velocity). Such a turnover has not been observed in the present, more extensive observations. Of course it is possible that knots have not been ejected beyond this turnover point in the lifetime of the knot ejection process in MyCn 18. However, it seems unlikely, though not impossible, that this rotating bipolar jet model is applicable to MyCn 18.

Changing speed within an ejection cone

In its simplest form all the knots are ejected at the same time, with a range of speeds within a fixed ejection cone. This simplistic model would produce a linear relationship between distance and velocity with a scatter governed by the opening angle of the cone. From separate linear fits to the data (Fig. 6.6) it can be seen that the knots would have to have originated on the opposing sides of the nebula at some 10″ from the centre. As no physical mechanism for this process occurring seems plausible this model is not investigated further here.

A modification to this simplest case may be made by also allowing the ejections

to occur over a period of time. The faster knots would have time to travel further than expected (from the distance of the slower knots) if they were ejected earlier. In this case, simple comparison of the gradients of lines joining the knots to the origin indicates that for the present data the innermost knots would have been travelling for approximately 3/4 the time of the faster knots. If one takes the kinematical age of the furthest knots to be 1250 yr (Bryce et al. 1997) a time-scale for the ejection period of around 300 yr is found.

Of course if accelerations or decelerations are introduced one can, with a combination of temporal/spatial origins or ejection speeds, form a multitude of models to reproduce the linear relationships found here. Further terms result in further degeneracy from the simple model and are best considered from a physical, rather than mathematical, perspective.

Incidentally, the precessing bipolar jet (Cliffe et al. 1995) or a 'wandering' episodic bipolar jet variants of the first class of model (§6.3.1) may be more closely related to this class of model. When a small precessional angle is assumed the precessing jet tends towards a non–rotating jet and thus cannot be ruled out.

6.3.2 Structure and dynamics

Formation of the inner core

The present pv arrays and the morphology of the bright core of MyCn 18 bear similarities to those of Mz 3 which Meaburn & Walsh (1985) model as the flow of ionized gas along the wall of an evacuated cavity. Numerical interacting

stellar winds model codes can reproduce such shapes and the associated velocities satisfactorily. The high speed knots are neither expected nor accounted for by such models but if, as argued below, these knots have little effect on the structure of the hourglass shape then these models could still be applied to the bright core of MyCn 18.

Sahai et al. (1999) surmise that interacting stellar winds models can reproduce the main hourglass shape. However, they reveal the very innermost regions to be more complicated than expected from these models and suggest a close binary star to be responsible for the differences.

Models for the high speed knots

In Bryce et al. (1997) several possibilities for the kinematical behaviour of the high speed knots were considered. The new data have shown that the initial observations (Bryce et al. 1997) had indeed detected the outermost knots and does not constrain the BRET model further. A simple, single event, grapeshot model was discussed briefly and discounted in Bryce et al. (1997). It is however worth examining variations on this basic theme.

The knotty outflow could have originated from the disruption of a pre–existing wind-blown shell. If this then generated a collection of outwardly coasting clumps then a velocity-distance straight line fit through the clumps should be constrained to pass through the position and velocity of the precursor shell rather than the origin (which was used in Bryce et al. (1997) since the grapeshot ejection was assumed to originate in the core). However, if the knots

form as the result of a break up of a shell via the Rayleigh-Taylor instability then the knot velocities will be of the order of the shell velocity just prior to break up. The low expansion velocities of the undisrupted portions of the bipolar shell imply that if this is the case there must have been a severe velocity change from the pole to the equator. An expansion into a plane parallel density gradient with a small scale height would help produce such a velocity spread but it is very hard to see how the highest velocity knots could be generated in this way (see e.g., Pascoli 1992 for a discussion of the various mechanisms that may lead to such a density enhancement).

Alternatively, the knots could be ejected all at the same time but with a range of initial masses (velocities could conceivably be constrained if the knots form from a fragmenting shell). The lower mass knots will be slowed to a greater degree by their passage through the circumstellar medium than the higher mass knots. Very approximately, a knot of uniform number density $n_{\rm k}$ and radius $r_{\rm k}$ travelling at $v_{\rm k}$ through a medium with average density $n_{\rm i}$ will be disrupted and slowed after it has travelled through a column length $l \sim r_{\rm k}(n_{\rm k}/n_{\rm i})$ containing about the same amount of mass as itself. The low speed knots have reached a distance of $l \simeq 15''$ and appear to be resolved in these observations to be $r_{\rm k} \lesssim 2''$. If they are beginning to be slowed down (Section 6.3.1) then the density contrast between the slowest knots and the circumstellar medium is approximately $n_{\rm k}/n_{\rm i} \lesssim 10$. Local electron densities in the ionized gas could be measured by use of [S II] $\lambda\lambda$6717, 6730 Å line ratios. However, the narrow profiles of the knots favours photoionization of clumps of

gas rather than excitation behind individual bow-shocks (see Figs. 6.4 and 6.5) and would therefore imply little interaction between the knots and the ISM. The masses of the clumps must of course remain uncertain since only the ionized component is detected in optical emission lines and they may possess neutral cores.

Another possibility is that the MyCn 18 knots are the remnants of disrupted polar blobs formed in the AGB phase. Morris & Reipurth (1990) have observed such features around the bipolar pre-planetary nebula IRAS 09371+1212, a likely precursor to a bipolar PN. Could the subsequent switch-on of a fast stellar wind somehow disrupt these polar blobs? The high velocity knots of MyCn 18 may then be explained by the flow of a fast stellar wind around individual slow moving clumps. Against this interpretation is the lack of broad velocity features for each of the knots. Their localised appearance in the pv arrays strongly suggests that the measured velocities are the bulk velocities of the knots themselves (see the narrow profile in Fig. 6.5). A further more general argument against this interpretation is that mass-loading a hypersonic flow in this way will lead to the deceleration of the flow (Hartquist & Dyson 1993) by simple momentum conservation i.e. the measured velocities should decrease rather than increase with distance.

Hypothetically, if a very strong magnetic field is present then García-Segura et al. 1999 show, using 2-D models, that it is possible to generate a high speed jet (with increasing flow speed with distance) along a bipolar PN axis. They suggest that if such a jet were to break up via instabilities associated with

magnetically confined plasmas then the knotty outflow of MyCn 18 may be reproduced.

A nova–like origin for the knots

A possibility that has not been previously considered is that a nova–like phenomenon has played a part in the generation of the high speed knots in MyCn 18. This is explored below.

Sahai et al. (1999) detect a fraction of the knots in their HST frames and go on to estimate the total mass of the knots as $\sim 10^{-5}$ $M_{\odot}$ (although this is dependent on the highly uncertain distance to MyCn 18). The outflowing speeds of the knots can be estimated to be from several hundred up to over 600 km s^{-1}. Both the total mass and speed of the knotty outflow are typical of a nova ejection. A nova requires a close binary to enable Roche lobe overflow. Nova ejecta can be clumpy (see, for example, the striking images of GK Per in Slavin, O'Brien & Dunlop 1995) and can also be bipolar (Bode & Evans 1989). Sahai et al. (1999) favour a close binary to generate the morphology of the very innermost regions of MyCn 18. Such a binary central star could also be capable of undergoing a nova–like explosion to form the knotty outflow (the main body of the PN would be formed in the usual way however).

A recurrent nova ejection for the knot formation is a particularly attractive possibility since there is a degree of symmetry in velocity and position in opposing knots or clusters of knots (evident from inspection of Figs. 6.2 and 6.4) and typical recurrence time-scales are between $\sim 20 - 80$ yr (Webbink et al. 1987).

Several ejections could have taken place within the suggested 300 yr period the knots may have been ejected over. The velocity range observed in the knotty outflow may simply be because nova ejections do not occur with a single well-defined velocity (Bode & Evans 1989) and successive outbursts may vary in average ejection speeds. Lépine et al. (1999) report the first direct measurement of acceleration in the outflow of a recurrent, or classical, nova in U Scorpii.

It is worth pointing out that the nova explosion(s) may not need to be bipolar in order that the ejecta be confined to a cylinder about the PN axis. If the nebula is ionization bounded in all directions apart from close to the Hourglass axis then only those knots illuminated by the UV photons from the central star will be ionized. The very low knot filling factor makes it unlikely that they could completely disrupt the hourglass shape. However, the filaments of nebulosity imaged by Sahai et al. (1999) which extend beyond the main Hourglass shape could be due to the passage of knots through the ionized walls.

6.4 Conclusions

It has been argued that the Hourglass nebula is composed of two opposing nearly hemispherical extended cavities inclined at an angle of some 52°.

Knots were ejected over a period of 300 yr at hypersonic ($\leq$ 660 km s^{-1}) speeds. These knots are now visible due to photoionization by the central star

rather than shock ionization.

A variety of simple models may reproduce the kinematics observed in the knots of MyCn 18. Dynamically, the most plausible explanation seems to be that the high speed knotty outflow from MyCn18 is the result of a (possibly recurrent) nova–like ejection from a central binary system. This is in harmony with the considerations of Sahai et al. (1999) who favour a close binary to generate the morphology of the very innermost regions of MyCn 18.

Chapter 7

The young bipolar planetary nebula Mz 3

7.1 Introduction

Mz 3 (also designated PN G331.7-01.0) spans more than 50″ on the sky. This bright proto/young planetary nebula (PN) consists of a dense ionized core with bright protruding, inner, approximately spherical, bipolar lobes (IBL; Fig. 7.1). These are contained within a much more extensive filamentary bipolar nebula (Evans & Thackeray 1950; Cohen et al. 1978). Lopez & Meaburn (1983) found the IBL to have an expansion velocity of $V_{\rm exp} \simeq 50$ km s^{-1}. They also detected wings to the Hα profiles that extend to $\pm$1200 km s^{-1} which were attributed to electron scattering within the hot ionized inner regions close to the star. Mz 3 is a dusty system. It is bright in the far infrared (Phillips & Mampaso 1988) with densities in the range $10^3 - 10^5$ cm^{-3}. Mz 3 has been imaged at 10

microns by Quinn et al. (1996) who find extended emission from warm (100-130 K) dust that correlates well with the visible outer bipolar lobes. V-band imaging polarimetry by Scarrott, Scarrott & Wolstencroft (1994) suggests that the inner bipolar lobes are filled with hot ionized gas bounded by swept up shocked gas from the fast stellar wind. The dust in the nebula is most likely to be radiatively heated by direct stellar illumination and trapped Lyman α photons (Scarrott, Scarrott & Wolstencroft 1994).

Two outer, bipolar, filamentary lobes (OBL1 and 2; Fig. 7.1) were identified by Meaburn & Walsh (1985). The more prominent but narrower of these, OBL1, has parallel walls out to 40″ north and south of the core. Meaburn & Walsh (1985) deduced that its bipolar axis is at $\simeq 20$ deg to the plane of the sky. The position-velocity (pv) arrays of profiles perpendicular to OBL1 exhibit 'velocity ellipses' down its whole length. Expansions of the walls of $\simeq$ 90 km s^{-1} in directions away from the central star were implied. OBL2 encompasses OBL1 and was found to exhibit similar velocity ellipses but with a wall expansion of $\simeq$ 180 km s^{-1}, again away from the star (Meaburn & Walsh 1985). Na I absorption lines were also detected in the atomic recombination continuum emission from the compact ionized nebular core. The presence of a neutral torus with an ionized inner surface with an electron number density of $n_e \sim 2 \times 10^4$ cm^{-3} is indicated. Both are expanding at $\simeq 40$ km s^{-1}.

New spatially resolved spectral observations which have lead to the discovery of a pair of hypersonic knots of emission at the apices of the inner bipolar lobes of Mz 3 are presented. Recently available HST imagery reveals the

morphological features that correspond to these velocity data. The kinematics of the hypersonic knots are compared with those of similar speed but different morphologies in MyCn 18 and He 2-111 and KjPn 8. Physical mechanisms that may be responsible for producing such dramatic flows are briefly discussed. A plausible model for the outer bipolar lobes is also developed after consideration of their kinematics along with the HST imagery.

7.2 Observations and Results

7.2.1 HST imagery

In Fig. 7.1 a pair of narrow band Hα (F656N) WFPC2 images generated from archive data are displayed (Proposal IDs 6856 & 6502, John Trauger, June 1998). The IBL is obscured in the portions close to the core. The two components of the IBL are morphologically different. There is a narrow protrusion (Y) to the southern lobe and a broader extension (X) to the northern lobe (Fig. 7.1). Fig. 7.1(b) is an enlarged view of the inner regions of the southern half of the nebula. Feature Y is more clearly seen.

The IBL has a distinctly mottled appearance, reminiscent of the Homunculus in η Carinae (Morse et al. 1998). A system of cometary knots is seen in Fig. 7.1 that extend to several tens of arcseconds from the central star.

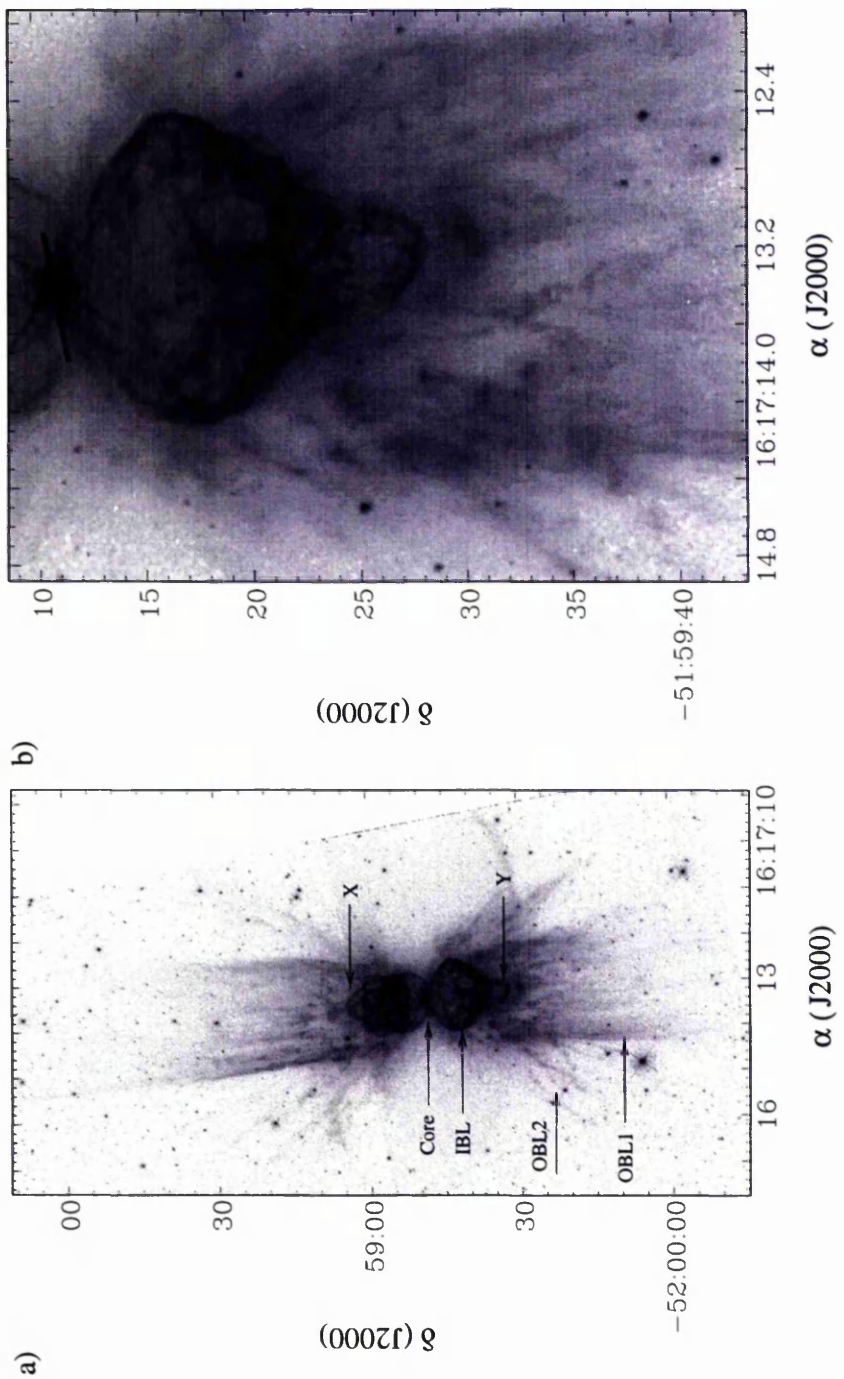

Figure 7.1: WFPC2 F656N narrow band Hα archive images of Mz 3. a) The whole nebula in the light of Hα. The labels indicate features described in the text. b) An enlarged view of the southern half of the nebula. Feature Y and the patch of emission to the south of it are clearly seen. Numerous cometary knots with overlapping tails are evident in both images, particularly in b). (From Redman et al. (2000))

7.2.2 Echelle spectra

Spatially resolved, longslit echelle spectra and Hα and [N II] λ6584 Å emission line images of Mz 3 were obtained with the Manchester echelle spectrometer (MES; Meaburn et al. 1984) combined with the f/7.9 Cassegrain focus of the Anglo–Australian telescope (AAT). A Tektronix CCD with 1024×1024 24 μm square pixels was the detector. The observations were made on 28 March, 1999 using a 100 Å wide interference filter to isolate the 87th order containing the Hα and [N II] λ6584 Å emission lines. A slit width of 150 μm ($\equiv$ 10 km s^{-1} and 1″) was used. The CCD was binned by a factor of two in the spatial direction to give 512 × 0″.32 pixels along the slit length. Each integration was debiased and wavelength calibrated to better than 0.5 km s^{-1} using ThAr arc lamp spectra obtained between exposures.

The slit was orientated with the major bipolar axis of the nebula and passes through the central star. The resulting pv array of line profiles from the slit position is displayed in Fig. 7.2. In Fig. 7.2(a) the linear display highlights a pair of high velocity features at $V_{\rm hel} \simeq -230$ and 120 km s^{-1}. Their positions along the slit correspond to X and Y in Fig. 7.1(a) and they are labelled as such in Fig. 7.2(a). The systematic radial velocity is measured from Fig. 7.2(b) to be $v_{\rm sys} \simeq -55$ km s^{-1}.

Meaburn & Walsh (1985) calculated that the northern and southern components of OBL1 are orientated at 13° and 25° to the plane of the sky respectively. It is assumed that the IBL has an orientation intermediate between these two values of $\simeq$ 20° to the plane of the sky. This yields an outflow velocity of

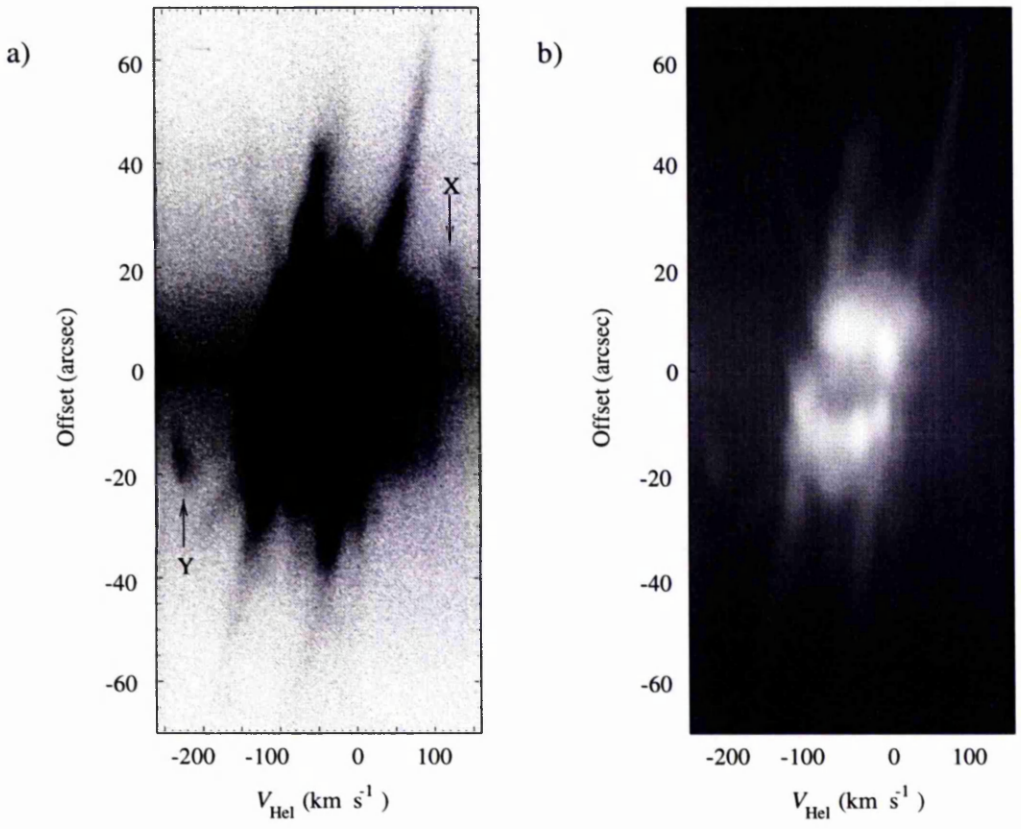

Figure 7.2: [N II] λ6584 Å Position velocity arrays of the inner core of Mz 3 from a slit position passing through the central star aligned along the major bipolar axis. The deep linear display (left) highlights the velocity features at approximately -250 km s^{-1} and 120 km s^{-1} in both pv arrays. These lead to de-projected velocities of around 500 km s^{-1} (§7.2.2). In the logarithmic display (right) the knotty substructure of the inner core can be discerned

$\simeq 510$ km s^{-1} for features X and Y.

Fig. 7.2(b) is a logarithmic display of the same data. The inclined velocity ellipse from the IBL indicates that it is inclined somewhat to the line of sight, consistent with the results of Meaburn & Walsh (1985). The knotty substructure of the IBL data is in accord with the mottled appearance of the IBL in the HST images in Fig. 7.1.

7.3 Discussion

7.3.1 Proper motions

In principle, one can use high speed motions on the plane of the sky to determine expansion proper motions and hence distances. Previous narrow band imaging (obtained in June 1983 with seeing of around 2″) of Mz 3 and included in the thesis of Whitehead (1989) were compared with the HST data for evidence of proper motions in X and Y. Over the $t \simeq 15$ yr time frame a proper motion of approximately one arcsecond is marginally detected. If this is taken as an upper limit, $\theta \lesssim 1''$, and if the velocity tangential to the line of sight is (using the estimate of 20° as above) $V_t \simeq 480$ km s^{-1} then the distance D can be found from

$$D(\mathrm{pc}) = 0.216 \frac{\mathrm{V_t\ (kms)\ T\ (yr)}}{\theta\ (\mathrm{arcsec})}, \tag{7.1}$$

and is $\gtrsim$ 1500 pc. Of course, this distance is strongly dependent on the actual angle to the plane of the sky used, since this angle is small. Previous estimates of the distance to Mz 3 are $\sim$ 1.8 Kpc (Cohen et al. 1978); $\lesssim$ 1 Kpc (Lopez & Meaburn 1983) and $\sim$ 3.3 Kpc (van Der Veen, Habing & Geballe 1989). Even if Mz 3 were placed at 3.3 Kpc, the extremely high velocities of the protrusions X and Y mean that motions of 0″.1 could be discerned by the HST or ground based adaptive optic telescopes on a time-scale of just 3 years.

Note that it is implied that the measured radial velocities correspond to movement of the emitting feature. It is entirely possible for an emission region to be stationary but with a flow-through of gas (e.g. FLIERS as recombination fronts at the end of mass-loaded jets; Redman & Dyson 1999) in which case there would be no proper motion involved. This is almost certainly the case for the numerous bright cometary knots in the vicinity of Y (see Fig. 7.1b). They are morphologically very similar to the knots in the Helix nebula (Meaburn et al. 1998b) and in the core of Abell 78 (Borkowski, Harrington & Tsvetanov 1995) and are likely therefore to be dense clumps with neutral cores being stripped of mass by the stellar wind.

7.3.2 The kinematics of OBL1 and OBL2

The clumps in Mz 3 could offer an explanation for previously puzzling kinematics of OBL1 and OBL2. The overlapping tails of the clumps appear to merge to form the two lobes (Fig. 7.1). Although the emitting material in OBL1 is clearly confined to a cylindrical region, Meaburn & Walsh (1985)

found velocity ellipses with implied expansion velocities of $\simeq 90$ km s^{-1} from slit positions perpendicular to cylindrical axis. The separation of the long, almost parallel features in the pv arrays in Fig. 7.2 corresponds to the minor axes of the Meaburn & Walsh (1985) velocity ellipses. Given such expansion velocities, the cylindrical OBL1 should have fanned out into a cone. However, if OBL1 is the result of a cylindrically distributed collection of slowly moving clumps then a fast radial wind from the central star will result in the clump tails pointing away from the star. The velocity ellipses would then be due to the tails possessing differing angles to the line of sight with tails on the near side of OBL1 appearing blue shifted and tails on the far side appearing red shifted. Incidentally, similar lobes to OBL1 in the PN NGC 6302 could have the same kinematical explanation (Meaburn & Walsh 1980)

7.3.3 Global dynamics

Most models for bipolar nebulae around stellar objects assume that there is some sort of equatorial-polar variation in the mass loss from the star. This can be either the result of a uniform dense slow wind being impacted by a fast wind of varying momentum flux or, more usually, a variation in the slow wind. In planetary nebulae, this wind is generated by mass loss from a post-AGB star (see e.g. Frank & Mellema 1994). There are several possible mechanisms for generating density gradients in the AGB wind: a compact binary companion either spins up the dense wind in the orbital plane during a common envelope phase (Soker 1998b) or a detached binary affects the wind directly (Mastrode-

mos & Morris 1999); a toroidal component to the magnetic field impedes the outflow in the equatorial direction (Pascoli 1992); a fast rotating AGB star will result in an equatorially focussed outflow (Bjorkman & Cassinelli 1993). In all these cases, the subsequent fast hot wind from the central stellar remnant then blows into a plane stratified density environment and bipolar morphologies then quite naturally arise. There is ample evidence, from optical and infrared imagery and from spectropolarimetry that the expected constraining dense disk of material is present in Mz 3 (see §7.1)

The models predict that the highest velocity portions of the expanding PN shell are expected to be found along the major symmetry axis of the nebula, as one would expect, and to have maximum speeds of the order of several $\times 10$ km s^{-1}. However, in recent years several planetary nebulae have been found to have highly supersonic knotty components to their outflows. He 2-111 has two faint outer lobes beyond a comparatively small bright core (Meaburn & Walsh 1989). The extreme tips of these bipolar lobes have speeds $\gtrsim$ 350 km s^{-1}. Corradi & Schwarz (1993) have shown similar high speed phenomena in He 2-104. MyCn 18 has an even more extreme outflow, with a collection of around 20 ionized knots with speeds relative to the star that increase systematically up to 600 km s^{-1} (Bryce et al. 1997; O'Connor et al. 2000). Such features are beyond the parameter range of interacting stellar winds models and alternative physical mechanisms which act either alongside of or in place of these models should be explored.

Mz 3 is now the latest planetary nebula in which such hypersonic outflows have

been discovered. These velocity features can be compared to those in He 2-111 and MyCn 18. A wandering episodic jet may be responsible for shaping He 2-111 in a similar manner to that in KjPn 8 (Steffen & López 1998, see also the review of jets in PNe by Mellema 1996). Alternatively, O'Connor et al (2000), suggested that a nova-like explosive event in the central binary system in MyCn 18 was responsible for the bipolar hypersonic knotty outflow.

If an episodic jet has operated within Mz 3 to produce OBL1 and OBL2 prior to generating the IBL then it must have retained its axis, unlike KjPn 8 where several jet actions with distinct ejection times and directions have operated. The open ended bipolar morphologies of OBL1 and OBL2 could then be due to successive jet actions with a fixed axis. In this scenario, features X and Y could be the result of the latest jet breaking through the IBL. However, the morphology of the IBL is more like that of a standard pressure or wind driven bubble and the kinematics of the IBL do not suggest the action of a jet as the the shaping mechanism.

Mz 3 may be a much younger object than KjPn 8 and He 2-111 and OBL1 and OBL2 are more likely to be remnants of the AGB wind now being illuminated by the ionizing star. A close inspection of the HST images in Fig. 7.1 shows that the intersection of OBL2 with the IBL is marked by a brightening of the IBL, particularly in the southern half of Mz 3. OBL2 may mark a transition from dense constraining material, perpendicular to the bipolar axis of Mz 3, to a more rarefied environment. It is suggested that as the IBL expands, those portions that cross this boundary, driven by the pressure of the hot ionized

cavity will rapidly accelerate due to the sudden decrease in constraining matter. This cannot continue for long – an acceleration of a dense shell overlying more tenuous gas will result in a Rayleigh-Taylor instability developing and the break up of the accelerating part of the shell. This 'blow-out' effect has been well studied for other astrophysical situations (for example, giant shells in the plane of the galaxy elongate perpendicularly to the plane of the galaxy and eventually vent the hot gas inside the shell into the halo via a galactic chimney; Norman & Ikeuchi 1989). The end result of this process in Mz 3 may well be an hourglass shaped nebula such as MyCn 18 – since the driving pressure will have been vented, only the tips of the bipolar lobes will be forced through the constraining remnant AGB material. Furthermore, it is speculated that the break-up of features X and Y will result in a collection of high speed bullets coasting outwards, reminiscent of the dramatic MyCn 18 knots. In conclusion, previous observations indicate that Mz 3 is a young system surrounded by dense dusty circumstellar matter in a plane perpendicular to the bipolar axis of the nebula. To generate the 500 km s^{-1} outflow reported here, a model in which the tips of the IBL have encountered a much lower density environment and are undergoing a 'blow-out' is favoured.

Chapter 8

Conclusions and suggestions for further work

In its first use MOMI detected a giant lobe in the optical nebula around P Cygni. The feature corresponds spatially with an arc of emission in the radio maps of (Skinner et al. 1998). It was suggested that this feature might be connected to the LBV P Cygni and furthermore might be evidence of an historic, highly asymmetric eruptive event. As the mechanism for radio emission is mostly thermal, it was suggested that the optical feature may have been radiatively ionised by a flash of UV radiation from P Cygni. Further studies have now been done on the optical arc. Meaburn, López & O'Connor (1999) have found evidence for a kinematical association of the arc with P Cygni, however, clear evidence for a counter lobe or a southern counterpart was not found. Indeed, the kinematical information presented showed no change in the direction of the flow across the nebula, something that would be expected if

the outflow were bipolar. The nature and geometry of an eruptive event that would cause the strange nebular morphology is not straightforward. The kinematical age for the lobe was estimated by Meaburn, López & O'Connor (1999) to be $\sim$ 20,000 yrs. Although kinematical ages are model dependent and cannot be relied upon completely, this 20,000 yr age found by Meaburn, López & O'Connor (1999) places the eruptive event prior to the LBV phase which is thought to last only 10,000 yrs. Further observations of the P Cygni nebula (Meaburn et al. 2000) confirm and elaborate on the findings of Meaburn, López & O'Connor (1999). These latest observations are expected to clarify the nature of the giant lobe. Further work is needed to determine the nature of the possible giant nebula around P Cygni at other wavelengths.

The first use of the occulted Fabry-Perot mode of MOMI on the inner shell of P Cygni was delayed due to high atmospheric dust levels during the commissioning run on the INT. High dust levels in the atmosphere and partial moon illumination combine to raise the signal to noise levels due to scattering in the atmosphere and change the observing conditions during the scanning sequence. This work is yet to be completed and will give a detailed insight into the geometry and kinematics of the bright inner shell in both the light of [N II] λ6584 Å and [Ni II] λ7378 Å .

The ghosts produced by the interference filter in the pupil have proved troublesome. For applications where the large field of view of MOMI is not required a secondary mode of operation would prove beneficial. In this secondary mode the field of view would be restricted ($\approx 5'$ on the INT) and thus the interfer-

ence filter could be positioned between the occulting mask and the field lens. Ghosting would occur due to multiple reflections between the mask and filter though the ghosts could be directed away from the optical path by tilt tuning of the interference filter.

Preliminary investigations into the feasibility of rotating an apodising mask in the pupil reveal that, for the NOT telescope, it would be relatively simple to synchronise the mask orientation to that of the field rotator. The mechanical design of the mask rotator would need developing but would not be an obstacle to the implementation of such a device.

High speed (hypersonic) outflows from PNe are not reproduced by the present ISW models without additional assumptions which may or may not have observational support (e.g. strong magnetic fields). The observations presented in this thesis of MyCn 18 and Mz 3 would seem to favour a more explosive event for the origins of hypersonic knots. A full kinematical study of the Mz 3 nebula is now needed to fully understand the nature of the high speed feature observed. It would be most beneficial if the velocity field over the whole area of the protruding lobes could be determined.

Appendix A

T_e from Hα and [N II] λ6584 Å line profiles

An emission line, when observed by a spectrometer, is a convolution of several profiles with its halfwidth given by

$$\delta\lambda^2 = \delta\lambda_I^2 + \delta\lambda_{Tu}^2 + \delta\lambda_{Th}^2 \ , \tag{A.1}$$

where $\delta\lambda_I^2$ is the instrumental profile, $\delta\lambda_{Tu}^2$ is the profile due to turbulence in the emitting region and $\delta\lambda_{Th}^2$ is the thermal broadening. The observed emission line may be split into multiple components by spin-orbit coupling, this must be considered when observing emission lines (Meaburn 1970).

An expression can be found for an emission line broadened due to thermal velocity components for gas in equilibrium. The number distribution is given

by

$$dN(v) = N_o e^{-\frac{mv^2}{2kT}} dv \ , \tag{A.2}$$

where m, v, k, T have their usual meanings and N_o is a constant of proportionality. The light observed is Doppler shifted according to the non-relativistic formula

$$\delta\lambda = \lambda_o \frac{v_z}{c} \ , \tag{A.3}$$

where v_z is the line of sight velocity and c is the speed of light in a vacuum. As the intensity is proportional to the number density the intensity distribution can be written in terms of $\delta\lambda$ and T_e, the electron temperature, as

$$I(\delta\lambda) = I_o e^{-\frac{Mc^2}{2kT_e}(\frac{\delta\lambda}{\lambda_o})^2} d(\delta\lambda) \ . \tag{A.4}$$

The half–width, $\Delta_{\frac{1}{2}}\lambda$, at half–maximum is found when $I = I_o/2$, that is, when

$$e^{-\frac{Mc^2}{2kT_e}(\frac{\delta\lambda}{\lambda_o})^2} = \frac{1}{2} \ . \tag{A.5}$$

Thus the full–width at half–maximum is given by,

$$\Delta\lambda_{Th} = \frac{2\lambda_o}{c}\sqrt{\frac{2\ln 2\ kT_e}{m}} \ . \tag{A.6}$$

This relationship allows one to calculate T_e from the FWHM of a thermally broadened line profile.

As stated previously the observed emission line is a convolution of several functions, the thermally broadened line being one of them. To isolate the

thermally broadened component the turbulently broadened component and the instrumental profile component have to be subtracted. By observing two emission lines which occur spectrally close to each other and assuming that the instrumental profile is identical at each of the wavelengths observed subtraction of the instrumental profile component is possible. Furthermore, if the two emission lines are from gases with similar turbulent motions the turbulently broadened component may be subtracted.

For the observations considered here, Hα and [N II] λ6584 Å are separated by $\sim$ 22 Å and the assumption that the instrumental profile at these wavelengths is constant can be be made. One must also assume that the turbulently broadened components are the same for Hα and [N II] λ6584 Å.

The thermal broadening of atomic line profiles is inversely proportional to the square root of the mass, Eqn. A.6, i.e.

$$\Delta\lambda_{Th} \propto \sqrt{\frac{1}{m}} , \tag{A.7}$$

and, as the ratio of the mass of Hα to the mass of [N II] λ6584 Å is $\frac{1}{14}$,

$$\Delta\lambda_{Th}[NII] = \sqrt{\frac{1}{14}}\Delta\lambda_{Th}[H\alpha] . \tag{A.8}$$

This leads to the relationship

$$\Delta\lambda[H\alpha]^2 - \Delta\lambda[NII]^2 = \frac{52 \ln 2 \ \lambda_o^2 k T_e}{7c^2 m_p} , \tag{A.9}$$

where m_p is the mass of a proton, the effective mass of Hα, λ_o is the wavelength of Hα and the $\Delta\lambda$'s are the full-widths at half maximum of single emission lines from Hα and [N II] λ6584 Å. The observed Hα emission line has fine–structure splitting, (Meaburn 1970). Dyson & Meaburn (1971) investigated the structure of the emission line and found that the observed line could be approximated by the sum of two single, identical Gaussian components separated by 0.14 Å corresponding to the most significant fine structure emission lines.

The sum of two Gaussians with equal FWHM and displaced by $2x_o$ is simply

$$I(x) = e^{\frac{-(x-x_o)^2}{\sigma^2}} + e^{\frac{-(x+x_o)^2}{\sigma^2}}, \tag{A.10}$$

where σ is the halfwidth at the $\frac{1}{e}$ height, and is non-Gaussian. This can be expanded and the exponents collected to give

$$I(x) = e^{\frac{-(x^2+x_o^2)}{\sigma^2}}(e^{\frac{2x_o x}{\sigma^2}} + e^{\frac{-2x_o x}{\sigma^2}}), \tag{A.11}$$

The exponentials in x can be expanded as a power series and, as this series is convergent for all x, the function can be approximated as

$$I(x) = 2e^{\frac{-(x^2+x_o^2)}{\sigma^2}} e^{\frac{2x_o^2 x^2}{\sigma^4}} . \tag{A.12}$$

This is a Gaussian function and has a full width at half maximum approximately by

$$(FWHM)^2 = 4\ln 2\ (\sigma^2 + 2x_o^2)\ , \tag{A.13}$$

for $\frac{x_o}{\sigma} < \frac{1}{\sqrt{2}}$. As $4 \ln 2 \ \sigma^2$ can be identified as the full width at half maximum of the component Gaussians squared, Eqn. A.13 can be written,

$$(FWHM)^2 = (FWHM_c)^2 + 2 \ln 2 \ x_s^2 \ , \tag{A.14}$$

where x_s is the separation of the component Gaussians and $FWHM_c$ is their full width at half maximum.

Equation A.14, Eqn. A.9 and the approximation of Dyson & Meaburn (1971) can be combined to give a relationship between the observed Hα and [N II] λ6584 Å emission lines and the electron temperature,

$$\begin{aligned} T_e &= 49176(\Delta\lambda_{obs}[H\alpha]^2 - \Delta\lambda_{obs}[NII]^2 - 2 \ln 2 \ x_s^2) \ K \ , \\ &= 49176(\Delta\lambda_{obs}[H\alpha]^2 - \Delta\lambda_{obs}[NII]^2) - 1336 \ K \ . \end{aligned} \tag{A.15}$$

A more rigourous method for relating the observed and component Gaussians is one in which Gaussians are fitted numerically to the Hα line splitting model of Dyson & Meaburn (1971). A linear fit to the FWHM of the observed profile against the component profile is shown in Fig. A.1 along with the approximate relationship given in Eqn. A.15, variances are shown in Fig. A.2.

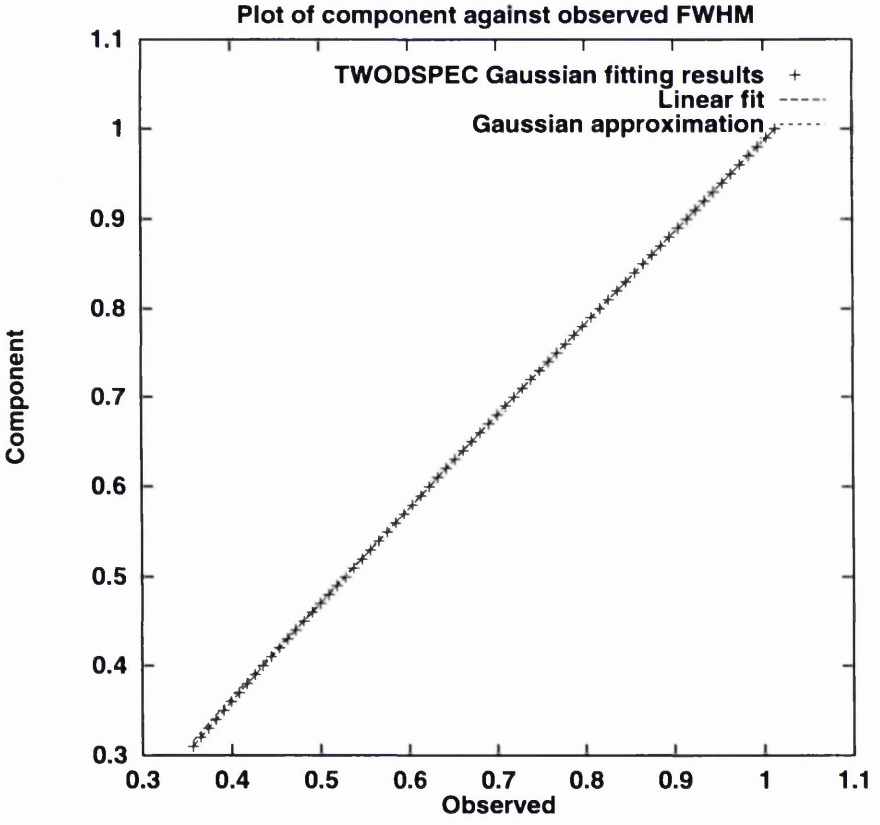

Figure A.1: The Gaussian approximation and the polynomial fit to simulated double Gaussian components against observed Hα profile FWHM.

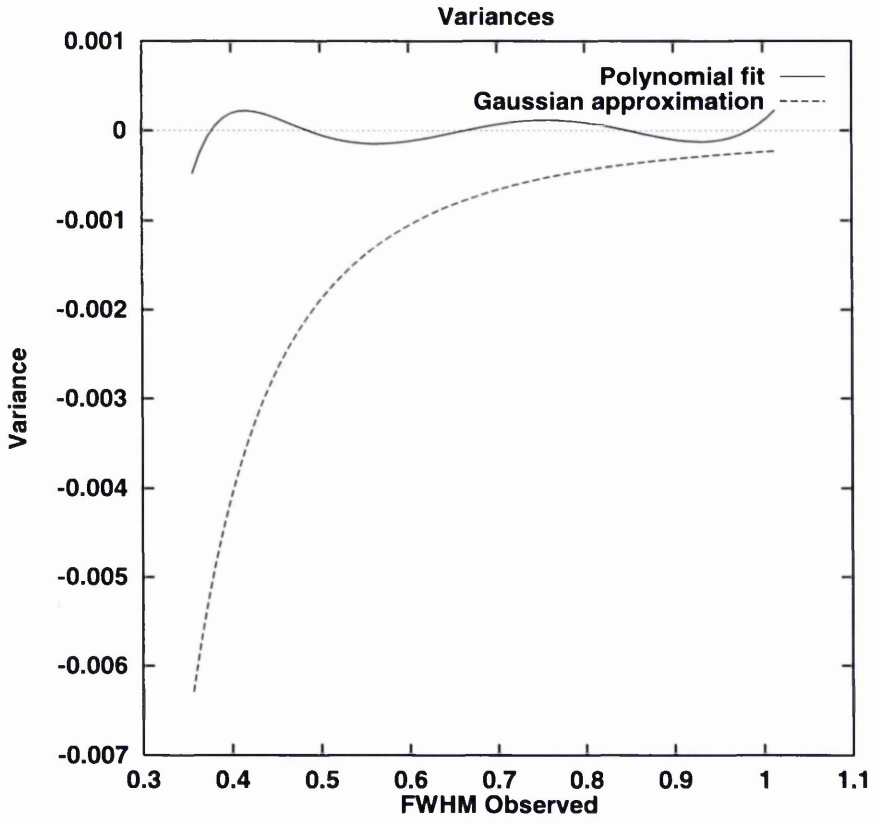

Figure A.2: Variances in the Gaussian approximation and the polynomial fit from simulated double Gaussian data against observed Hα profile FWHM.

Appendix B

Fabry–Perot Etalons

Referring to Fig. B.1, if a monochromatic plane wave of radiation, of wavelength λ is incident on a plane–parallel slab of refractive index μ with surface that partially reflect (r) and transmit light (t) then at each surface two beams will be generated. Furthermore, if the radiation was incident on the first surface at an angle θ to the normal then the phase lag, ϕ, between two adjacent emerging waves (as indicated in Fig. B.1) will be

$$\phi = 4\pi\mu\frac{d}{\lambda}\cos\theta, \tag{B.1}$$

where d is the thickness of the slab as in Fig. B.1.

If the emerging light is brought to a focus by a lens (L_2) then there will be constructive interference between waves separated in phase by $\phi = 2\pi n$ where n is an integer. Thus, for a wavelength λ, there will be a set of allowed θs[1]

[1]Strictly, a wavelength dependent phase change on reflection occurs, in which case ϕ may be replaced by $\delta = \phi + 2\chi$ where χ represents the phase change on reflection

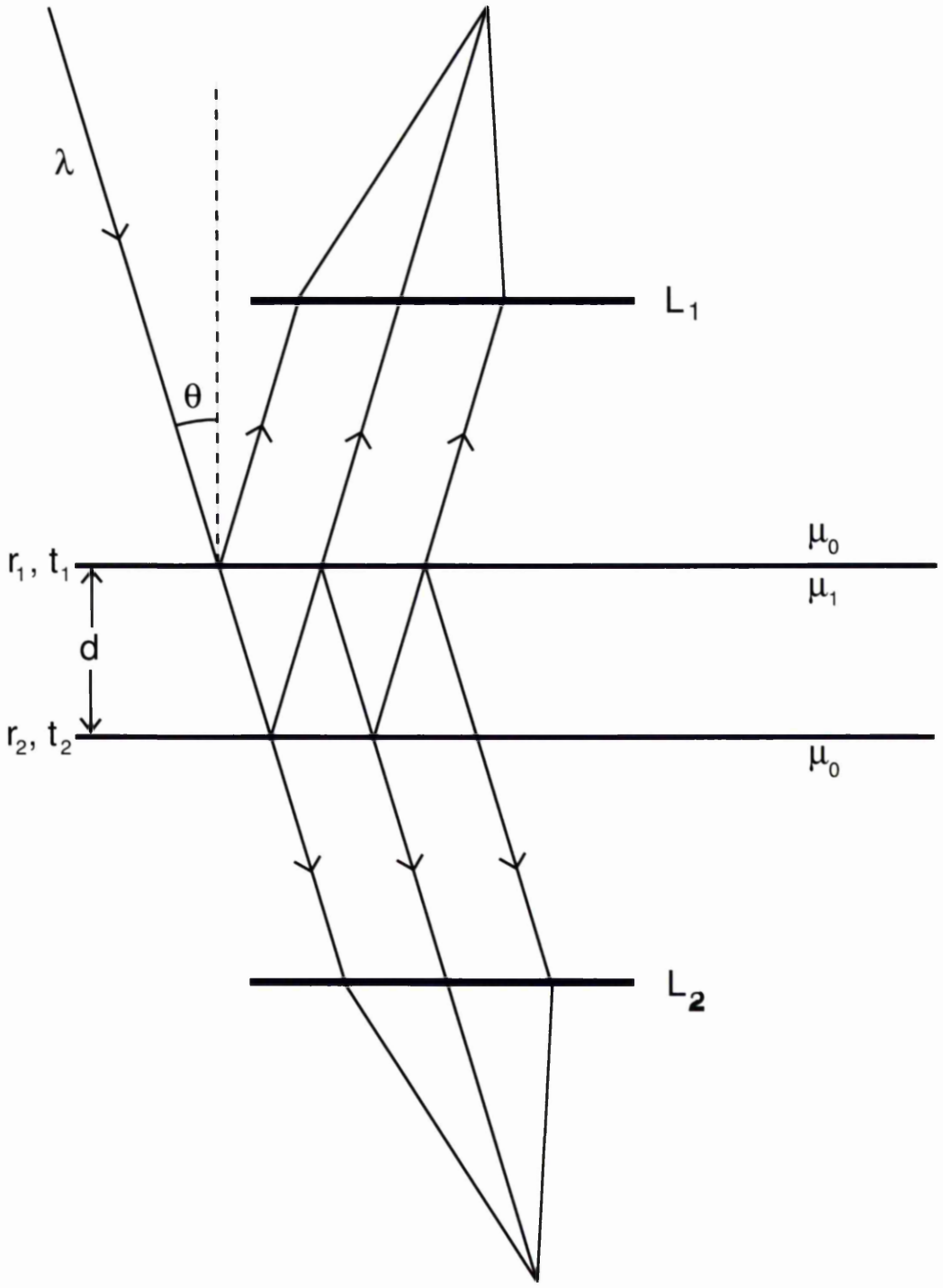

Figure B.1: Generation of multiple beams in a Fabry–Perot etalon (after Hernandez 1986).

which satisfy

$$\theta = \cos^{-1}\left(\frac{n\lambda}{2d\mu}\right). \tag{B.2}$$

If there are many plane waves, of wavelength λ, incident on the slab at different angles the slab (or Fabry–Perot etalon) will act as a filter in incident angle and, due to the circular symmetricity, a detector in the focal plane of L_2 will see a series of rings (see Fig. B.2).

Equation B.2 allows the most important properties of a Fabry–Perot etalon to be understood. The operating order of the etalon is defined for transmitted radiation perpendicular to the reflecting surfaces ($n_o = 2\mu\frac{d}{\lambda}$). For a fixed separation and refractive index there exists a minimum range of wavelengths that satisfy Eq. B.2 at all points in the field and this minimum range defines the free spectral range of the etalon. The free spectral range may be found from the difference in wavelength between the m^{th} and $m^{\text{th}} + 1$ order and for a given μd is

$$\left(\frac{1}{\lambda_2} - \frac{1}{\lambda_1}\right) = (2d\mu)^{-1} = \sigma/n_o, \tag{B.3}$$

which is normally given in wavenumber ($1/\lambda \equiv \Delta\sigma$). It is thus possible to limit the incident radiation to within the free spectral range of the etalon and take a series of images through the etalon within a range of values of μd which is sufficient to move the m^{th} order to the location of the $m^{\text{th}} + 1$. The result would be a set of data in which all the light within the free spectral range

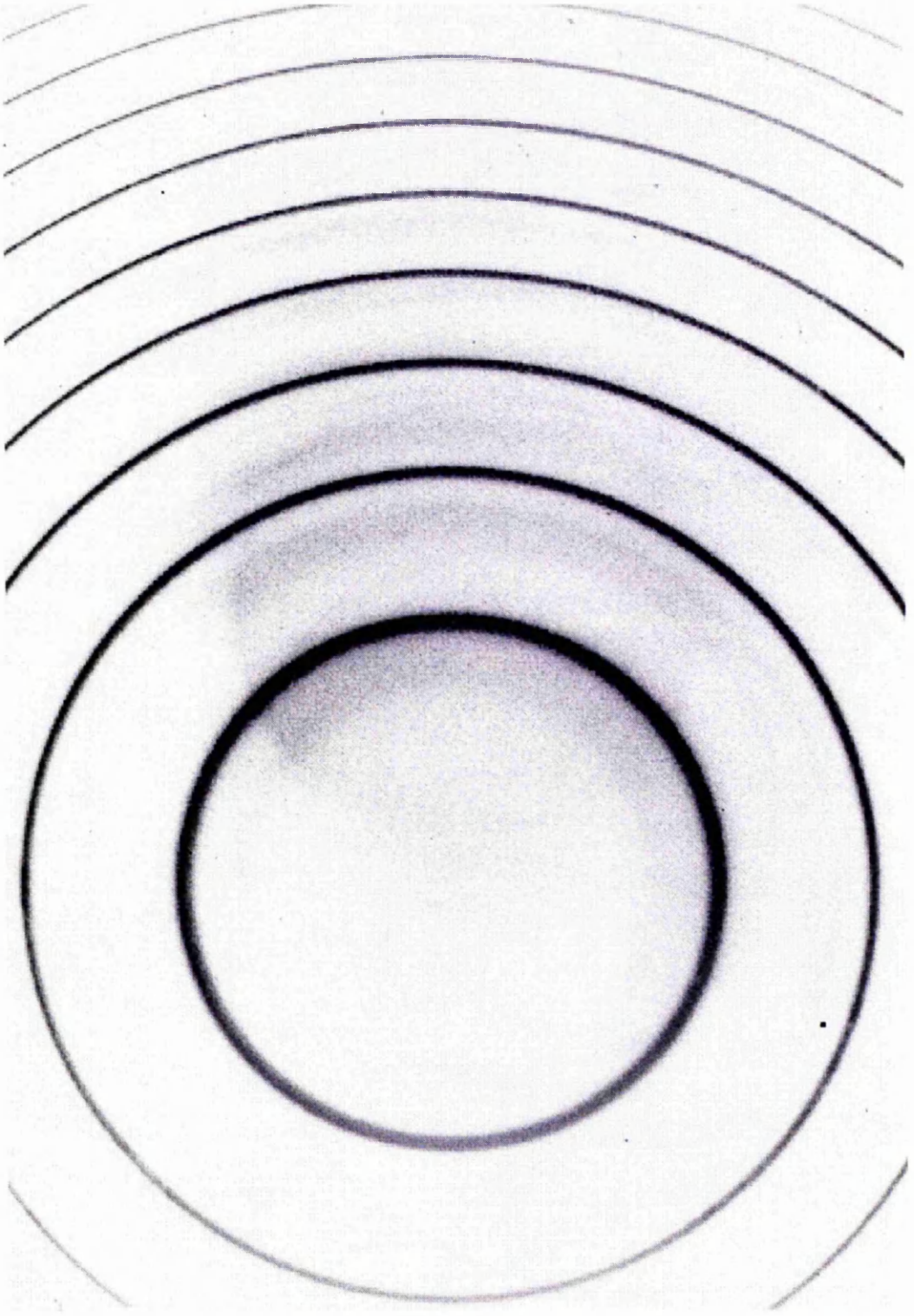

Figure B.2: A negative image in monochromatic radiation of an extended source viewed through a Fabry–Perot etalon obtained by the author with MOMI.

has been imaged and which, with some computational assistance, could be rearranged into images in the light of each sub–spectral range. This property is exploited in the scanning Fabry–Perot interferometers and μd may be varied by pressure scanning the refractive index or physically changing the separation d.

For a unit amplitude plane wave incident on the etalon the amplitudes of successive transmitted waves are:

$$t_1 t_2, t_1 t_2 r_2^2 e^{i\phi}, t_1 t_2 r_2^4 e^{2i\phi}, \ldots, \tag{B.4}$$

which when combined at the focus by L_2 give a total amplitude

$$A_t(\phi) = t_1 t_2 + t_1 t_2 r_2^2 e^{i\phi} + t_1 t_2 r_2^4 e^{2i\phi} + \ldots = \left(1 - Re^{i\phi}\right)^{-1} \tau, \tag{B.5}$$

where $t_1 t_2 = \tau$ and $r_2^2 = R$. The transmitted intensity is found from the product of the transmitted amplitude and its complex conjugate,

$$I_t(\phi) = A_t(\phi) A_t^*(\phi) \tag{B.6}$$

$$= \left[1 + R^2 - 2R\cos\phi\right]^{-1} \tau^2. \tag{B.7}$$

Since energy is conserved, $R + \tau + A = 1$, where A is a coefficient representing the absorbed and/or scattered light, Eq. B.7 may be rewritten

$$I_t(\phi) = \left(\frac{1-A}{1-R}\right)^2 (1-R)^2(1+R^2-2R\cos\phi)^{-1}. \tag{B.8}$$

The half–width at half–height (HWHH) is thus given by

$$\delta\phi = 2\sin^{-1}\left[\frac{1-R}{2R^{1/2}}\right], \tag{B.9}$$

and for small values of the inverse sine's argument can be approximated by

$$\delta\phi \approx \frac{1-R}{R^{1/2}}. \tag{B.10}$$

The reflective finesse, N_R, is twice the inverse of the ratio of the HWHM to the period, 2π, i.e. the number of full–widths at half–maximum in the free spectral range, and is, therefore, independent of scale and given by

$$N_R = \pi\left(2\sin^{-1}\left[\frac{1-R}{2R^{1/2}}\right]\right)^{-1}, \tag{B.11}$$

or, in the same approximation as Eq. B.10,

$$N_R \approx \frac{\pi R^{1/2}}{1-R}. \tag{B.12}$$

Equation B.10 shows that the reflective finesse depends only on the reflectivity, R, and Eq. B.8 shows that the light leakage that occurs at the minimum ($C = I_t(\phi)_{\max}/I_t(\phi)_{\min} = (1+R)^2/(1-R)^2$, where C is the contrast) also depends only on the reflectivity and therefore the reflective finesse.

Whilst the above treatment gives an insight into the essential properties of

the Fabry–Perot etalon it is based on an ideal etalon which is, in practice, unachievable. Microscopic defects, errors in parallelism, finite apertures and non–monochromatic sources all conspire to reduce the ideal performance. An effective finesse, which incorporates the forementioned defects may be used in place of the reflective finesse. A full treatment of the Fabry–Perot etalon, which is beyond the scope of this appendix, may be found in (Hernandez 1986).

Appendix C

Echelle gratings

In Fig. C.1, an Echelle reflection type diffraction grating is illustrated. Assuming that the optical axis is along the face normal (dashed line; Littrow configuration) and that a monochromatic plane wave, of wavelength λ, is incident on the grating at an angle ϕ to the optical axis then intensity maxima will occur, due to the constructive interference of reflections from each surface, at output angles which satisfy

$$m\lambda = a[\sin(\delta + \phi) + \sin(\delta + \phi_\lambda)], \tag{C.1}$$

where a is the groove width (there are 31.6 grooves mm^{-1} on the grating used in MES), δ is the Echelle blaze angle, ϕ_λ is the output angle and m is an integer.

The separation between maxima can be considered in wavelength space i.e.

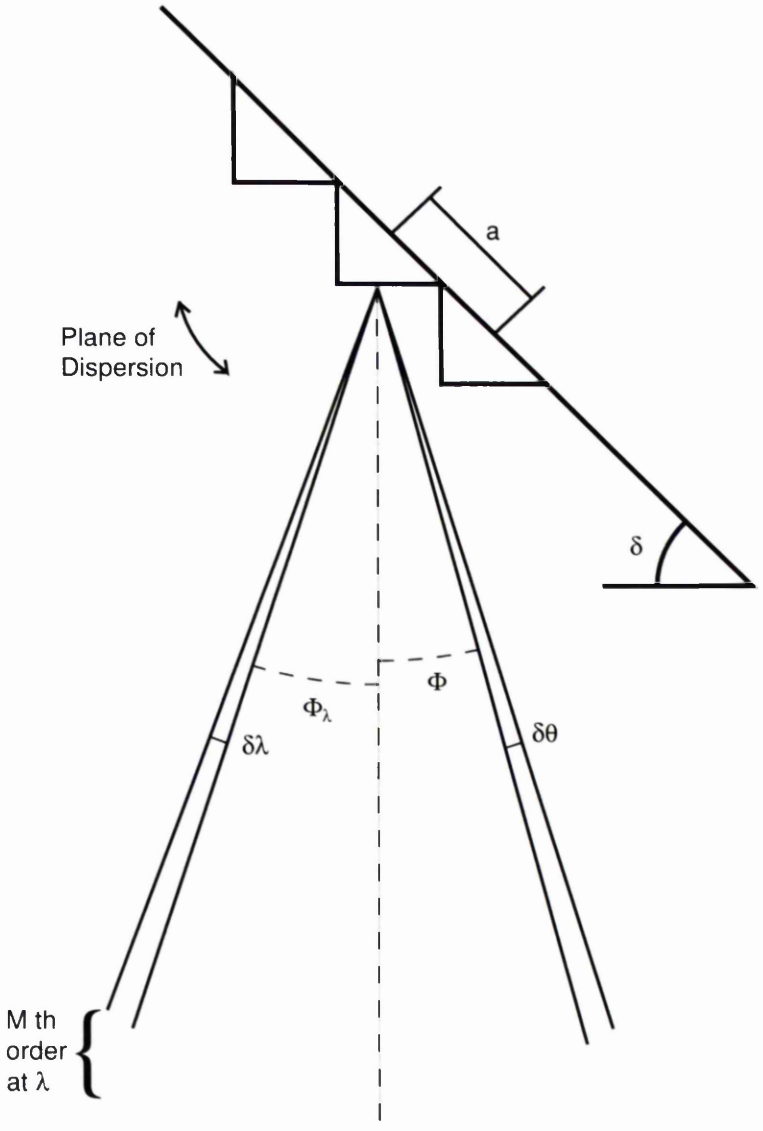

Figure C.1: Illustration of an Echelle diffraction grating

the difference in wavelength between $m\lambda$ and $(m+1)\lambda'$ and is simply

$$\Delta\lambda = \frac{\lambda}{m}, \tag{C.2}$$

To find the resolution of the spectrometer, again referring to Fig. C.1, with a slit width of $\delta\theta$ in angular dimensions at the grating one can take the derivative of Eq. C.1 and re–arrange to give

$$\frac{\lambda}{\delta\lambda} = \frac{\sin(\delta+\phi)+\sin(\delta+\phi_\lambda)}{\cos(\delta+\phi)\delta\theta}. \tag{C.3}$$

Echelle gratings have $\delta \sim 60°$ and therefore operate at high orders (the maximum intensity is placed at large n); consequently Echelle gratings have $\Delta\lambda$ small.

References

Amnuel P. R., Guseinov O. K., Novruzova K. I., Rustamov I. S., 1984, Ap&SS, 107, 19

Appenzeller I., 1989, in IAU Colloq. 113: Physics of Luminous Blue Variables. p. 195

Baars J. W. M., Wendker H. J., 1987, A&A, 181, 210

Bains I., Bryce M., 1997, Acta Cosmologica, 23, 107

Balick B., Rugers M., Terzian Y., Chengalur J. N., 1993, ApJ, 411, 778

Balick B., Perinotto M., Maccioni A., Terzian Y., Hajian A., 1994, ApJ, 424, 800

Balick B., Alexander J., Hajian A. R., Terzian Y., Perinotto M., Patriarchi P., 1998, AJ, 116, 360

Balick B., 1987, AJ, 94, 671

Barlow M. J., Drew J. E., Meaburn J., Massey R. M., 1994, MNRAS, 268, L29

Bjorkman J. E., Cassinelli J. P., 1993, ApJ, 409, 429

Bobrowsky M., Zijlstra A. A., Grebel E. K., Tinney C. G., Te Lintel Hekkert P., Van De Steene G. C., Likkel L., Bedding T. R., 1995, ApJL, 446, L89

Bode M. F., Evans A., 1989, Classical novae. Wiler & Sons, Chichester

Bohigas J., Olguin L., 1996, Revista Mexicana de Astronomia y Astrofisica, 32, 46

Boksenberg A., Burgess D. E., 1973, Proc. Symp. on Television Type Sensors, , 21

Borkowski K. J., Harrington J. P., Tsvetanov Z. I., 1995, ApJL, 449, L143

Bryce M., Lopez J. A., Holloway A. J., Meaburn J., 1997, ApJL, 487, L161

Burger P., Lamers H. J. G. L. M., 1989, A&A, 218, 161

Clayton C., 1987, PhD thesis, University of Manchester

Cliffe J. A., Frank A., Livio M., Jones T. W., 1995, ApJL, 447, L49

Cohen M., Kunkel W., Lasker B. M., Osmer P. S., Fitzgerald M. P., 1978, ApJ, 221, 151

Corradi R. L. M., Schwarz H. E., 1993, A&A, 268, 714

Corradi R. L. M. a. K., Schwarz H. E., 1995, A&A, 293, 871

Corradi R. L. M., Guerrero M., Manchado A., Mampaso A., 1997, New Astronomy, 2, 461

Courtes G., Louise R., Monnet G., 1968, Annales d'Astrophysique, 31, 493

Cudworth K. M., 1974, ApJ, 79, 1384

De Groot M., 1988, Irish Astronomical Journal, 18, 163

Dgani R., Soker N., 1998, ApJ, 495, 337

Dyson J. E., Meaburn J., 1971, A&A, 12, 219

Evans D. S., Thackeray A. D., 1950, MNRAS, 110, 429

Figer D. F., Najarro F., Morris M., MCLean I. S., Geballe T. R., Ghez A. M., Langer N., 1998, ApJ, 506, 384

Figer D. F., Morris M., Geballe T. R., Rich R. M., Serabyn E., McLean I. S., Puetter R. C., Yahil A., 1999, ApJ, 525, 759

Figer D. F., McLean I. S., Morris M., 1995, ApJL, 447, L29

Frank A., Mellema G., 1994, ApJ, 430, 800

Frank A., Ryu D., Davidson K., 1998, ApJ, 500, 291

Frank A., 1999, New Astronomy Review, 43, 31

Fréedericks V., 1911, Ann. Phys. (Leipzig), 34, 784

García-Segura G., Langer N., Rózyczka M. l., Franco J., 1999, ApJ, 517, 767

Garcia-Segura G., Mac Low M. M., Langer N., 1996, A&A, 305, 229

Georgelin Y. P., 1970, A&A, 9, 441

Goodman J. W., 1968, Introduction to Fourier optics. McGraw-Hill

Guyon O. et al., 1999, PASP, 111, 1321

Hartquist T. W., Dyson J. E., 1993, QJRAS, 34, 57

Hernandez G., 1986, Fabry–Perot Interferometers. Cambridge University Press

Hillier D. J., Crowther P. A., Najarro F., Fullerton A. W., 1998, A&A, 340, 483

Humphreys R. M., Davidson K., 1979, ApJ, 232(409)

Humphreys R. M., Davidson K., 1994, PASP, 106, 1025

Humphreys R. M., Davidson K., Smith N., 1999, PASP, 111, 1124

Jacquinot P., Roizen-Dossier B., 1963, Progress in Optics, 1, 29

Jacquinot P., 1954, J. Opt. Soc. Amer, 44, 761

Kahn F. D., West K. A., 1985, MNRAS, 212, 837

Lamers H. J. G. L. M., De Groot M., Cassatella A., 1983, A&A, 123, L8

Lamers H. J. G. L. M., De Groot M., Cassatella A., 1983, A&A, 128, 299

Lamers H. J. G. L. M. et al., 1996, A&A, 315, L229

Lamers H. J. G. L. M., Korevaar P., Cassatella A., 1985, A&A, 149, 29

Lamers H. J. G. L. M., 1987, in Instabilities in Luminous Early Type Stars. p. 99

Lamers H. J. G. L. M., 1989, in IAU Colloq. 113: Physics of Luminous Blue Variables. p. 135

Lang C. C., Figer D. F., Goss W. M., Morris M., 1999, AJ, 118, 2327

Langer N., 1989, in IAU Colloq. 113: Physics of Luminous Blue Variables. p. 221

Laques P., Vidal J. L., 1979, A&A, 73, 97

Lépine S., Shara M. M., Livio M., Zurek D., 1999, ApJL, 522, L121

Lesser M. P., 1990, in CCDs in astronomy; Proceedings of the Conference, Tucson, AZ, Sept. 6-8, 1989 (A91-45976 19-33). San Francisco, CA, Astronomical Society of the Pacific, 1990, p. 65-75; Discussion, p. 75. Research supported by University of Arizona. p. 65

Lopez J. A., Meaburn J., 1983, MNRAS, 204, 203

Lopez J. A., Meaburn J., Bryce M., Rodriguez L. F., 1997, ApJ, 475, 705

Lopez J. A., Meaburn J., Bryce M., Holloway A. J., 1998, ApJ, 493, 803

Lopez J. A., Meaburn J., Palmer J. W., 1993, ApJL, 415, L135

Lopez J. A., Roth M., Tapia M., 1993, A&A, 267, 194

Lopez J. A., Vazquez R., Rodriguez L. F., 1995, ApJL, 455, L63

Lucy L. B., 1995, A&A, 294, 555

Lyot B., 1939, MNRAS, 99, 580

Malbet F., 1996, A&AS, 115, 161

Mastrodemos N., Morris M., 1999, ApJ, 523, 357

Meaburn J., Walsh J. R., 1980, MNRAS, 193, 631

Meaburn J., Walsh J. R., 1985, MNRAS, 215, 761

Meaburn J., Walsh J. R., 1989, A&A, 223, 277

Meaburn J., White N. J., 1982, Ap&SS, 82, 423

Meaburn J., Blundell B., Carling R., Gregory D. F., Keir D., Wynne C. G., 1984, MNRAS, 210, 463

Meaburn J., Lopez J. A., Barlow M. J., Drew J. E., 1996, MNRAS, 283, L69

Meaburn J., Lopez J. A., Bryce M., Mellema G., 1996, A&A, 307, 579

Meaburn J., Clayton C. A., Bryce M., Walsh J. R., Holloway A. J., Steffen W., 1998, MNRAS, 294, 201

Meaburn J., Lopez J. A., Bryce M., Redman M. P., 1998, A&A, 334, 670

Meaburn J., O'Connor J. A., Lopez J. A., Bryce M., 2000, MNRAS, in preperation

Meaburn J., López J. A., O'Connor J., 1999, ApJL, 516, L29

Meaburn J., 1959, PhD thesis, University of Manchester

Meaburn J., 1970, Nature, 228, 44

Meaburn J. The detection and spectrometry of faint light, chapter 6, p. 119, D. Reidel, 1976

Mellema G., 1995, MNRAS, 277, 173

Mellema G., 1996, Jets from stars and galactic nuclei, Springer Lecture Notes. Springer

Mellema G., 1997, A&A, 321, L29

Mendez R. H., Herrero A., Manchado A., 1990, A&A, 229, 152

Moffat A. F. J., Drissen L., Robert C., 1989, in IAU Colloq. 113: Physics of Luminous Blue Variables. p. 229

Morris M., Reipurth B., 1990, PASP, 102, 446

Morse J. A., Davidson K., Bally J., Ebbets D., Balick B., Frank A., 1998, AJ, 116, 2443

Noll R. J., 1985, Proc. SPIE, 513, 499

Norman C. A., Ikeuchi S., 1989, ApJ, 345, 372

Luminous Blue Variables: Massive Stars in Transition, 1997

Nota A., Livio M., Clampin M., Schulte-Ladbeck R., 1995, ApJ, 448, 788

O'Connor J. A., Meaburn J., López J. A., Redman M. P., 1999, A&A, 346, 237

O'Connor J. A., Redman M. P., Holloway A. J., Bryce M., Lopez J., Meaburn J., 2000, ApJ, 531, 336

O'Connor J. A., Meaburn J., Bryce M., 1998, MNRAS, 300, 411

Palmer J. W., Lopez J. A., Meaburn J., Lloyd H. M., 1996, A&A, 307, 225

Pascoli G., 1992, PASP, 104, 350

Phillips J. P., Mampaso A., 1988, A&A, 190, 237

Quinn D. E., Moore T. J. T., Smith R. G., Smith C. H., Fujiyoshi T., 1996, MNRAS, 283, 1379

Redman M. P., Dyson J. E., 1999, MNRAS, 302, L17

Redman M. P., O'Connor J., Holloway A., Bryce M., Meaburn J., 2000, MNRAS, 312(2), L23

Sahai R. et al., 1999, AJ, 118, 468

Scarrott S. M., Scarrott R. M. J., Wolstencroft R. D., 1994, Ap&SS, 216, 31

Schwarz H. E., Corradi R. L. M., Melnick J., 1992, A&AS, 96, 23

Schwarz H. E., Aspin C., Corradi R. L. M., Reipurth B., 1997, A&A, 319, 267

Shore S. N., Altner B., Waxin I., 1996, AJ, 112, 2744

Skinner C. J., Exter K. M., Barlow M. J., Davis R. J., Bode M. F., 1997, MNRAS, 288, L7

Skinner C. J., Becker R. H., White R. L., Exter K. M., Barlow M. J., Davis R. J., 1998, MNRAS, 296, 669

Slavin A. J., O'Brien T. J., Dunlop J. S., 1995, MNRAS, 276, 353

Smith L. J., Nota A., Pasquali A., Leitherer C., Clampin M., Crowther P. A., 1998, ApJ, 503, 278

Soker N., 1998, MNRAS, 299, 562

Soker N., 1998, ApJ, 496, 833

Steffen W., López J. A., 1998, ApJ, 508, 696

Tyson J. A., Seitzer P., 1988, ApJ, 335, 552

Vakili F., Mourard D., Bonneau D., Morand F., Stee P., 1997, A&A, 323, 183

van Der Veen W. E. C. J., Habing H. J., Geballe T. R., 1989, A&A, 226, 108

Van Genderen A. M., Steemers W. J. G., Feldbrugge P. T. M., Groot M., Damen E., Van Den Boogaart A. K., 1985, A&A, 153, 163

Van Genderen A. M. et al., 1990, A&AS, 82, 189

Van Genderen A. M., Sterken C., De Groot M., Burki G., 1999, A&A, 343, 847

Wang Y., Vaughan A. H., 1988, Applied Optics, 27, 27

Webbink R. F., Livio M., Truran J. W., Orio M., 1987, ApJ, 314, 653

Weigelt G., Balega Y., Preibisch T., Schertl D., Schöller M., Zinnecker H., 1999, A&A, 347, L15

Whitehead M. J., 1989, PhD thesis, University of Manchester

Zucker D. B., Soker N., 1993, ApJ, 408, 579